University of Nottingham
UK | CHINA | MALAYSIA

Toward the large-scale continuous synthesis of flaky barium sulfate

by

Yingrong Xu

Submitted in partial satisfaction of the requirements for the degree of

Master of Mechanical Engineering

Under the supervision of

Dr. Guang Li

Prof. Xiaogang Yang

July 2024

DEDICATION

To my family.

ACKNOWLEDGEMENTS

At the beginning of this thesis, I would like to extend my sincere gratitude to those who provided me with friendly help, especially my supervisor, Dr Guang Li. Completing my research with his professional guidance and valuable suggestions is possible. Due to my lack of relevant chemical knowledge, I could not develop significant experiment schemes when designing experiments. With rich personal experience and excellent research skills, Dr. Guang Li gives me many helpful instructions. As a result, all these experiments can be conducted efficiently and successfully during the whole research period. After getting the data, his timely feedback and unique opinions about experiment outcomes have inspired me to optimize the following experiments. I would also like to thank him for pointing out some mistakes in my scientific research process, which helped me develop the proper scientific thought on fluid dynamics and chemicals. Finally, I am very grateful to him for allowing me to study at UNNC.

I also want to thank my peer mentor, Dr. Bin Li, who instructed me on my topic and taught me many professional skills, which laid the groundwork for my research. Without his help, I could hardly finish the master's work quickly.

Most importantly, I must express my gratitude to my parents, Mrs. Yueqing Wang and Mr. Xiujun Xu, for their unconditional support. Finally, I want to thank my partner, Denghui, for her understanding and company.

SYNOPSIS

The conventional barium sulfate used in foundation cosmetics encountered some problems, such as poor extendibility over the skin, insufficient adhesion to the skin, and another uncomfortable feeling after using it. To overcome these disadvantages, flaky barium sulfate was proposed, which had a plate-like structure and an aspect ratio of 5-100, and the ratio of the square of the circumference of the plate and the area of the orthogonal projection plane is about 20:1-150:1 (European Patent Application No. 0445785A1, Japanese Patent Laid-open No. 41718/1983). Flaky barium sulfate has a specific crystal structure with a relatively high area ratio compared to the other morphology of barium sulfate, and barium sulfate with a flake shape also has unique optical characteristics like shading properties and a smoother feeling. Therefore, flaky barium sulfate can be used in foundation cosmetics to give an excellent skin feel instead of conventional barium sulfate products. However, producing such barium sulfate involves several complicated processes due to the requirement of post-treatment of the crude products, such as heat treatment or washing with mineral acid. However, removing the crude products after such a post-treatment is complex, and developing the desired shape is insufficient. Given this situation, this thesis aims to explore one efficient approach to low energy consumption in the mass production of flaky barium sulfate that satisfies the abovementioned requirements. This thesis involves the synthesis of flaky barium sulfate and using numerical simulation to analyze the influence of fluid dynamics in the chemical reactor on the synthesis process and properties of Barium sulfate:

1. Four different types of reactors, including high-speed shear mixer, simple stirred tank reactor, Taylor-Couette reactor, and ultrasonic reactor, were applied to the small-scale synthesis of barium sulfate. The experiments were carried out in different reactors to obtain the target product by adjusting the operation process parameters, such as reactant concentration, reaction temperature, reactor parameters (rpm, volt), feed flow rate, and others.
2. The morphology and particle size of the products were characterized using a field emission scanning electron microscope and a particle size analyzer. After comparing the products prepared using different reactors, the results show that the Taylor-Couette reactor has an obvious advantage in the synthesis of flaky barium sulfate. Therefore, the Taylor-Couette reactor was determined for the large-scale production of flaky barium sulfate. The last two large-scale experiments also showed the reproducibility of the mass production.
3. With the help of ANSYS Fluent, the hydrodynamics generated in Taylor-Couette reactors were captured. The visual descriptions of the fluid mechanisms give insights into the influence of hydrodynamics on the properties of barium sulfate.

Overall, this masterwork provides a feasibility study of the application of the Taylor-Couette reactor to synthesize flaky barium sulfate, providing an essential platform for further industrial application. Future research on the characteristics and application of Taylor-Couette reactors in the industry will be expanded further.

TABLE OF CONTENTS

NOMENCLATURES

Abbreviations

a	ion activities, mol/m^3
C_1, C_2	model constants
C	concentration of the reactant solution, mol/m^3
C_s	saturated concentration, mol/m^3
$C_{\varepsilon 1}$	model constant for ε equation
$C_{\varepsilon 2}$	model constant for ε equation
C_μ	model constant for the calculation of η_K
d	gap width between the inner cylinder and the outer cylinder, m
d_{jet}	diameter of the inlet pipe, m
d_{32}	Sauter mean diameter, m
D	diameter of the impeller, m
E_V	energy density, J/m^3
G	dimensionless torque
H	length of the cylinder, m
K_{sp}	solubility product, mol^2/L^2
l	length scale, m
m_{net}	mass flow rate, kg/s
p	constant pressure, Pa
P	total power input, W
Q	volumetric flowrate, m^3/s
r_i	radius of the inner cylinder, m
R	ideal gas constant, J/mol/K
Re	Reynolds number, dimensionless
Re_{ax}	axial Reynolds number, dimensionless
Re_c	critical Reynolds number, dimensionless

Re_{jet}	jet Reynolds number, dimensionless
R_i	radius of the inner cylinder, m
R_o	radius of the outer cylinder, m
S_a	supersaturation of the solution, mol^2/m^6
t_M	micro mixing time, s
Ta	Taylor number, dimensionless
Ta^+	modified Taylor number, dimensionless
T	temperature, K
u'	fluctuating velocity, m/s
u_i	instantaneous velocity, m/s
u_{jet}	average velocity in the inlet pipe, m/s
V	reactor volume, m^3
Vi, We	Webber number, dimensionless
x_j	coordinate, m

Greek letters

μ_2	chemical potential, J/mol
μ_s	chemical potential of the saturated solution, J/mol
μ_C	chemical potential of the solid phase, J/mol
ω	angular velocity, rad/s
ν	kinematic viscosity, m^2/s
ρ	density of the fluid, kg/m^3
μ	dynamic viscosity, Pa s
γ_i	average activity coefficient for ions in solution
η	ratio of inner cylinder to outer cylinder
η_K	Kolmogoroff length scale, m
φ_{max}	maximum stream function, kg/s
ε	energy dissipation rate or power per unit mass, m^2/s^3 or W/kg

σ_k	turbulent Prandtl number for *k* equation
σ_ε	turbulent Prandtl number for ε equation
τ	torque, N m
γ	shear strain rate, 1/s

Chapter 1. Current status of the synthesis of barium sulfate

1.1 Introduction

The synthesis of barium sulfate has been thoroughly researched and developed in recent decades. A large amount of research has been conducted on some key factors and their influencing mechanisms, such as supersaturation, pH valve, temperature, additives, synthesis system, etc. Kucher et al. (2006) investigated the influence of the supersaturation of reactants in the reaction system on the morphology of barium sulfate and particle size distribution. The results revealed that a low supersaturation of barium or sulfate ions leads to a smaller average particle size. According to the report of Wang et al. (2021), extremely high temperature (200°C) has a noticeable effect on the morphology of barium sulfate. Compared to the product synthesized at room temperature, the product obtained at 200°C has various morphologies, such as plate-shaped, X-shaped, granular, and other forms. Using filtration dispersion technology, Chen et al. (2005) developed a novel method to prepare nanosized barium sulfate in the Oil/Water system. Nagaraja et al. (2007) synthesized spherical and cubic mesoporous barium sulfate particles using ethylene glycol (n-$HOCH_2CH_2OH$) as the solvent and $Ba(OH)_2$ solution and H_2SO_4 solution as the reactants. Much effort has been put into synthesizing barium sulfate of different morphologies using different additives. Yokota et al. (2000) prepared a round-shaped barium sulfate by adding Polyelectrolytes (PAA). Uchida et al. (2001) studied barium sulfate's morphology through hydrothermal synthesis, where rhombohedral, rod-like, and spindle-shaped were observed in the reaction systems with different additives like Egtazic acid (EGTA), Nitrilotriacetic acid (NTA), and Ethylenediaminetetraacetic acid (EDTA). Until now,

PAA and EDTA have been the most often used additives in research on the controllable synthesis of BaSO4 crystals. The influence of oxalate ions appears in barium sulfate synthesis to be due to surface interactions, which is similar to the function mechanism of EDTA (Jones et al., 2018). Researchers have also tried to build a connection between barium sulfate precipitation and applied reactors. A new spinning disk reactor was used to investigate the reaction-precipitation process of barium sulfate (Cafiero et al., 2002). Wong et al. (2003) studied the effect of reactants' molar ratio and feed mode on barium sulfate precipitation in a conventional stirred tank reactor. Aljishi et al. (2013) examined the influence of vortex flow on barium sulfate precipitation in Taylor-Couette reactors. In practice, a novel high-speed spinning disk reactor was used to prepare nanosized barium sulfate (Jahanshahi-Anboohi and Molaei Dehkordi, 2019).

1.2 Research background and main aim

Flaky barium sulfate, which had a plate-like structure and an aspect ratio of 5-100, and the ratio of the square of the circumference of the plate and the area of the orthogonal projection plane is about 20:1-150:1 (European Patent Application No. 0445785A1, Japanese Patent Laid-open No. 41718/1983). Given the unique advantages of flaky barium sulfate in optical characteristics, the conventional barium sulfate used in cosmetics will definitely be replaced by flaky barium sulfate. Therefore, developing an economic way of large-scale synthesis (preliminary yield set $\geqslant$10 t/year) of flaky barium sulfate is quite meaningful. However, the above-mentioned approaches to preparing barium sulfate have some shortcomings in application to large-scale production, such as low efficiency (low throughput), high energy consumption (heating

requirement), and relatively high production cost (extra additives, pH regulation). In addition, there are only a few reports about preparing flaky barium sulfate in such references. Therefore, in this master research work, experimental investigations were conducted to find an optimal way to produce flaky barium sulfate with lower cost but higher efficiency. According to the main aim, the objectives are listed below:

1. Determining the type of chemical reactor suitable for producing flaky barium sulfate and the corresponding production process. Thus, four typical reactors (High-speed shear mixer, Sitrred tank reactor, Ultrasonic reactor, Taylor-Couette reactor) were selected for the synthesis of flaky barium sulfate.
2. Exploring the optimal process for synthesizing flaky barium sulfate in the Taylor-Couette reactor. The main operating parameters such as the concentration of the reactants, rotation speed of the reactor, feed flow rate, et al. were studied to find out the key factors influencing the quality of the flaky barium sulfate.
3. Conducting a set of large-scale continuous experiments to evaluate the feasibility and reliability of the Taylor-Couette reactor in future industrial applications.

1.3 Fundamentals of barium sulfate.

1.3.1 Properties of barium sulfate

Barium sulfate ($BaSO_4$) is a white crystalline solid with excellent stable chemistry. It is almost insoluble in conventional solvents, such as water, ethanol, and acids, due to its structural formula (Figure 1-1) but soluble in hot sulfuric acid. Barium sulfate is a commonly used laboratory and industrial chemical.

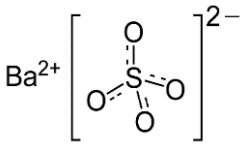

Figure 1-1 structural formula of barium sulfate.

Barium sulfate synthesized in different reaction conditions possesses different morphologies. The following pictures show some typical morphologies of barium sulfate. As shown in Figure 1-2, barium sulfate presents various shapes at different molar ratios of reactants, like a rose leaf, spherical particles, plate-like with extra growing crystals, star shape, rectangular and aggregated rice shape.

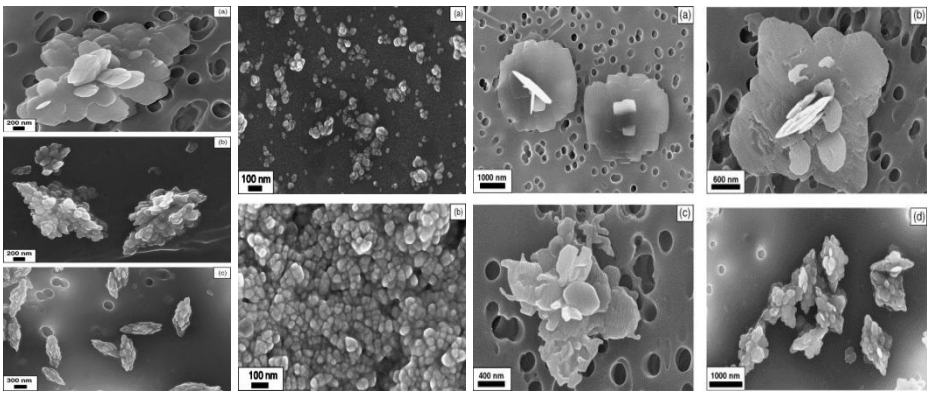

Figure 1-2 Different morphologies of barium sulfate synthesized at different molar ratio (Kucher et al., 2006).

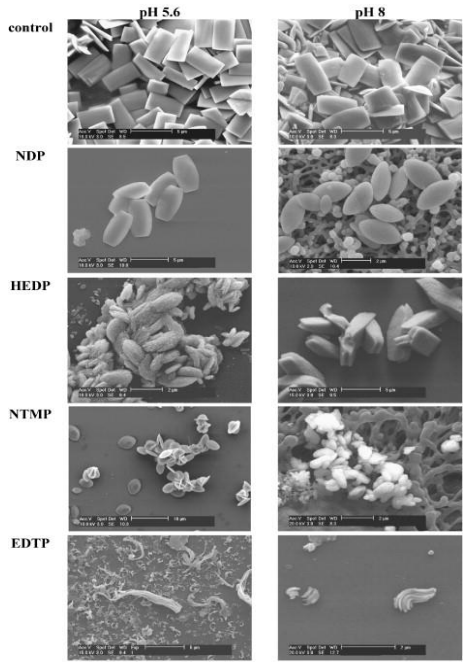

Figure 1-3 Different morphologies of barium sulfate synthesized by using different additives (Jones et al., 2003).

Barium sulfate prepared in reaction conditions using additives exhibits some exciting shapes. Compared with the morphologies of products prepared in a pure reactant system (only reactant materials exist), the morphologies of products obtained from reaction systems with additives are more regular and neater, and the surface of these products looks smooth. Rectangular, rice-like floc can be seen from Figure 1-3.

1.3.2 Synthesis of barium sulfate

Standard synthesis method of barium sulfate

Precipitation is an often-used synthesis method to prepare barium sulfate, and it has been employed in the past decades. Precipitation (or reaction crystallization) is an essential approach to producing chemical products in the industry. Many chemical materials such as

pharmaceuticals, biochemicals, catalysts, and pigments are produced with precipitation. In the standard precipitation processes, sparingly soluble forms during the chemical reaction, then start to precipitate as a solid by nucleation and growth (Kind, 2002). The size of these newly formed primary crystals is often on a nanometer scale. The phase transformation processes promote the rise and growth of nanoparticles. The appearance of new phases is generally attributed to the desire of the reaction system to transfer into a more stable state.

In a typical process of barium sulfate precipitation, the solution's supersaturation is the thermodynamic driving force, which motivates the solid particles to form nuclei and grow (Vicum et al., 2003). The formation of barium sulfate crystals is described in Eq. 1-1:

$$Ba^{2+} + SO_4^{2-} \rightarrow BaSO_4 \tag{1-1}$$

The chemical potentials of the liquid phase are equal to that of the solid phase in the reaction system. When the system is supersaturated, Eq. 1-2 can be employed to describe this deviation from the equilibrium (Bromley, 1973):

$$\Delta\mu = \mu_2 - \mu_2^e > 0 \tag{1-2}$$

Where μ is the chemical potential of barium sulfate, superscript “e” is the equilibrium state. This equation is established under constant pressure (P) and temperature (T) conditions.

The deviation ($\Delta\mu$) is defined by the concentration of the reactant solution (C) and the saturated concentration (C_s), shown in the below Eq. 1-3, where R is the ideal gas constant.

$$\Delta\mu = RT \ln \frac{C}{C_s} \tag{1-3}$$

Ion activities (a) can be used instead of concentrations (C) to describe the valid concentration of the reactants in a reaction system. The supersaturation of the solution (S_a) is defined as Eq. 1-4:

$$S_a = \sqrt{\frac{a_{Ba^{2+}} a_{SO_4^{2-}}}{K_{sp}}} = \gamma_i \pm \sqrt{\frac{C_{Ba^{2+}} C_{SO_4^{2-}}}{K_{sp}}} \tag{1-4}$$

Where $a_{Ba^{2+}}$ and $a_{SO_4^{2-}}$ represent the activities of barium ions and sulfuric ions, $C_{Ba^{2+}}$ and $C_{SO_4^{2-}}$ are the concentration of the barium ions and sulfuric ions, γ_i is the average activity coefficient, and the value of the solubility product $K_{sp} = 9.82 \times 10^{-11}$ mol^2/L^2 at 298.15 K is taken from Monnin (1999).

Particle formation involves two stages: nucleation and growth of the nuclei. The classical theory of nucleation points out that the difference between the actual concentration of the solution (C) and its saturated concentration (C_s) cause the supersaturation of a reaction system (ΔC):

$$\Delta C = C - C_s \tag{1-5}$$

A solid-liquid interface, also called interfacial forces, and excess free energy are required for nucleation. The chemical potential of crystals in the solution (μ_C) could be determined as Eq. 1-6 (Ketegenov et al., 2022), Where μ_C^0 is the standard chemical potential of the substance.

$$\mu_C = \mu_C^0 + RT \ln C \tag{1-6}$$

The chemical potential of the solid phase (μ_C) is thought to be equal to the concentration of the saturated solution (μ_s) in a typical saturated reaction system, defined by Eq. 1-7(Bromley, 1973):

$$\mu_s = \mu_C = \mu_C^0 + RT \ln C \tag{1-7}$$

The growth of nuclei results from the sequential attachment of sparingly soluble from the solution to the crystal surface. If the nucleus size is over-critical, such a reaction is favorable in

thermodynamics and irreversible. The nucleation step typically determines the final morphology and the size of particles. Therefore, in a typical reaction system of precipitation, supersaturation significantly influences the particle size distribution and the morphology of crystals. The ideal approach to obtaining nanosized particles is micromixing at the reactants' molecular level has been achieved before the system establishes a steady-state nucleation rate. Generally, crystal growth often involves several steps, such as diffusion of solute from the solution bulk to the crystal surface, adsorption on crystal surfaces, diffusion over the surfaces, attachment to steps of the surfaces, diffusion along a step, and integration into a crystal kink site (Marchisio et al., 2002). Through the fast sampling technique and the cryo-TEM analysis, Judat and Kind (2004) pointed out that the growth of the early formed particles since the beginning of nucleation in a short time is composed of many nanoparticles, which aggregate in a highly ordered manner. The diffraction pattern of barium sulfate particles showed that many small-angle grain boundaries appeared initially. However, monocrystalline was observed at the end of precipitation, concluding that the growth of $BaSO_4$ crystals follows a combined mechanism of a self-assembled aggregation and a fast recrystallization process. The action of aggregation, the hydrodynamic behavior of the suspensions, and the shear strain rates present in the reactors participated in forming the final morphology of the products.

Typical reaction systems used to synthesize barium sulfate

Barium chloride ($BaCl_2$) and sodium sulfate (Na_2SO_4) are the often-used materials to prepare $BaSO_4$. Such a chemical reaction can be described as Eq. 1-8. Chen et al. (2005) used sodium

sulfate and barium chloride to synthesize barium sulfate with a rice shape in an O/W (oil/water) system, as shown in Figure 1-4.

$$BaCl_2 + Na_2SO_4 \rightarrow BaSO_4 \downarrow +2NaCl \quad (1\text{-}8)$$

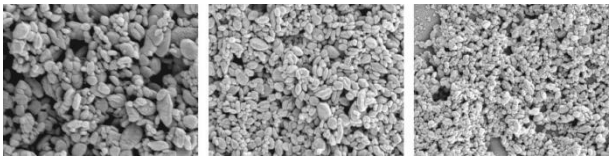

Figure 1-4 Barium sulfate synthesized in O/W system (Chen et al., 2005).

Sometimes, sulfuric acid (H_2SO_4) can be used as the reactant instead of Na_2SO_4. Yokota et al. (2000) used H_2SO_4 and $BaCl_2$ to successfully prepare round-shaped barium sulfate by adding polyelectrolytes at different pH values. Figure 1-5 shows barium sulfate products with different shapes.

$$BaCl_2 + H_2SO_4 \rightarrow BaSO_4 \downarrow +2HCl \quad (1\text{-}9)$$

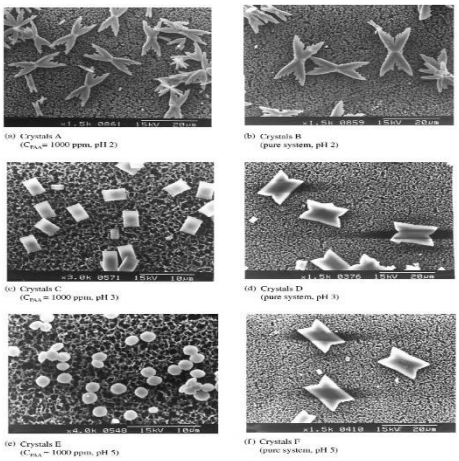

Figure 1-5 Barium sulfate synthesized by using H_2SO_4 and $BaCl_2$ (Yokota et al., 2000).

Nagaraja et al. (2007) utilized $Ba(OH)_2 \cdot 8H_2O$ and H_2SO_4 to synthesize barium sulfate. Spherical and small irregular plate-like barium sulfate were observed in that reaction system, as shown in Figure 1-6.

$$Ba(OH)_2 \cdot 8H_2O + H_2SO_4 \rightarrow BaSO_4 \downarrow + 10H_2O \quad (1\text{-}10)$$

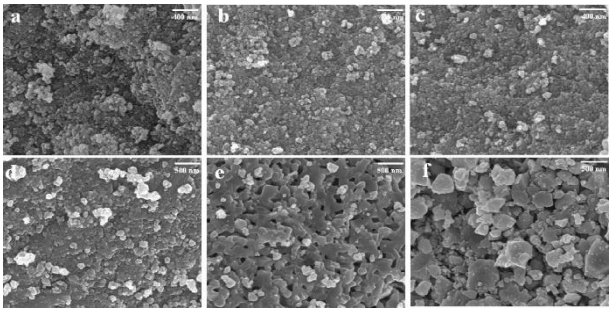

Figure 1-6 Barium sulfate synthesized by $Ba(OH)_2 \cdot 8H_2O$ and H_2SO_4 with ethylene glycol (Nagaraja et al., 2007).

As mentioned in those typical reaction conditions, barium sulfate precipitation is a reaction process in which barium ions combine with sulfuric ions to form the precipitated barium sulfate. Different reactants used to prepare barium sulfate could form different morphological barium sulfates, such as plate-like, spherical, rectangular etc.

1.3.3 Application of barium sulfate

As an important industrial raw material, barium sulfate is widely used in plastics, rubber, paint, and pharmaceutical formulations (Qi et al., 1996, Sireci, 2021). Due to its high refractive index (1.63~1.65), barium sulfate appears whiter in color. It has a specific coverage, which can be used in coating or paints to replace some of the more expensive raw materials and can control the viscosity, gloss, and stability of the finished paint. In medicine, barium sulfate is often used in radiological examinations as a gastrointestinal contrast agent because it can absorb X-rays in the gastrointestinal tract, and its characteristics are unharmful to humans (Kilian et al., 2023). Besides, barium sulfate brick can be used to build an X-ray room (Kiatwattanacharoen et al., 2020). Because of its high reflectance throughout the solar waveband, barium sulfate can

produce a building composite with excellent reflective cooling performance (Han et al., 2024). Some Polyvinyl chloride (PVC) composite materials can be significantly improved when the hydrophobic $BaSO_4$ is added (Hu et al., 2014). Flaky barium sulfate is also often applied in color cosmetics, effectively hiding spots or freckles on the skin (Johnson Jr et al., 2018). Seung-Yong and Hak-Hee (2004) used barium sulfate and polydimethylsiloxane to successfully synthesize a composite powder foundation, which has a better Ultraviolet (UV) shielding ability, hiding, and blooming effect.

1.4 Effect of additives used in the preparation of barium sulfate

In many synthesis processes, it is significant to maintain the stabilization of the concentrated aqueous suspensions to obtain the desired nanoparticles. Thus, polymeric dispersants are often used to stabilize the reaction system. The mechanism of polymer stabilization is that polymers can form an adsorption layer around the solid particles, which diminishes the possibility of configurations between two approaching particles. Besides, the aggregation of the particles is inhibited by the osmotic pressure, which is generated from the high concentration of adsorbed polymer between these two particles. Polymers, which can reduce the Gibbs' free energy of a reaction system when they are dissolved, are typically considered suitable stabilizers. When approaching soluble covered with polymer, the Gibbs' free energy rises, and the soluble repels. Several kinds of additives are introduced in the synthesis of barium sulfate.

1.4.1 Polyacrylic acid (PAA)

Li et al. (2016) used PAA as a modifier to manipulate the growth of barium sulfate crystals. Their research showed that PAA is a contributing inhibitor that can be applied to manipulate barium sulfate morphology. As shown in Figure 1-7, the morphology of $BaSO_4$ was effectively controlled by the PAA. The mean particle size of barium sulfate decreased from 10 μm to 3 μm as the PAA concentration increased. Meanwhile, irregular, blunt, rose-shaped structures with rigid surfaces gradually grew into exclusively spherical structures. This result may be due to the weak interactions between the PAA-COOH groups and the BaSO4 particle planes. When the concentration of PAA increased, the interactions between the PAA-COOH groups and the

$BaSO_4$ crystal planes were strengthened; thus, the barium sulfate crystals were spherical. Akyol and Cedimagar (2016) also reported a similar phenomenon.

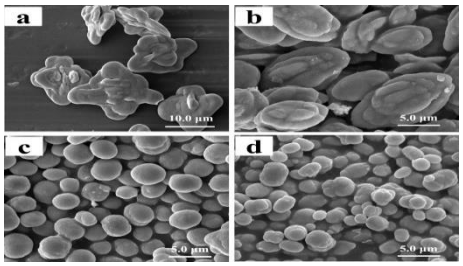

Figure 1-7 SEM of $BaSO_4$ particles obtained with PAA concentrations of: (a) 0.04 mg mL^{-1}, (b) 0.1 mg mL^{-1}, (c) 0.4 mg mL^{-1}, (d) 0.8 mg mL^{-1} [$BaSO_4$] = 5 mM, pH = 3 (Li et al., 2016).

1.4.2 Ethylenediaminetetraacetic acid (EDTA)

Zhang et al. (2011) successfully prepared spherical barium sulfate using EDTA. As shown in Figures 1-8 and 1-9, it is evident that EDTA exhibited a solid capacity to control the morphology over the crystallization of $BaSO_4$. The morphology of barium sulfate changed from plate-liked to spherical.

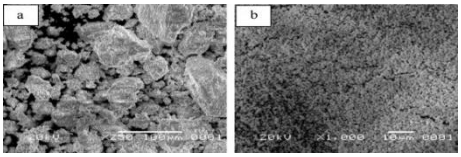

Figure 1-8 SEM image of $BaSO_4$ particles obtained in the absence (a) and presence (b) of EDTA (Zhang et al., 2011).

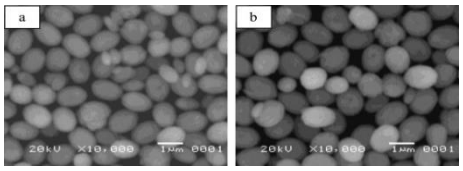

Figure 1-9 SEM image of $BaSO_4$ obtained in the presence of EDTA after aging for: (a) 1day, (b) 3days, pH=9 (Zhang et al., 2011).

During the experimental process, EDTA was first added to the $BaCl_2$ aqueous solution, and barium ions were combined with EDTA to form the Ba-EDTA complex, effectively controlling the reactivity of barium ions. Then, Na_2SO_4 aqueous solution was added to the Ba-EDTA complex's solution, causing barium sulfate's precipitation. Meanwhile, the stable $BaSO_4$ crystals were formed (Harvey, 2000). This precipitation process of $BaSO_4$ is described as the following ions equations:

$$Ba^{2+} + EDTA \rightleftharpoons Ba - EDTA \quad (1\text{-}11)$$

$$Ba - EDTA + SO_4^{2-} \rightleftharpoons BaSO_4 + EDTA \quad (1\text{-}12)$$

1.4.3 Polyethylene oxide-polypropylene oxide-polyethylene oxide (PEO-PPO-PEO)

Wang et al. (2005) used PEO-PPO-PEO as an additive to synthesize $BaSO_4$. The result showed that PEO-PPO-PEO could be an effective growth modifier for controlling the morphology and particle size of $BaSO_4$. Figure 1-10 shows the morphologies of $BaSO_4$ obtained at different additive concentrations. When the concentration of the polymers increases, the growth of $BaSO_4$ is inhibited. That is, barium sulfate gradually evolves from flakes to needles.

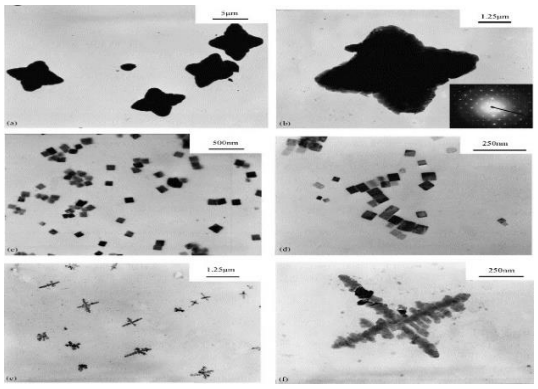

Figure 1-10 TEM images of barium sulfate obtained by using $(EO)_{20}$-$(PO)_{72}$-$(EO)_{20}$: the copolymer concentration (a, b, c) was 1 g L^{-1}, 2 g L^{-1}, 3 g L^{-1} [$BaSO_4$] = 2 mM, pH 6, Temperature = 20°C (Wang et al., 2005).

The mechanism of this formation may include two aspects. The first is referred to as the template mechanism, in which nano-particles are entirely covered with polymer molecules located in the core of micelles dominated by hydrophobic block PPO, which restricts further growth and results in small-scale particles (Zhang et al., 2003). Another one is face-selective interaction or absorption, which causes growth retardation of the face-specific (Coveney et al., 2000). The copolymers prefer absorbing on specific faces, causing the growth along these faces and exhibiting different morphologies. As the concentration of polymer increases, the polymer

assembles spontaneously to form a micelle. Hydrophobic block PPO cover the crystal nucleus to form hydrophobic nuclear, while hydrophilic block PEO diffuses in solution to promote stability and formation of the crystal structure.

1.4.4 Sodium hexametaphosphate

Gupta et al. (2010) used sodium hexametaphosphate, a water-soluble inorganic stabilizing reagent, to prepare nanosized barium sulfate particles. As shown in Figure 1-11 (a), no aggregation of particles was observed from the TEM image. From the HRTEM image given in Figure 1-11 (b), lattice fringes corresponded to the growth of $BaSO_4$ particles, indicating there was no sodium hexametaphosphate on the surfaces of $BaSO_4$ crystals. Such a $(NaPO_3)_6$ reaction system could be employed to synthesize nanosized barium sulfate particles.

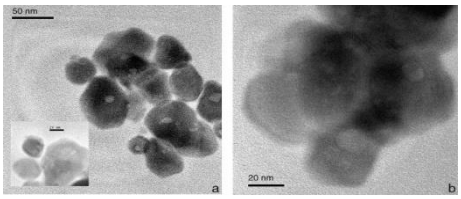

Figure 1-11 (a) Bright field TEM image of $BaSO_4$, (b) HRTEM image of lattice fringes on $BaSO_4$ surface (Gupta et al., 2010).

1.4.5 Methylglycinediacetic acid (MGDA)

Li et al. (2023) reported that MGDA is in favor of enhancing the interaction between MGDA and the crystals, causing the formation of spherical barium sulfate. As shown in Figure 1-12, as the concentration of MGDA increased, the morphology of crystals presented spherical (f), then small plate-like (e-c), and finally rice-shaped (b-a). This change in the morphology of barium

sulfate with the addition of MGDA indicated that crystal faces absorbed this additive richly, inhibiting the growth of crystal faces and leading to a change in the crystal morphology.

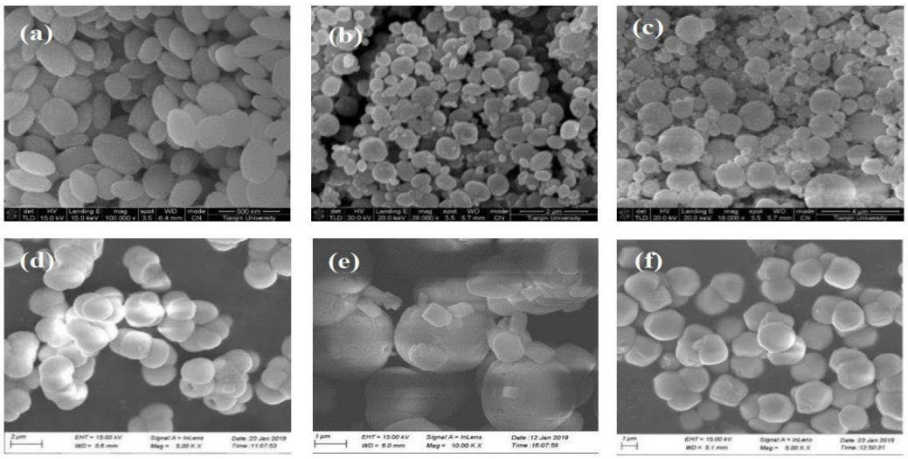

Figure 1-12 SEM of barium sulfate obtained under different additives dosages: the molar ratio of the additives to barium sulfate is: (a) 1:1; (b) 1:2; (c) 1:4; (d) 1:8; (e) 1:16; (f) 1:20, [reactant concentration 0.005M)] (Li et al., 2023).

1.5 Application of different chemical reactors in the synthesis of barium sulfate

1.5.1 Stirred Tank Reactor (STR)

Wong et al. (2003) studied the precipitation of barium sulfate in a conventional stirred tank reactor with a volume of 7.5 L to explore the effects of feed position, concentration, and rotation speed of the impeller on the properties of the precipitates. Illustrations of the feed modes are given in Figure 1-13. Two vertical feed tubes were set diametrically apart (DA) to separate the fed reactants effectively and placed midway between two baffles. The feeding pipes were placed close to the top (T), 15 mm below the initial liquid level (z=190 mm, r=88 mm), namely DA(T). The feed pipes set close to the impeller were DA(I) feed mode (z=72 mm, r=53 mm). The feeding pipes were placed close together and on the same side of the impeller, namely (CT)

feed mode. When the feed tubes were close to the top, 10 mm below the liquid surface (z=185 mm, r=53 mm), namely CT(T). When close to the impeller (z=72 mm, r=53 mm), named CT(I), the solution of 1.5 M of reactants was constantly fed nearest to the impeller (Figure 1-13b).

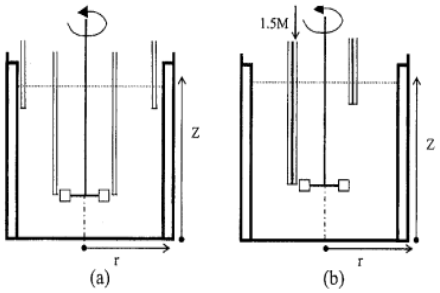

Figure 1-13 Feed positions applied in the reactor. (a) DA(T) and DA(I), (b) CT(T) and CT(I) (Wong et al., 2003).

Figure 1-14 shows the morphologies of barium sulfate produced at DA(T) feed mode. The particle size distribution was uniform at the beginning, and later, some small and rectangular crystals were observed as the precipitation proceeded, which resulted in a bimodal distribution.

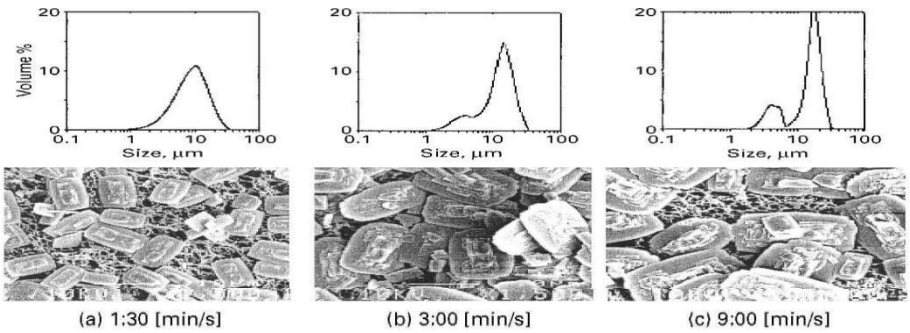

Figure 1-14 SEM and PSD of $BaSO_4$ obtained at molar ratio=1, n=150 rpm, DA(T) (Wong et al., 2003).

Figure 1-15 shows tiny and star-like crystals appearing when applying CT(I) feeding mode. However, the morphology of the products is not as uniform as that of products obtained at DA(T) feed mode, which indicates that feed locations also influence the morphology of barium sulfate products.

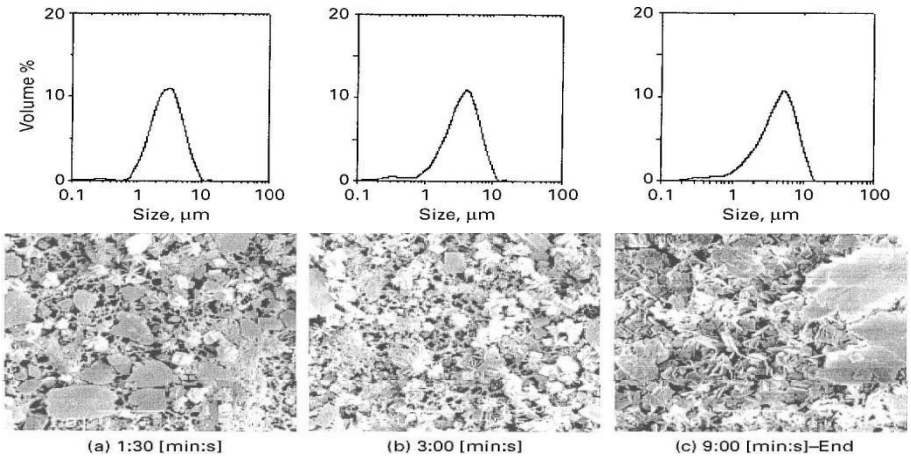

Figure 1-15 SEM and PSD of $BaSO_4$ obtained at molar ratio = 1:15, n = 150 rpm, CT(I) (Wong et al., 2003).

1.5.2 Spinning Disks Reactor (SDR)

A spinning disk reactor (SDR), as shown in Figure 1-16, is an advanced chemical processing system that utilizes a flat, rotating disc to enhance heat and mass transfer during chemical reactions. The high-speed rotation of the disc generates a strong centrifugal force, creating a thin liquid film on the reactor surface. This film is subjected to intense shear and mixing due to the frictional interaction between the liquid and the air above it, as well as the rapid movement of the disc itself. Mass transfer inside such reactors is also greatly enhanced due to the extremely high shear forces, intensifying the mixing and improving the heat/mass-transfer rates (Cafiero et al., 2002).

Figure 1-17 shows that the high shear rates in SDR break down reaction species into smaller particles. Therefore, most barium sulfate is controlled in the nanometer size range. The results were also observed in the reports of (Dehkordi and Vafaeimanesh, 2009, Farahani et al., 2017, Jahanshahi-Anboohi and Molaei Dehkordi, 2019).

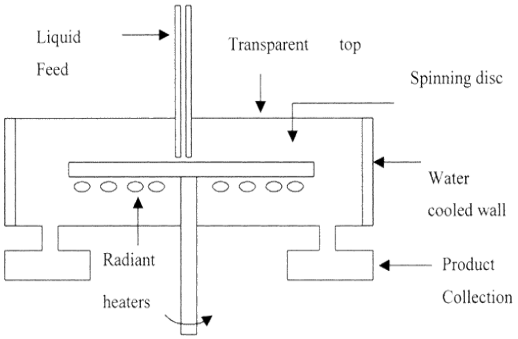

Figure 1-16 Typical representation of spinning disk reactor (Cafiero et al., 2002).

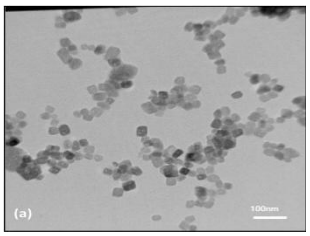

Figure 1-17 SEM of $BaSO_4$ produced by the SDR (Farahani et al., 2017).

1.5.3 Taylor-Couette Reactor (TCR)

Judat et al. (2004) investigated barium sulfate precipitation's macro/micro-mixing conditions in a Taylor-Couette reactor. This study employed a modified Taylor number (Ta^+) and the axial Reynolds number (Re_{ax}) to describe the flow conditions, as defined by Eq. 1-13 and 14.

$$Ta^+ = \frac{\omega r_i^2}{\nu} \tag{1-13}$$

$$Re_{ax} = \frac{\omega d}{\nu} \tag{1-14}$$

Where ω is the rotational speed of the reactor, w stands for the mean axial velocity in TCR, ν is the kinematic viscosity of the fluid, r_i and d are the radius of the inner cylinder and the gap width between the inner and outer cylinders.

Figure 1-18 shows the morphology of barium sulfate obtained in different macromixing conditions. This study reveals that the macromixing in such a reactor has no influence on the

particle size of barium sulfate but can significantly affect the final morphology of the products.

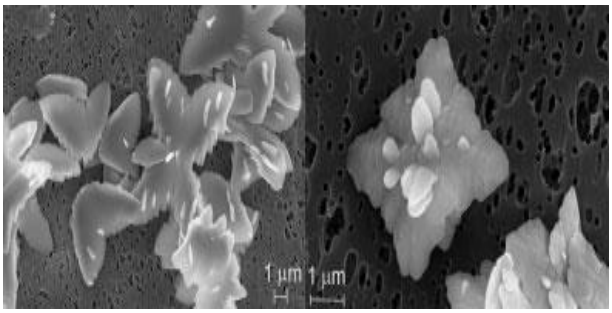

Figure 1-18 Influence of macromixing intensity on particle shape (Ta^{+}=90000): left particles produced at Re_{ax}=850, right at Re_{ax}=1200 (Judat et al., 2004).

1.5.4 Ultrasonic Reactor (USR)

An ultrasonic reactor is a specialized equipment that utilizes ultrasonic waves to induce acoustic cavitation within a liquid medium. Acoustic cavitation is a process where bubbles form, grow, and collapse rapidly in response to high-intensity ultrasound, creating localized zones of extreme temperature and pressure. These conditions facilitate a variety of physical and chemical effects that are harnessed for different applications.

Pohl et al. (2012) presented a novel reactor concept for continuous precipitation of nanoparticles, which utilized ultrasonic sound as a mixing method. Precipitation of barium sulfate was adopted as the investigated model. The geometry of this new reactor is exhibited in Figure 1-19. However, according to the report of Pohl et al. (2009), this structure (Figure 1-19 a) has two problems: the formation of recirculation and the exist of dead zones, which would cause an increase in the concentration of suspensions due to the mix of precipitated product and the reactants. Therefore, an optimized geometry with a smaller diameter of the reaction chamber (Figure 1-19 b) was applied in the experiments.

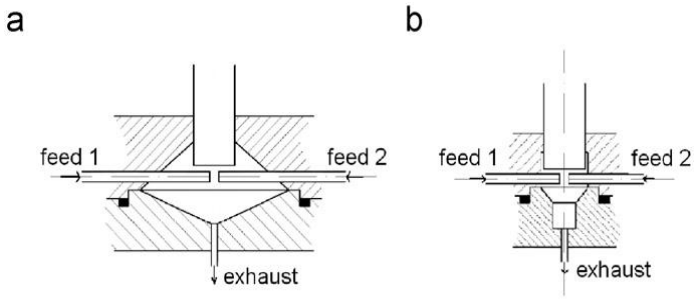

Figure 1-19 Geometries of the reactor chamber: (a) conical and (b) cavitational (Pohl et al., 2012).

From Figure 1-20, both morphologies of the products are similar, leading to the conclusion that temperature has almost no influence on the experimental results if ultrasound is not applied in the reactor. Results of experiments conducted under an ultrasonic condition are shown in Figure 1-21. More nanosized particles are produced, which indicates that ultrasound is an excellent way to synthesize the nanoparticles.

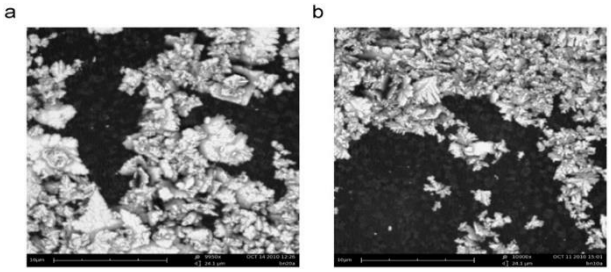

Figure 1-20 SEM of precipitated barium sulfate obtained in absence of ultrasonic power: (a) 20 ℃ and (b) 70 ℃ (Pohl et al., 2012)

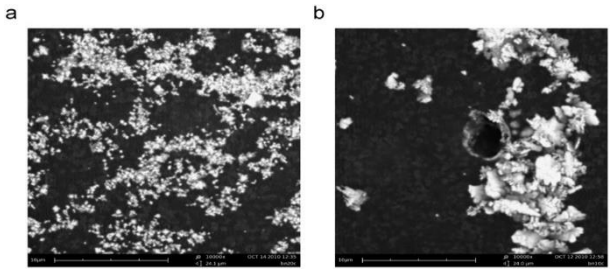

Figure 1-21 SEM of precipitated barium sulfate obtained by 160W ultrasonic power: (a) 20 ℃ and (b) 70 ℃ (Pohl et al., 2012)

1.5.5 Jet Reactors

Wojtas et al. (2020) proposed a method of large eddy simulations (LES) to predict the formation of barium sulfate crystals conducted in jet reactors (Figure 1-22).

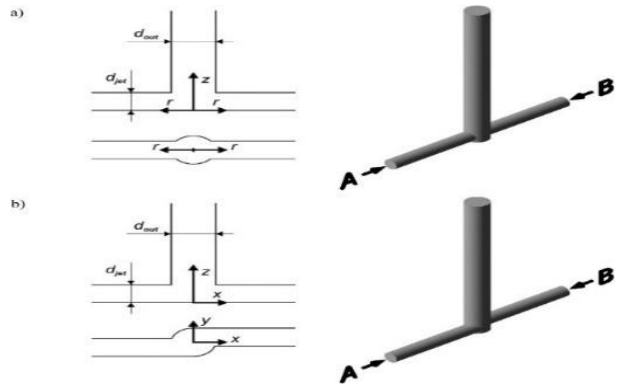

Figure 1-22 Reactor geometries: (a) T-mixer; (b) V-mixer (Wojtas et al., 2020).

The jet Reynolds number, Re_{jet} was defined as:

$$Re_{jet} = \frac{u_{jet} d_{jet} \rho}{\mu} \tag{1-15}$$

Where u_{jet} is the average velocity at the inlet, d_{jet} is the diameter of the inlet pipe, ρ and μ are the density and the dynamic viscosity of mixed solutions (at 25℃). The inlet molar concentration of reactants was equal, $c_{\alpha 0} = c_{A0} = c_{B0}$.

Figure 1-23 shows that particles exhibit the same flat shape at different mixing conditions.

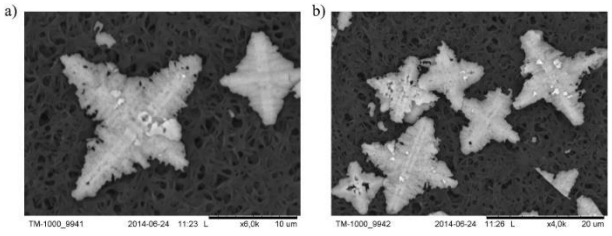

Figure 1-23 SEM images of barium sulfate obtained in T-mixer (Wojtas et al., 2020) :

(a) Re_{jet}= 300, $c_{A0} = c_{B0}$= 0.04 mol dm^{-3}; (b) Re_{jet}=1000, $c_{A0} = c_{B0}$ = 0.04 mol dm^{-3}.

1.5.6 Micromixer

Wu et al. (2013) used a micromixer (SIMM-V2) to develop an optimized preparation process for barium sulfate. Figure 1-24 exhibits the whole preparation system. From Figure 1- 25, with an increase in flow rate, the morphologies of $BaSO_4$ particles change from nanosized rice-shaped to round or spheroid-shaped. Meanwhile, the average particle size also decreases as the flow rate increases.

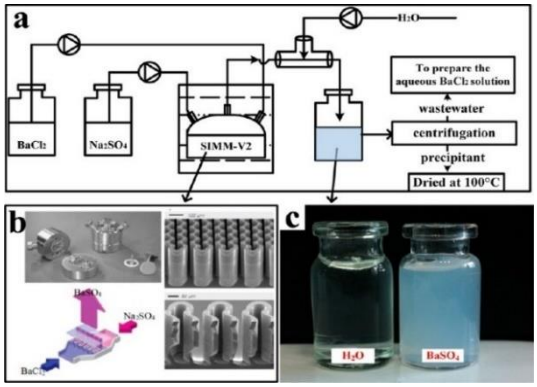

Figure 1-24 Process flow of synthesis of barium sulfate (Wu et al., 2013)

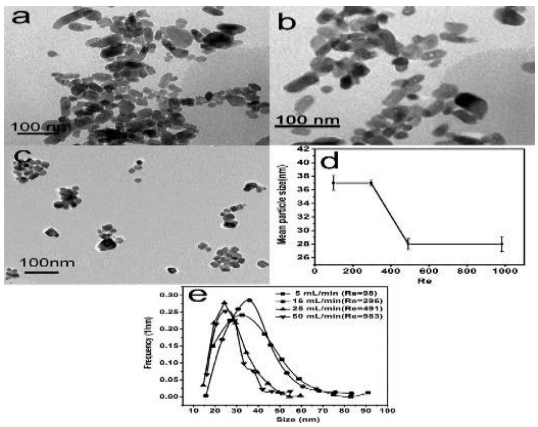

Figure 1-25 TEM of $BaSO_4$ prepared with an equal flow rate of: 5 mL/min (a), 15 mL/min (b), 50 mL/min (c); the average particle size (d) and particle size distribution (e) at different *Re* numbers (Wu et al., 2013).

1.6 Recapitulation and conclusion

Chapter 1 gives an overall introduction to the synthesis of barium sulfate, including the necessary basic concept of barium sulfate, and the effect of critical factors on morphology and particle size of barium sulfate, such as concentration, temperature, feed location, and flow rate et al. and some applications of reactors in preparation of barium sulfate. Especially, the concentration (ion ratio) of the reactants has a great influence on the morphology and the particle size of barium sulfate. According to research by Kucher et al., 2006, the morphology of barium sulfate changes from plate-like into a sort of fir cone morphology, as the ion ratio $c_{Ba^{2+}}/c_{SO_4{}^{2-}}$ increases. Other operating parameters such as feed flow rate, as discussed in section 1.5.6, an increasing flow rate leads to a decrease in average particle size.

However, few of those studies reported in detail about the preparation of flaky barium sulfate. Only a few of those studies' experiments express the possibility of preparing flaky barium sulfate. Therefore, large-scale continuous synthesis of flaky barium sulfate is the primary goal of this study, including confirming relevant parameters and exploring the feasibility of different agitating reactors in preparation for flaky barium sulfate. Then, in section 2, through a comprehensive comparison with these studied reactors, we finally can confirm that the Taylor-Couette reactor is one of the most effective equipment that can be applied in the industrial production of flaky barium sulfate. Meanwhile, we also study the characteristics of Taylor-Couette reactors, turbulence generation, and its effects on the morphology of barium sulfate in Chapter 4.

Chapter 2. Experimental investigation on the synthesis of flaky barium sulfate

2.1 Introduction

In the previous chapter, an overview of the preparation of barium sulfate is introduced. This chapter involves experimental investigations of barium sulfate synthesized in different reactors, including high-speed shear mixer (HSSM), stirred tank reactor (STR), ultrasonic reactor (USR), and Taylor-Couette reactor (TCR).

HSSM is a versatile and powerful industrial mixing equipment designed to provide efficient mixing, emulsification, and dispersion of various ingredients. This mixer is characterized by its high rotor tip speeds, ranging from 10 to 50 m/s, and very high shear rates, typically from 20000 to 100000 s^{-1}. Therefore, in this study, a typical HSSM is applied to study the influence of such violent mixing conditions on the formation of barium sulfate particles. Unlike HSSM, the mixing intensity at the multiple scales generated in a STR is relatively gender. As introduced in section 1.4.1, Wong et al. (2003) prepared flaky barium sulfate in a stirred tank reactor with a 280/500 mL volume using a propeller/anchored paddle. The ultrasonic waves formed in the USR create cavitation effects within the medium, which generate localized high pressures, temperatures, and intense shear forces, leading to a range of beneficial outcomes for some reactions. Pohl et al. (2012) prepared nanosized barium sulfate using an ultrasonic reactor. Thus, a USR was also applied to prepare nanosized barium sulfate in the present work. The Taylor-Couette reactor consists of two cylinders with a small gap between them, where a wide range of flow regimes can form. This property is beneficial for the conversion of some chemical reactions. Investigations of the formation of barium sulfate in a Taylor-Couette reactor have

been reported in recent decades by (Judat et al., 2004, Aljishi et al., 2013, Liu et al., 2020). These studies synthesized barium sulfates with a size range from nanometers to microns and different morphologies. Given those detailed research results and the characteristics of such a reactor, TCRs with different gap widths were applied to prepare barium sulfate in this study.

2.1.1 Fundamentals of High-speed Shear Mixer (HSSM)

A high-speed shear mixer is a specialized industrial mixing device designed to blend various materials quickly and efficiently by subjecting them to intense shear forces (Vashisth et al., 2021). Figure 2-1 shows the typical structure of a high-speed shear mixer used in the laboratory. This type of mixer is widely utilized in different fields, such as pharmaceuticals, chemicals, food processing, and cosmetics, where precise and thorough mixing is crucial to the quality of the desired product (Zhang et al., 2012).

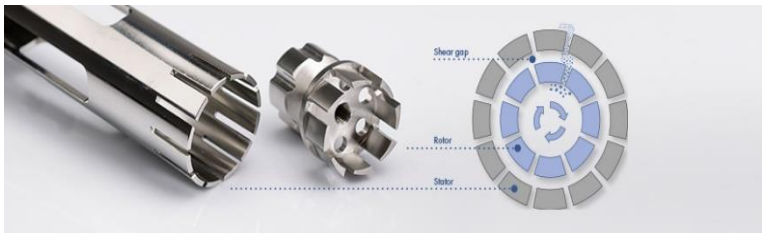

Figure 2-1 Typical structure of high-speed shear mixer (https://www.fullbrooksystems.co.uk/rotor-stator).

These mixers operate at high rotational speeds, often in the range of thousands to tens of thousands of rotation speeds per minute. Such high rotational speed generates intensive shear, which breaks down the particles and promotes mixing. The primary mechanism of mixing in high-speed shear mixers is shear force. Shear force occurs when adjacent layers of fluid move at different velocities, resulting in the stretching and deforming of fluid (Deshawar and Kumar,

2017). The vigorous shear force effectively disperses and blends different components in a mixture (Sinnott and Cleary, 2016). For example, Song et al. (2021) proposed an assisted-coprecipitation method utilizing a shear mixer, which was successfully applied to the controllable synthesis of $LiNi_{1/3}Co_{1/3}Mn_{1/3}O_2$. Ferrari et al. (2023) studied the droplet size distribution in HSSM using CFD. The research explained the properties of the pre-and post-mixing zones in a high-shear mixer, which possibly paved the way for industrial food emulsion preparation. Their efficiency in breaking down and dispersing materials makes them indispensable in industries where precision mixing is essential for product performance and characteristics.

2.1.2 Fundamentals of Stirred Tank Reactor (STR)

The stirred tank reactor is a widely utilized chemical reactor in various industrial processes that involve mixing multiple components to produce chemical products. The essential feature of this reactor is the presence of one or more agitators that stir the reactants, facilitating mixing and promoting efficient heat and mass transfer within the system.

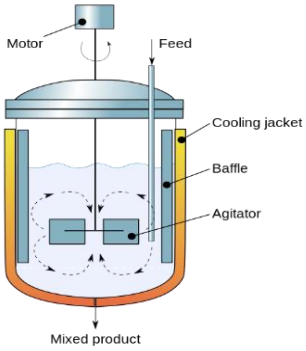

Figure 2-2 schematic diagram of a stirred tank reactor.

The performance of mixing and dispersion in such agitating reactors dramatically depends on the geometric shape of the impellers. Figure 2-3 shows some typical impellers used in practical applications.

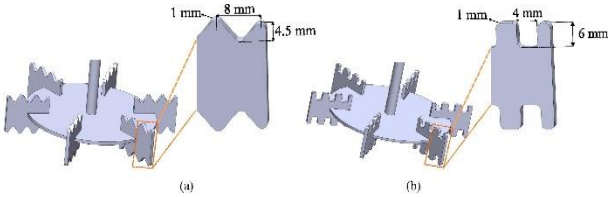

Figure 2-3 Geometries of different radial impellers: (a) V-shape and (b) U-shape impellers (Hoseini et al., 2021).

Hoseini et al. (2021) investigated the behavior of the turbulence and the power consumption of three types of impellers by utilizing CFD, as shown in Figure 2-3, which can be directly applied in industries. Amiraftabi et al. (2020) focused on studying the properties of a dual helical ribbon impeller, which provides unique and valuable guidance for application in process industries. Gu et al. (2017) reported that a punched rigid-flexible impeller handled the suspending solid-liquid phases more efficiently than a rigid impeller and rigid-flexible impeller at the same power consumption.

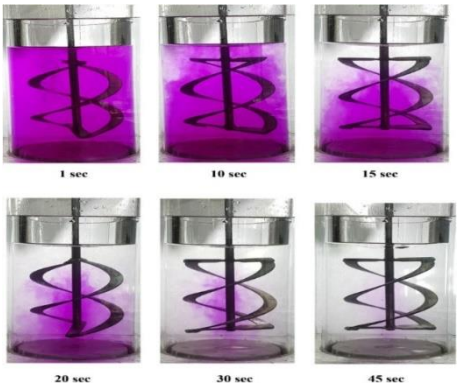

Figure 2-4 The evolution of mixed pattern generated by the dual helical ribbon impeller (Amiraftabi et al., 2020) .

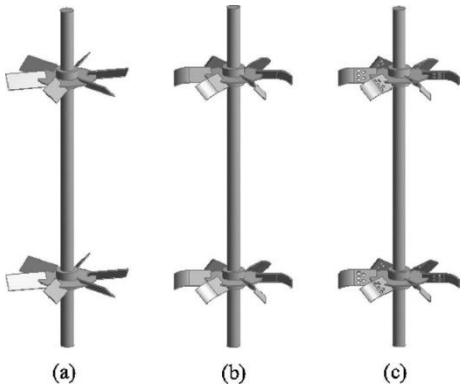

Figure 2-5 Structure diagram of the impellers: (a) Rigid impeller, (b) Rigid-flexible impeller, (c) Punched rigid-flexible impeller (Gu et al., 2017).

Besides, stirred tank reactors are also suitable for suspending solid phases and have an excellent scale-up capacity (Cherkasov et al., 2023). For the solid phase of dilute suspensions in STRs, Hartmann et al. (2006) investigated the dispersion process of solid particles suspended with the help of a large eddy simulation. Lamberto et al. (2001) and Guha et al. (2007) systematically studied the influence of impeller types on the occurrence of solids “just-suspension” speed, which pointed out that a “globally chaotic” flow could be generated through a relatively lower rotation speed settings. Given those regnant characteristics of the stirred tank reactors, a conventional simple stirred tank vessel was also applied to prepare barium sulfate in this research work.

2.1.3 Fundamentals of Ultrasonic Reactor (USR)

Figure 2-6 shows that an ultrasonic reactor is a specialized device that utilizes ultrasonic waves for various processes, such as mixing, dispersing, emulsifying, and accelerating chemical reactions (Asgharzadehahmadi et al., 2016).

Figure 2-6 Typical ultrasonic reactor (http://www.tissuly.com/sonics/product).

The application of ultrasonic energy in reactors has gained popularity across different industries, including chemistry, materials science, pharmaceuticals, and food processing, due to its ability to enhance process efficiency and produce unique effects that are difficult to achieve through conventional methods (Delacour et al., 2020, Sajjadi et al., 2017). Vishwakarma and Gogate (2017) successfully developed an ultrasonic assisted-cooperation approach to cooling crystallization of oxalic acid, of which the narrow particle size was significantly smaller than that obtained through conventional methods.

The core technology of ultrasonic reactors is the generation of high-frequency sound waves (above 20 kHz). These waves create pressure variations in liquids, leading to the formation and collapse of tiny bubbles, a phenomenon named cavitation. The cavitation process breaks down agglomerates and particles, leading to a more uniform distribution of components in the mixture, which is particularly beneficial in applications such as nanoparticle synthesis and dispersion of additives in liquids (Mistewicz et al., 2021). Overall, ultrasonic reactors can accelerate chemical reactions by providing additional energy input through cavitation, which can lead to faster

reaction rates and more complete conversions, which enhances the multiphase process, especially for the immiscible fluid-fluid to fluid-solid systems (Dong et al., 2020). In this research, a handheld ultrasonic generator is applied in research on the synthesis of barium sulfate.

2.1.4 Fundamentals of Taylor-Couette Reactor (TCR)

Basic

A Taylor-Couette reactor (TCR) consists of two concentric cylinders, with the inner cylinder capable of rotating independently of the outer one (Fig. 2-7). When the inner cylinder rotates, it imparts angular momentum to the fluid, producing different flow patterns suitable for chemical reactions and crystallization processes.

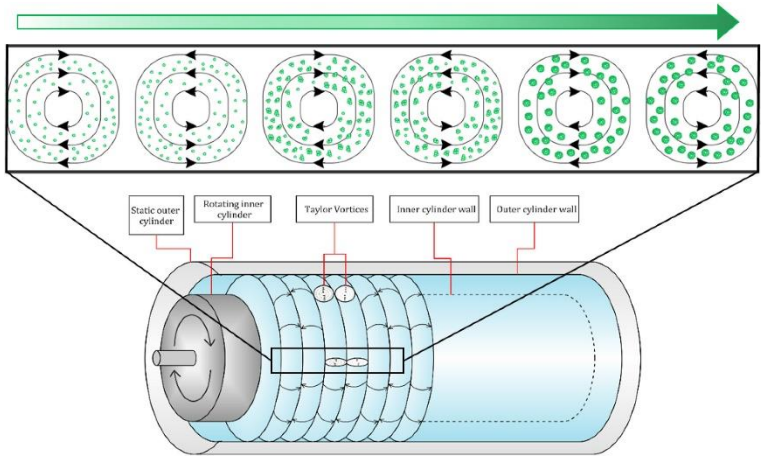

Figure 2-7 Schematic representation of flow pattern forming in a Taylor-Couette reactor (Seenivasan et al., 2021).

TCR is a good option when the reaction systems contain fragile particles due to its relatively gentle but efficient mixing properties (Seenivasan et al., 2021, Giordano et al., 2000). AlAmer et al. (2018) developed a continuous process of the oxidation of graphite (GtO) flakes by using

Taylor-Couette reactor, in which high-quality, structurally uniform GtO was prepared, and the reaction time was remarkably shortened from hours to minutes. Compared with a typical mixing tank reactor, TCR combines excellent mixing characteristics with limited back mixing (Schrimpf et al., 2021). Therefore, the efficiency of the phase transformation process in TCR is several times faster than that in some conventional reactors. The flow pattern in TCR plays an essential role in determining the size and morphology of the products (Wu et al., 2015). Wang and Tao (2022) prepared a kind of micro-/nanohydroxyapatite successfully by using TCR. The results reveal that TCR can effectively improve the performance of the mixing and the distribution of the flow field, which exhibits the flexibility of TCR in application to the synthesis of micro/nanoparticles. As mentioned, the Taylor-Couette reactor is a promising and valuable technology in the large-scale production of micro/nanomaterials (Tang et al., 2019).

Taylor-Couette flow

The relative rational motion between the inner and outer cylinders in a Taylor-Couette reactor and the fluid viscosity leads to a range of flow regimes. Taylor number (*Ta*) and Reynolds number (*Re*), defined by the following equations, are often used to characterize the state of the flow.

$$Ta = \left(\frac{dr_i\omega}{v}\right)^2 \cdot \frac{d}{r_i} \tag{2-1}$$

Where d is the gap width between the inner and outer cylinder of TCR, r_i is the radius of the inner cylinder, ω represents the angular velocity, and v is the kinematic viscosity of the fluid. *Re* is defined as the following (Majji and Morris, 2018, Nemri et al., 2016, Nemri et al., 2013)

$$Re = \frac{dr_i\omega}{\nu} \tag{2-2}$$

Where d, r_i, ω, and ν are the same as the defined as the above-mentioned.

The flow is laminar and axisymmetric at low *Re*, which is called Circular Couette Flow (CCF). As the *Re* increases beyond a critical value, $Re_{c,1}$, the flow becomes unsteady, dominated by a series of stable toroidal vortices, namely Taylor Vortex Flow (TVF). When *Re* keeps on increasing until it exceeds a second critical *Re* value, $Re_{c,2}$, the flow starts to lose its axisymmetry due to the oscillations in the position of vortices caused by azimuthal waves traveling through the fluid (Akonur and Lueptow, 2003, Wereley and Lueptow, 1998). When the vortices transport fluid from the inner cylinder surface with high angular velocity into the center of the vortices, strong azimuthal jets can be formed, resulting in an instability of the flow (Coughlin and Marcus, 1992). This state is called Wavy Vortex Flow (WVF). A single temporal frequency and wavelength can be used to describe this flow pattern. Further increase in *Re* is associated with more transitions, where more temporal frequencies occur, ultimately leading to turbulence (Andereck et al., 1986, Dutcher and Muller, 2009).

Nemri et al. (2013) proposed a series of flow instabilities using a visualization method. Spectral analysis was applied to determine transition Reynolds numbers and structural properties of these flow states. Figure 2-8 shows the visual structure of the flow pattern, ranging from Taylor vortex to turbulent flow. η is the ratio of the inner cylinder's radius (R_i) to the outer cylinder's radius (R_o). Majji and Morris (2018) investigated the inertial migration of neutrally buoyant particles in a Taylor-Couette reactor, as shown in Figure 2-9.

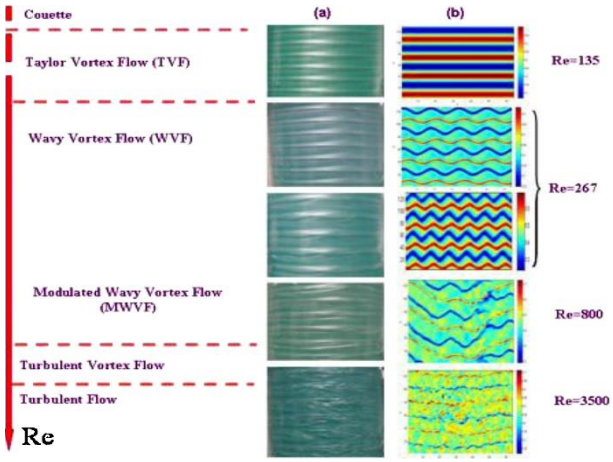

Figure 2-8 Illustration of different flow regimes in a Taylor-Couette reactor ($\eta = \frac{R_i}{R_o} = 0.85$): (a) Visualization of experiments and (b) CFD simulations (Nemri et al., 2013).

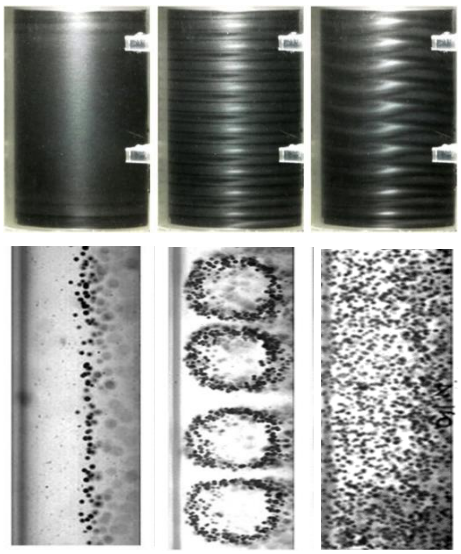

(a) (b) (c)

Figure 2-9 Flow structures and the final distribution of particles in a Taylor-Couette reactor. (a) circular Couette flow (CCF), (b) Taylor vortex flow (TVF), (c) wavy vortex flow (WVF) (Majji and Morris, 2018)

In CCF, due to the competition between the shear gradient of the flow and the wall interactions, particles migrate to a position near the middle of the fluid (Figure 2-9-a). In TVF, the migration of particles is dominated by the shear gradient and wall interactions due to the vortex motion,

resulting in a circular equilibrium area in each vortex (Figure 2-9-b). Being different from CCF and TVF, where the azimuthal direction is invariable, due to the existence of azimuthal waves in WVF, the particles cannot reach a stable equilibrium position due to the shorter migrating time, leading to a state of complete and uniformly mixing in the annular region (Figure 2-9-c).

2.2 Synthesis of barium sulfate in High-speed shear mixer

2.2.1 Experimental setup

The experimental facilities (Figure 2-10) include two high-precision plunger pumps with a flow range of 1-200 mL/min, a flow accuracy of up to ±0.005mL/min, and a repeatability of 0.5%, and a high-speed shearing mixer (HSSM) with a rotational speed range of 300-23000 rpm, and the stator diameter is 18mm. The reaction occurs in a plexiglass container with a diameter of 60 mm. The reactant inlet is set at a height of 65 mm from the base of the container, and the mixture outlet is set at a height of 85 mm from the base of the container. The rotor is positioned with a 10mm clearance from the bottom of the container. Table 1 gives details of the high-speed shear mixer used in this investigation.

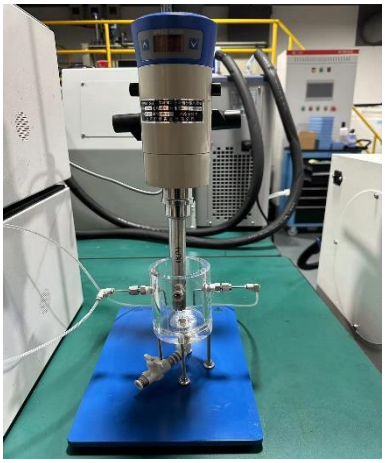

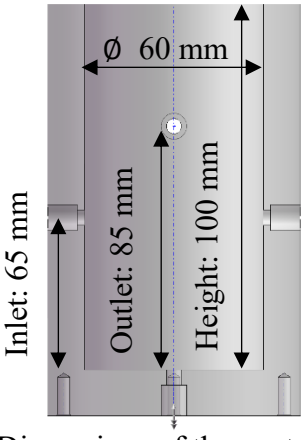

Dimensions of the container

Figure 2-10 High-speed shear mixer.

Table 1

HUXI-FJ200-SH Laboratory digital high-speed homogenizer

Power: 200 W	Setting ratio: intermittent	Rotation speed: 300-23000 rpm
Voltage: 220 V	Frequency: 50 HZ	Insulation level: E

The morphology of barium sulfate particles is achieved by using a Thermo Scientific Phenom Pro scanning electron microscope (SEM) at 15kV/ Zeiss sigma VP scanning electron microscope at 15kV. Before the microscopy, all samples need to be coated with a thin gold film under a vacuum as barium sulfate powder is nonconducting. The particle size distribution (PSD) is achieved by a Bettersize 2000 laser particle size analyzer and (the surface area) average particle size d_{32} (or called Sauter mean diameter) can be output directly from the computer. Experimental materials, including barium chloride dihydrate (99%) and sodium sulfate (99%), were provided by our partner company, and the pure water for the preparation of solutions was taken from HHITECH Basic-Q15 Laboratory water purification system (The pure water is also known as RO water: the water is filtered through a reverse osmosis membrane, the pore size of which is generally between 10A and 100A and it can remove more than 95% of the ionic impurities). The barium sulfate precipitation in this study was described as the mentioned Eq. 1-8.

2.2.2 Experimental procedure

The preparation of barium sulfate was continuously synthesized in the high-speed shear mixer (HSSM) by the violent shearing action at room temperature (22℃). Before the experiment, the plexiglass container was prefilled with 150 mL of pure water. Then, 100 mL $BaCl_2$ and Na_2SO_4 aqueous solution were simultaneously injected into the container through a PTFE tube at the set flow rate by two individual plunger pumps. After feeding, the resulting products were filtered by a vacuum filer to collect the barium sulfate produced. Finally, the filtered products

were put into a conventional oven and dried at 70℃ for 12 hours. The feeding modes applied in this study are exhibited in Figure 2-11, and other operation parameters are listed in Table 2.

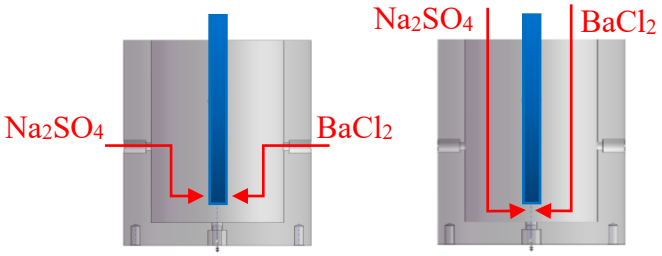

(A) (B)

Figure 2-11 Illustration of the feeding modes applied in the HSSM: (A): feed inlet (red triangle) locates close to the rotator of the HSSM, (B): feed inlet (red triangle) locates under the rotator of the HSSM.

Table 2

Experimental conditions applied in the high-speed shear mixer

No. of exp.	Rotational speed (rpm)	Total flow rate (mL/min)	Feeding mode	Concentration of $BaCl_2$ (mol/L)	Concentration of Na_2SO_4 (mol/L)
H1	6500	20	A	0.1	0.1
H2	9500	20	A	0.1	0.1
H3	10500	20	A	0.1	0.1
H4	10500	20	B	1	1

2.2.3 Results and Discussion

Figure 2-12 exhibits the SEM images (left) and the corresponding particle size distribution diagrams (PSD) (right) of barium sulfate obtained at different rotation speeds and feed locations

in the high-speed shear mixer. In the case of H1, barium sulfate particles present rectangular shapes with blunt edges, giving an average size of 3.4 μm. Some tiny crystals are attached to the surfaces of the particles. Small, aggregated particles can be observed from the SEM, which gives feedback in the PSD diagram, namely the appearance of a small bimodal. With an increase in rotation speed, the surfaces of the flakes become smooth, and no tiny, aggregated particles are attached to the surfaces. The bimodal distribution is more prominent, and the particle size is around 3 μm (H2). When the rotation speed reaches 10500 rpm (H3), the morphology of the particles exhibits an irregular round shape, and more small particles are attached to the surfaces of the round particles, giving an average size of 2.3 μm. When the concentration of the reactants increases to 1 mol/L and the feed ports are placed under the rotator head (H4), spherical aggregating particles can be observed, giving an average particle size of 1.8 μm.

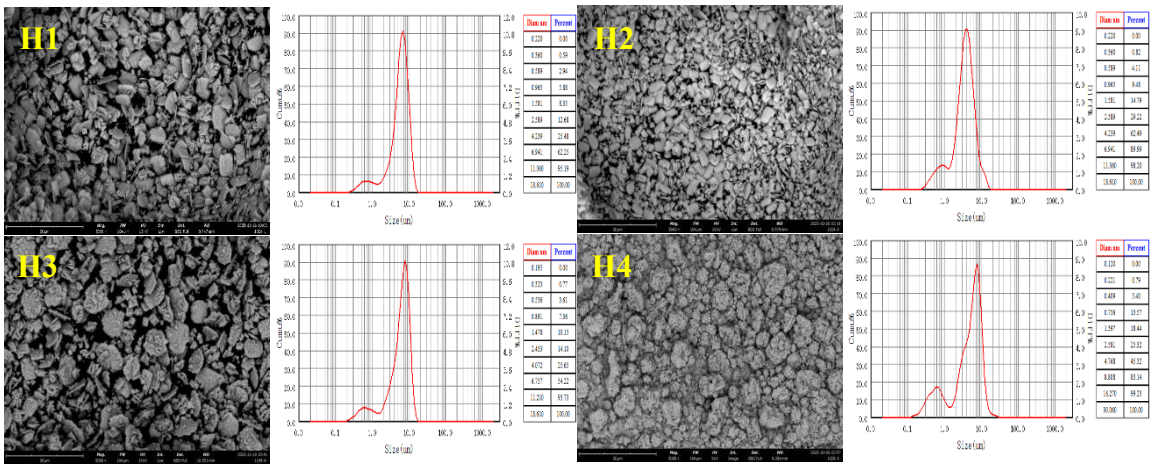

Figure 2-12 SEM and PSD of barium sulfate obtained at different rotation speeds in the high-speed shear mixer: H1: 6500 rpm; H2: 9500 rpm, H3: 10500 rpm, [$BaSO_4$=0.1 mol/L, Feeding mode: A]; H4: 10500 rpm, [$BaSO_4$=1 mol/L, Feeding mode: B].

It is also worth noting that a bimodal distribution appears in each particle size distribution diagram, which indicates that the shear force distribution in the high-speed shear mixer is

complex, resulting in such a phenomenon. Besides, an erosion mechanism could be employed to describe the breakage and agglomeration of barium sulfate particles in the high-speed shear mixer (Bałdyga et al., 2008). The deagglomeration of the very large, agglomerated particles is slower, while such a process of the large, agglomerated particles is faster. The forces bonding the fragile, very large agglomerates are probably feeble. Then, the erosion of large agglomerates would be predated by the rupture of very large agglomerates, resulting in different-sized agglomerates of barium sulfate.

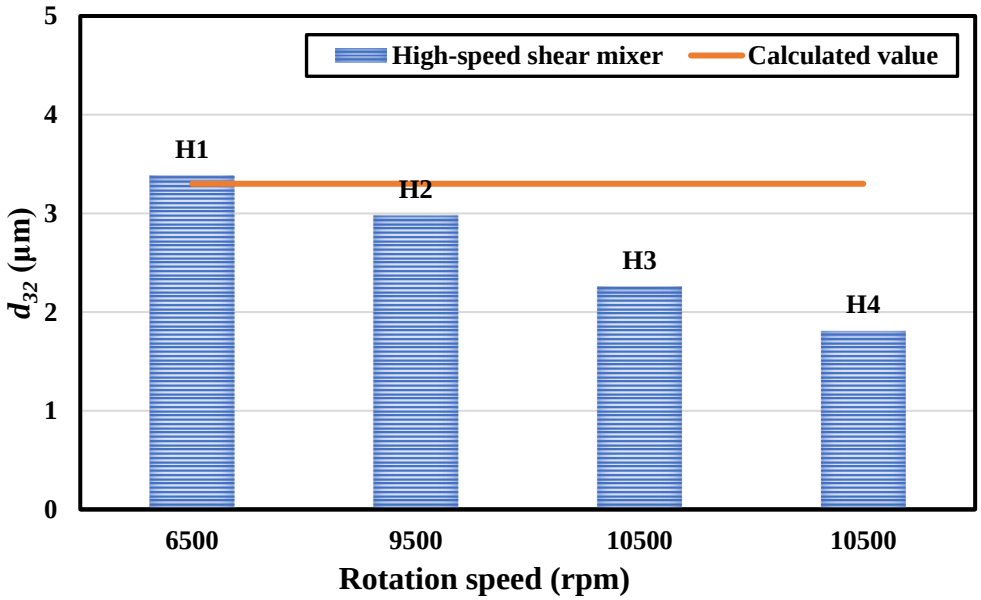

Figure 2-13 Average particle size (d_{32}) of barium sulfate obtained at different rotation speeds in the high-speed shear mixer.

As shown in Figure 2-13, the average particle size of barium sulfate decreases with increasing rotation speed of HSSM due to a more potent formed shearing force. The average particle size (d_{32}) for practical applications depends on the relative magnitude between the droplet size (d) and η_K (the kolmogoroff length scale, m). Padron (2005) summarized three mechanistic equations for correlating d_{32} in different sub-ranges:

Inertial sub-range: $(L_T \gg d \gg \eta_K)$ $\frac{d_{32}}{D} = C_1 We^{-3/5}\left[1 + C_2 Vi(\frac{d_{32}}{D})^{1/3}\right]^{3/5}$ (2-3)

Inertial stress: $(d < \eta_K)$ $\frac{d_{32}}{D} = C_1 (WeRe)^{-1/3}\left[1 + C_2 ViRe^{1/2}(\frac{d_{32}}{D})\right]^{1/3}$ (2-4)

Viscous stress: $(d \ll \eta_K)$ $\frac{d_{32}}{D} = C_1 We^{-1} Re^{1/2}\left[1 + C_2 ViRe^{-1/4}\right]$ (2-5)

Where C_1 and C_2 are the model constants, L_T represents the turbulent macro length scale, d is the droplet size, D is the diameter of the impeller, *We*, *Re,* and *Vi* are the Webber number, Reynolds number, and the viscosity group. Eq. 2-3~2-5 are generally applicable to the emulsion system, such as the Kerosene-Water system, clean and surfactant system et al. Especially the limits of $Vi \to 0$ or $Vi \to \infty$ could be employed in the case of inviscid or highly viscous droplets. Alternatively, d_{32} can be described by an empirical equation correlated with the energy density (Zhang et al., 2012).

$$d_{32} \propto C \cdot E_V^b = C \cdot (\frac{P}{Q})^b \quad (2\text{-}6)$$

Where C is a constant, determined by the viscosity of the fluid, E_V is the energy density (J/m^3), P is the total input power (W), Q is the volumetric flow rate (m^3/s), and b is a second constant. In this study, take experiment "H1" as an example, the average particle size can be calculated from Eq. 2-6. Due to the low volume fraction of the particles (< 5%), the resulting mixture solution is assumed as water, thus constant C can be taken as 1×10^{-3} (Pa·S), P is 200 (W), Q is 3.3×10^{-7} (m^3/s), given the experiment is continuous and the residence time of droplets in the dispersing zone lies in the order of milliseconds to tenths of a second as is usually found in commercial continuous emulsification, and the turbulence is decisive for droplet disruption,

thus b is in the order of 0.4 (Karbstein and Schubert, 1995).

Thus, $d_{32} = 1 \times 10^{-3} \left(\frac{200}{3.3 \times 10^{-7}}\right)^{0.4}$ =3.3 (μm), which is nearly close to the measured value of 3.4 (μm), showing the universal applicability of Eq. 2-6 in such a case. However, in the case of H3, H4 there is a margin of error between the measured value and the calculated value. It is probable that the role of turbulence changes at such a high rotation speed, thus Eq. 2-6 would be not suitable for these cases, but he calculated values of these two cases are still close, implying that Eq. 2-6 were also applicable to cases H3 and H4 if the value of b can be adjusted correctly.

2.3 Synthesis of barium sulfate in Stirred tank reactor.

2.3.1 Experimental setup

The reaction system includes two high-precision plunger pumps with a flow range of 1-200 mL/min, a flow accuracy of up to ±0.005mL/min, and a repeatability of 0.5%, an electric agitator with a rotational speed range of 100-2000 rpm (Figure 2-14), and a glass beaker with a diameter of 80 mm and height of 120 mm. The experiment is conducted in a plexiglass container (the same one used in HSSM) with a propeller and a glass beaker with an anchor paddle. Table 3 gives the detailed information about the electric agitator used in this study.

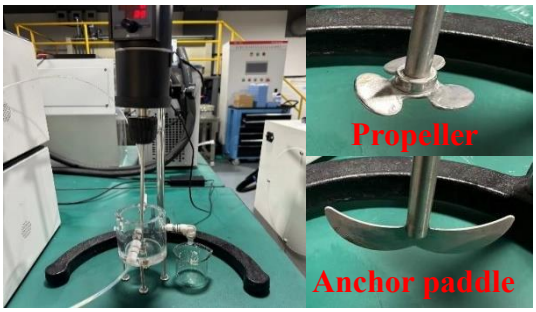

Figure 2-14 Stirred tank reactor with different impellers.

Table 3

Parameters of the applied electric agitator

Model:	XIUILAB-JB-80SH
Max Power of motor:	80 W
Rotational speed range:	100-2000 rpm
Diameter of propeller:	Ø 29 mm
Diameter of anchor paddle:	Ø 64 mm

2.3.2 Experimental procedure

The main parameters studied in this study were the stirrer speeds and the configuration of impellers. Two types of impellers (propeller and anchor paddle), as shown in Figure 2-15, were used in this study to synthesize the barium sulfate.

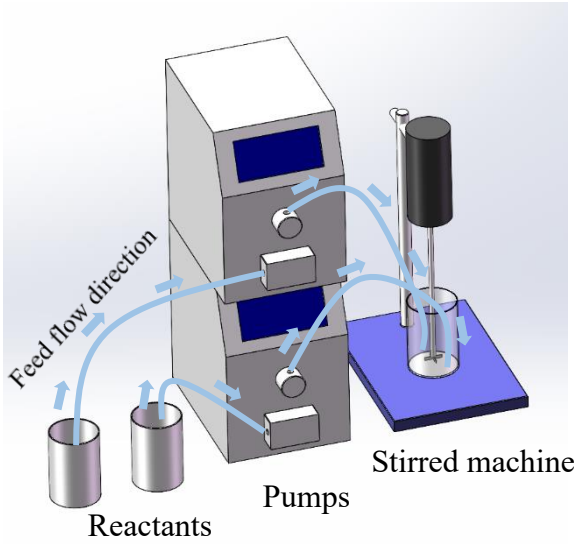

Figure 2-15 Schematic illustration of experiment process.

The experiment was carried out at room temperature (22°C), at the beginning, a 500 mL glass beaker was prefilled with 150 mL pure water and placed in a water bath until the desired temperature was reached. Then, 150 mL $BaCl_2$ and 150 mL Na_2SO_4 solution were simultaneously fed into the glass beaker through a Polytetrafluoroethylene (PTFE) tube at the desired flow rate by two individual plunger pumps. The PTFE feeding tube with a diameter of 3 mm was carefully placed against the inner wall of the beaker to reduce its interference with the flow dynamic. The synthesis of barium sulfate was conducted in STR at different rotation speeds. After completing solution feeding and waiting an additional 9 minutes to achieve a better mixing result, then the mixture was filtered by a vacuum filer to collect the barium sulfate produced. Finally, the filtered products were put into a conventional oven and dried at 60°C for

12 hours to reduce energy consumption, because, during the literature review, different drying temperatures were applied in different studies, which suggests that the processing of drying involves a common physical transformation. The fact that the collected barium sulfate can also be dried completely at such a temperature. For future industrial production, the drying process will be considered furtherly to save energy. The operation parameters are listed in Table 4.

Table 4

Experimental conditions applied in the stirred tank reactor

No. of exp.	Rotational speed (rpm)	Total flow rate (mL/min)	No. of feed position	Concentration of $BaCl_2$ (mol/L)	Concentration of Na_2SO_4 (mol/L)
S1-a S1-b	300	40	-	0.1	0.1
S2-a S2-b	500	40	-	0.1	0.1
S3-a S3-b	800	40	-	0.1	0.1
S4-a	1000	40	-	0.1	0.1

2.3.3 Results and Discussion

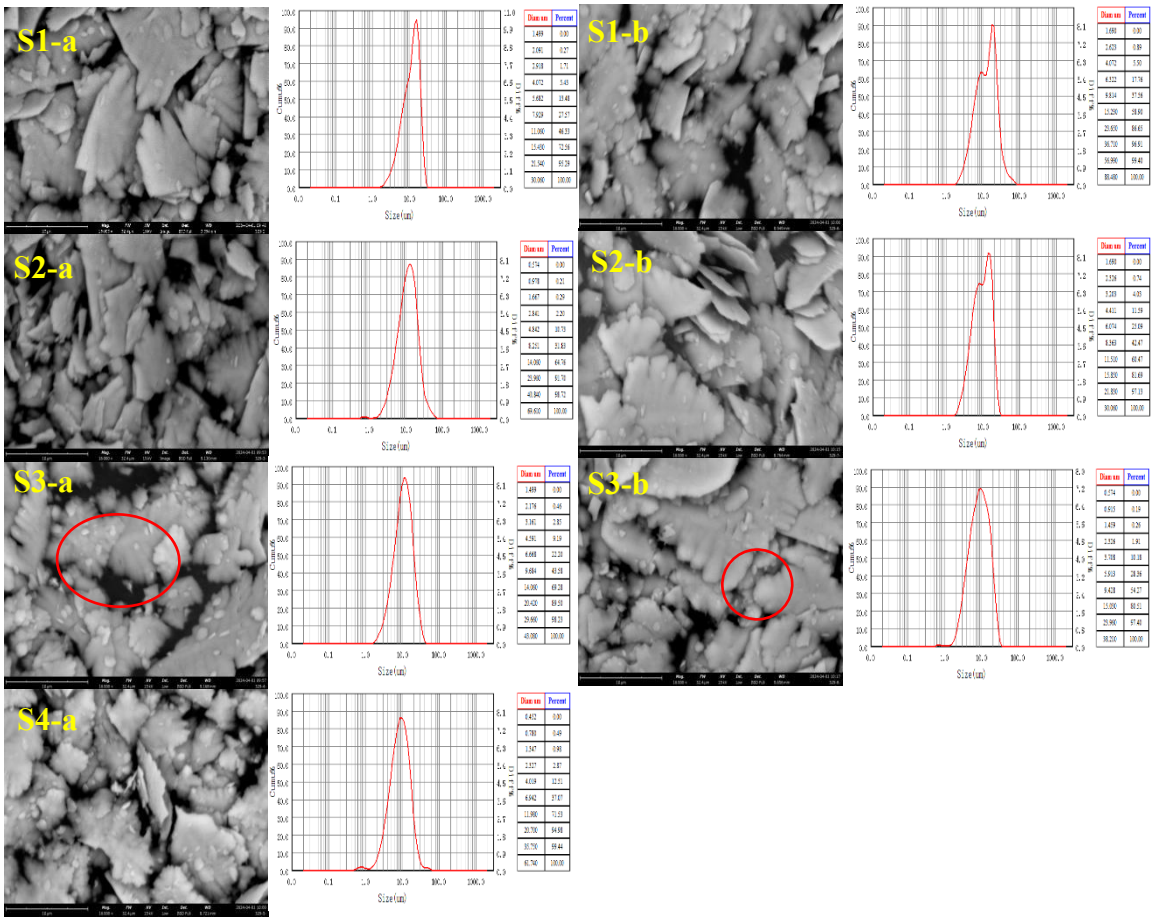

Figure 2-16 SEM and PSD of barium sulfate obtained at different rotation speeds in the stirred tank reactor: S1-a: 300 rpm, S2-a: 500 rpm, S3-a: 800 rpm, S4-a: 1000 rpm; S1-b: 300 rpm, S2-b: 500 rpm, S3-b: 800 rpm; [-a: by using propeller, -b: by using anchor paddle, Total flow rate: 40 mL/min, Concentration: 0.1 mol/L]

Figure 2-16 shows SEM images (left) and the corresponding particle size distribution (PSD) diagrams (right) of barium sulfate obtained at different rotation speeds in the stirred tank reactors by using different impellers. Experiments S1~4-a are conducted in the stirred tank reactor by utilizing the propeller. In S1-a, flaky barium sulfate particles with sharp edges are produced, giving an average size of 8.7 μm. The surface of the particles is attached with some tiny crystals. As the rotation speed increases to 500 rpm, the morphology of barium sulfate

particles is still quite irregular (S2-a). When the rotation speed reaches 800 rpm, blunt edges of the particles appear instead of the previous sharp edges (S3-a). Meanwhile, the growth of the particles seems to be inhibited in such experimental conditions because the apparent crack in the surface of the crystals can be observed, and the edges look loosened, as shown in the red circle in S3-a. At the highest rotation speed (S4-a), the morphology of barium sulfate is similar to that in S3-a. There is a slight decrease in the particle size, and the final average particle size is about 6.5 μm. Experiments S1~3-b are conducted in the stirred tank reactor by utilizing the anchored paddle. The morphology of barium sulfate obtained in S1~3-b is like that obtained in S1~4-a. Barium sulfate particles with blunt edges and cracks on the surface can also be observed. Probably, before the completion of the crystals' growth, these aggregated crystals had been transported to the upper transitional zone, as shown in Fig. 2-17. Thus, the reduction in the number of crystals limits the growth and aggregation of the particles, resulting in a noticeable crack on the surface of the particles.

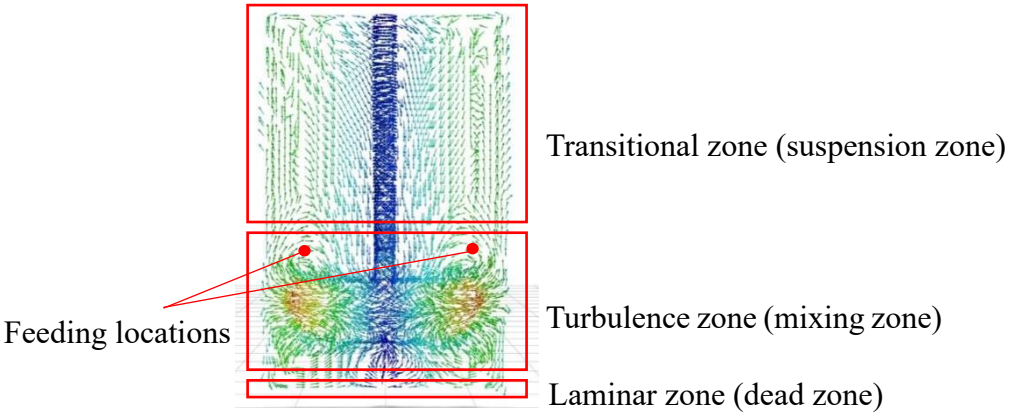

Figure 2-17 Simulation result of the velocity field in the stirred tank reactor used in this study. Stationary zone: Ø80 × 120 mm, Rotationary zone: Ø70 × 33 mm, [Operating conditions: Anchor paddle in the glass beaker, 300 rpm]

In general, there is no apparent difference in morphology between these two groups of products, which all show a plate-like shape with fine cracks on the surfaces. Figure 2-18 shows the average particle size of the products obtained at different rotation speeds by using the propeller and the anchor paddle. Both average particle sizes of the products present a decreasing trend as the rotation speed increases.

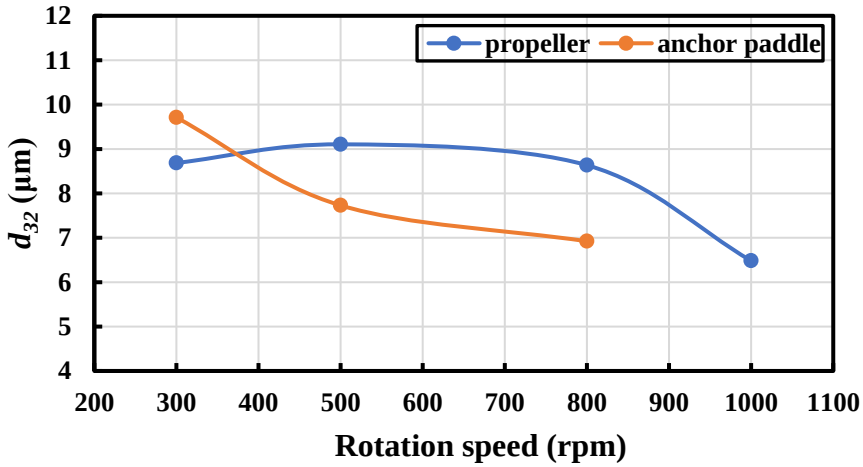

Figure 2-18 Average particle size (d_{32}) of barium sulfate obtained at different rotation speeds by using different impellers in the stirred tank reactor.

It is worth noticing that the average particle size of barium sulfate obtained by using a propeller is generally 1 μm bigger than that obtained by using an anchored paddle, which shows that the shear mixing generated by using an anchored paddle is more violent than that by using a propeller, resulting in a smaller particle size.

2.4 Synthesis of barium sulfate in Ultrasonic reactor

2.4.1 Experimental setup

The reaction system (Figure 2-19) includes two high-precision plunger pumps with a flow range of 1-200 mL/min, a flow accuracy of up to ±0.005mL/min, and a repeatability of 0.5%, and a repeatability of 0.5%, an ultrasonic reactor (Figure 2-19), and a plexiglass container (the same one used in HSSM). Table 5 gives detailed information about the ultrasonic generator used in this study.

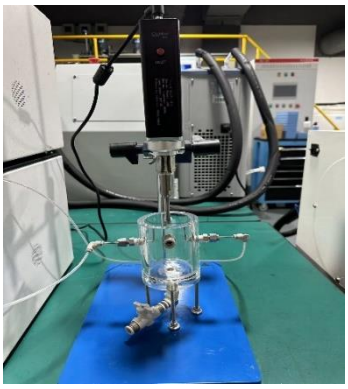

Figure 2-19 Ultrasonic reactor

Table 5

Product model:	OuHor-H150
Nominal Power:	150 W
Nominal frequency:	30 KHz
Input power:	24 V DC
Processing capacity:	500 uL-200 mL

2.4.2 Experimental procedure

The experiments were conducted at room temperature (25℃). Firstly, the plexiglass container was prefilled with 150 mL pure water, and the head of the ultrasonic generator was placed close to the top, 5 mm below the initial liquid level. The volt of the ultrasonic generator was set at 20 Volts according to the operation manual. Then 250 mL $BaCl_2$ and 250 mL Na_2SO_4 solutions were simultaneously injected into the container through a PTFE tube at the set flow rate by two individual plunger pumps. The resulting products were filtered by a vacuum filer to collect the barium sulfate produced. At last, the filtered products were put into a conventional oven and dried at 70℃ for 12 hours. The main parameters applied in this study are listed in Table 6.

Table 6

Experimental conditions in the ultrasonic reactor

No. of exp.	Ultrasound properties (KHz/V)	Total flow rate (mL/min)	No. of feed position (#)	Concentration of $BaCl_2$ (mol/L)	Concentration of Na_2SO_4 (mol/L)
U1	30/20	20	BF	0.1	0.1
U2	30/20	20	BC	0.1	0.1
U3	30/20	20	MF	0.1	0.1
U4	30/20	20	MC	0.1	0.1
U5	30/20	20	TF	0.1	0.1
U6	30/20	20	TC	0.1	0.1

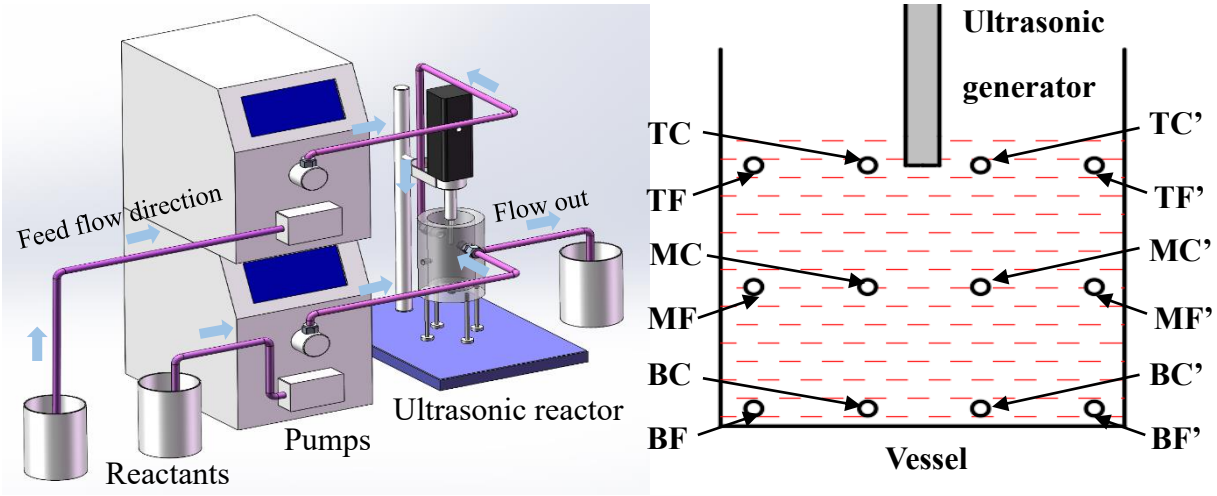

Figure 2-20 Illustration of the continuous synthesis process (left) and feeding positions (right) applied in the experiment.

Figure 2-20 illustrates the different feed locations set in this investigation. TC: the feed port is at the top of the vessel and close to the ultrasonic generator. TF: the feed port is at the top but far from the ultrasonic generator. MC: the feed port is in the middle of the vessel and close to the ultrasonic generator. MF: the feed port is in the middle but far from the ultrasonic generator. BC: the feed port is at the bottom of the vessel and close to the ultrasonic generator. BF: the feed port is at the bottom but far from the ultrasonic generator. Reactant solutions are injected from these positions by pumps, and then the resulting mixture flows out from the outlet of the container simultaneously, namely the whole experiment is continuous.

2.4.3 Results and Discussion

Figure 2-21 shows SEM images (left) and the corresponding particle size distribution (PSD) diagrams (right) of barium sulfate obtained at different feed locations in the ultrasonic reactor. In experiments U1 and U2, the surface of the particles is attached with many aggregated tiny particles, and many small, agglomerated particles result in a bimodal distribution in the PSD

diagrams, both giving an average particle size of 1.6 μm. In U3 and U4, there is a great reduction in the number of tiny particles attaching to the surface of the rectangular particles. Thus, the percentage of another unimodal decreases from 20% (in U2) to 10% (in U4). Rectangular barium sulfate particles with tiny particles on their surface can still be observed at TF feeding mode (U5). However, the number of tiny particles on the surface of the particles obtained in the TC feeding mode (U6) is much less than in any other feeding mode. These particles obtained in U6 have a smoother surface and an excellent unimodal size distribution, giving an average particle size of 1.4 μm.

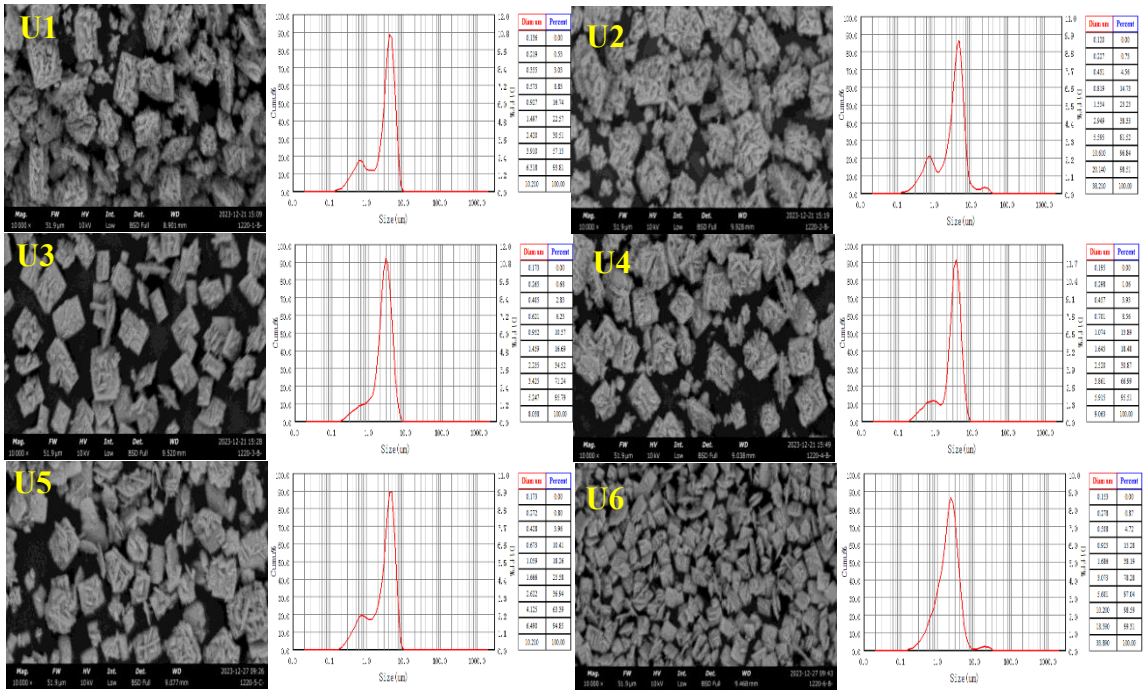

Figure 2-21 SEM and PSD of barium sulfate obtained at different feeding positions in the ultrasonic reactor: U1: (BF) feed position, U2: (BC) feed position U3: (MF) feed position, U4: (MC) feed position U5: (TF) feed position, U6: (TC) feed position; [Concentration: 0.1 mol/L, Set parameters of the ultrasonic reactor: 20V, 150 W]

Barium sulfate obtained at those feed positions applied in the ultrasonic reactor shows excellent morphology uniformity. Except for products synthesized in U1 (BF) and U2 (BC), feed positions are referred to as those mentioned above "dead zone". Barium sulfate produced at this position exhibits an aggregation state rather than the small and rectangular flakes. Barium sulfate flakes obtained at the positions (MF, MC, TF, TC) could be attributed to the coincidence that these positions are precisely correct set at the circulation point of the flow field, as shown in Figure 2-22, where the effect of mixing is perfect in the whole reactor (Virone et al., 2006, Vishwakarma and Gogate, 2017).

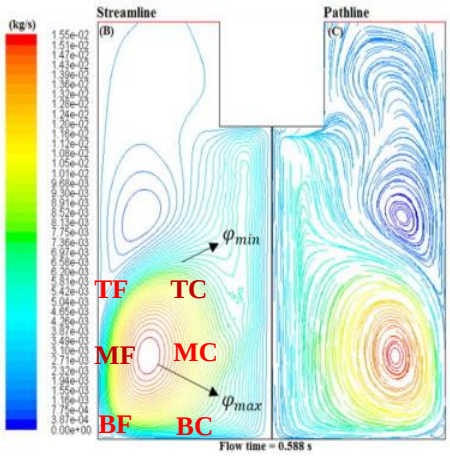

Figure 2-22 Visualization of the velocity pattern in an ultrasonic reactor (Rahimi et al., 2017), [The red marked: illustration of the feed positions in the reactor used in this study.]

According to the research of Hashemi et al. (2014), the mass flow rate defined by Eq. 2-7 could be introduced as a description of the intensive mixing in the reactor (Rahimi et al., 2017).

$$m_{net} = \Delta\varphi = \varphi_{max} - \varphi_{min} \tag{2-7}$$

Where m_{net} is the returned mass flow rate, φ_{max} and φ_{min} represents the maximum and minimum stream functions.

The research reveals that a higher mass flow rate returns at the circular zones, which may produce a higher mixing rate in this zone. Such a high mixing rate improves mixing for liquids with different densities. Besides, ultrasound can affect the yielding reduction in the induction time and improve the nucleation mechanism, which provides better control of the crystal morphology and uniform particle size distribution (Lyczko et al., 2002, Virone et al., 2006, Wohlgemuth et al., 2010, Wood et al., 2017). Due to the process intensification of ultrasonic, barium sulfate with uniform PSD of about 1.5 μm could be synthesized in such a reactor, as shown in Figure 2-23.

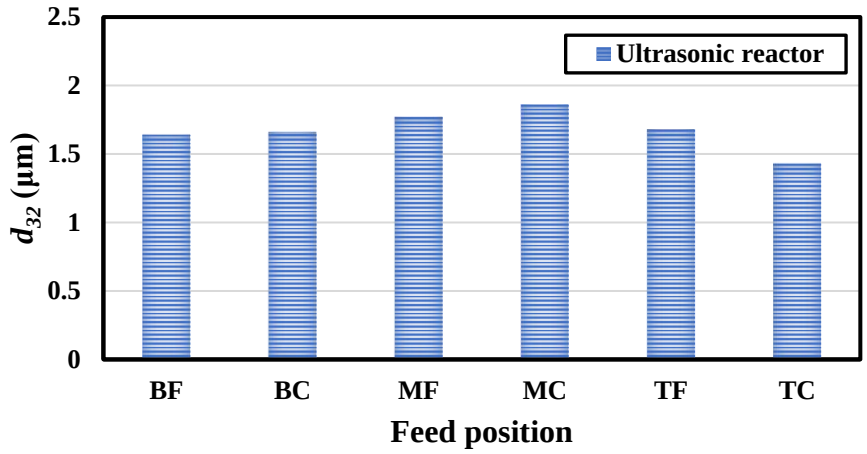

Figure 2-23 Average particle size (d_{32}) of barium sulfate obtained at different feeding positions in the ultrasonic reactor.

2.5 Synthesis of barium sulfate in the Taylor-Couette reactor

2.5.1 Experimental setup

The synthesis system comprises a Taylor-Couette reactor (TCR), a cooling circle machine, a high-low temperature circle machine, two plunger pumps, and two water baths. The inner cylinder of rotation is driven by a motor with a rotation rate in the range of 100-3000 RPM. Table 7 gives the detailed dimensions of the TCRs used in this study.

(a) (b)

Figure 2-24 TCR used in the present work: (a) TCR^1 (Gap width = 2 mm), (b) TCR^2 (Gap width = 5 mm)

Table 7

Dimensions of the Taylor-Couette reactor used in this study

Model (#)	inner cylinder R_i (mm)	outer cylinder R_o (mm)	Gap width (mm)	Length (mm)	Volume (mL)
TCR^1	33	35	2	300	128
TCR^2	30	35	5	300	306

Note: More detailed information about the applied TCR cannot be provided for confidentiality.

2.5.2 Experimental procedure

The continuous preparation of barium sulfate was conducted in TCR. The reactor was prefilled with pure water at the beginning of the experiments. A circulating oil bath was used to keep the desired reaction temperature. The aqueous solution of Na_2SO_4 and $BaCl_2$ was prepared in advance and put in the 25℃ water bath to avoid the effect of extreme temperature. During a typical synthesis, reactant solutions were simultaneously injected into the TCR by two individual plunger pumps at the desired flow rate through a PTFE tube with a diameter of 3 mm. After completing solution feeding, the white precipitates were collected and filtered by a vacuum filer, then put into a conventional oven and dried at 70℃ for 12 hours.

2.5.3 Effect of concentration

Experiments of different reactant concentrations, as shown in Tables 8 and 9, were designed to investigate the influence of concentration on the particle size and morphology of barium sulfate. According to the research of Kim et al. (2013), the axial moving velocity of the Taylor vortex was shown to decrease with a decrease in a feed flow rate, which indicates that a too fast feed flow rate could lead to a fast axial moving velocity of TVF, namely the deformation of TVF. Thus, a slow feed flow rate (20 mL/min) should be taken to maintain the desired flow pattern. The initial rotation speed of TCRs was set at the allowed lowest rotation speed, 100 rpm. All experiments were conducted at room temperature (22 ℃).

Table 8

Different reactant concentrations used for the preparation of barium sulfate in TCR[2]

No. of exp.	Rotational speed (rpm)	Total flow rate (mL/min)	No. of feed position (#)	Concentration of $BaCl_2$ (mol/L)	Concentration of Na_2SO_4 (mol/L)
C0	100	20	2,4	0.01	0.01
C1-a	100	20	2, 4	0.05	0.05
C2-a	100	20	2, 4	0.1	0.1
C3-a	100	20	2, 4	0.2	0.2
C4-a	100	20	2, 4	0.5	0.5

Table 9

Different reactant concentrations used for the preparation of barium sulfate in TCR[1]

No. of exp.	Rotational speed (rpm)	Total flow rate (mL/min)	No. of feed position (#)	Concentration of $BaCl_2$ (mol/L)	Concentration of Na_2SO_4 (mol/L)
C1-b	100	20	2, 4	0.05	0.05
C2-b	100	20	2, 4	0.1	0.1
C3-b	100	20	2, 4	0.2	0.2
C4-b	100	20	2, 4	0.5	0.5

Results and discussion

Figure 2-25 shows the SEM images (left) and the corresponding particle size distribution (PSD) diagrams (right) of barium sulfate obtained at different concentrations in TCRs. Experiments C1~4-a are conducted in TCR with a gap width of 5 mm, and C1~4-b are conducted in TCR with a gap width of 2 mm.

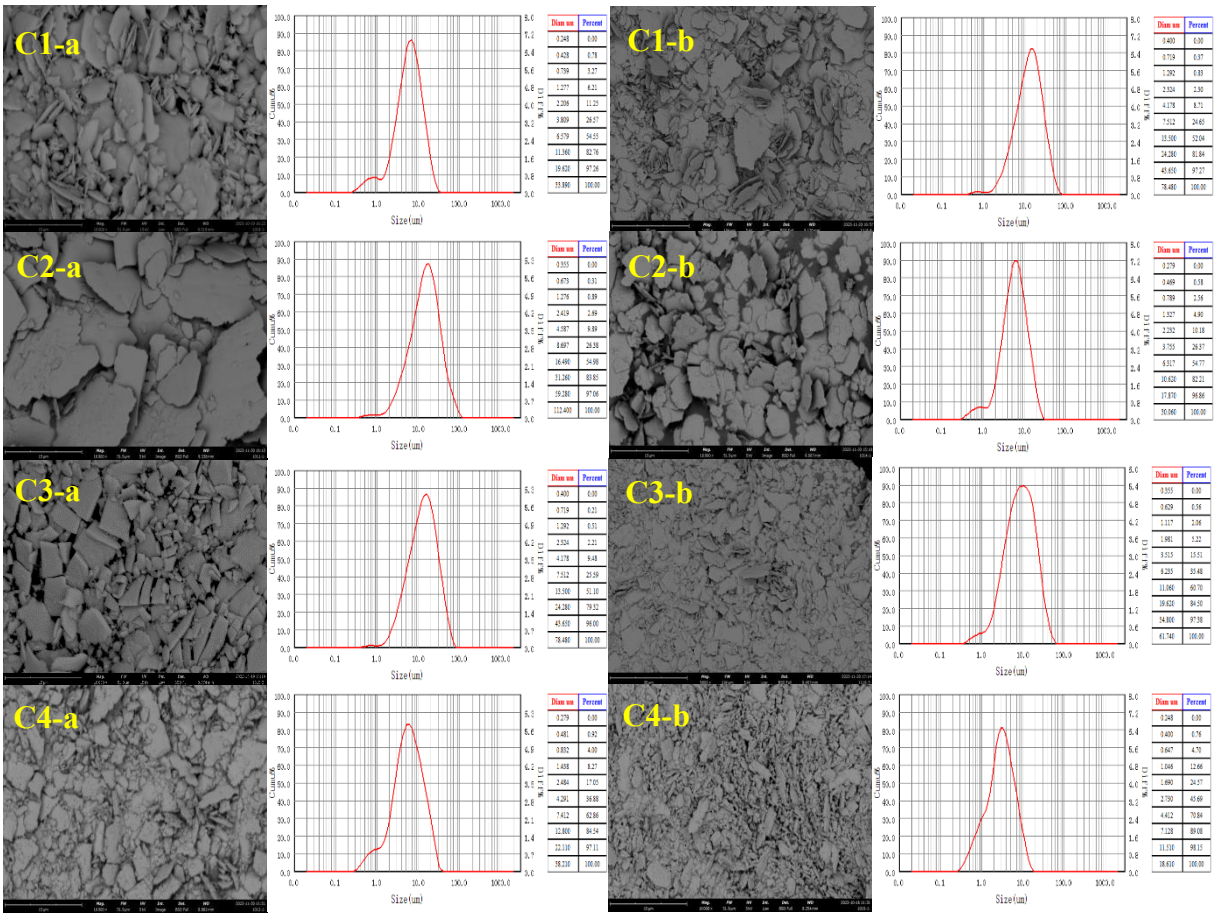

Figure 2-25 SEM and PSD of barium sulfate obtained at different reactant concentrations in TCRs: C1-a: 0.05 mol/L, C2-a: 0.1 mol/L, C3-a: 0.2 mol/L, C4-a: 0.5 mol/L; C1-b: 0.05 mol/L, C2-b: 0.1 mol/L, C3-b: 0.2 mol/L, C4-b: 0.5 mol/L; [Rotation speed: 100 rpm, Total feed flow rate: 20 mL/min]

In Figure 2-25 C1-a, flaky barium sulfate with different sizes can be observed, and the particle size is generally controlled within 3.5 μm. As the concentration increases to 0.1 mol/L, barium sulfate particles exhibit a desired flaky shape, giving an average particle size of 9.2 μm (Figure 2-25 C2-a). The average particle size of barium sulfate decreases to 8.7 μm when the concentration increases to 0.2 mol/L, and the particles become thicker (Figure 2-25 C3-a). At the highest concentration, 0.5 mol/L, barium sulfate particles become much thicker and present block-shaped with an average particle size of 3.4 μm (Figure 2-25 C4-a). Flaky barium sulfate obtained in C1-b is thinner than that obtained in C1-a and gives an average particle size of 8.6 um. As the concentration increases to 0.1 mol/L, flaky barium sulfates with an average particle size of 4.4 μm are produced (Figure 2-25 C2-b). At a concentration of 0.2 mol/L, flaky barium sulfate with an average particle size of 5.4 μm can be observed in C3-b. Then, the morphology of such flakes changes into an aggregated rice shape at the highest concentration of 0.5 mol/L. The final average particle size is located within the range of 2 μm (Figure 2-25 C4-b). It is concluded that the morphology of barium sulfate synthesized in TCRs changes from small flakes to larger flakes, then back to the small flakes, and the final thick, irregular shapes as the concentration of reactant increases.

Generally, when the concentration of the reaction system is low, the chance of collision between the particles is correspondingly low. Thus, it is difficult for the newly formed crystal nuclei to aggregate into large particles. When the concentration of the reaction system increases, the nucleation rate and the chance of collision between the particles will also increase, which is in favor of forming bigger particles (Li et al., 2023). However, as shown in Figure 2-26, increasing

the reactant concentration (0.05 mol/L-0.1mol/L) results in a smaller mean size of barium sulfate produced in TCR with a gap width of 2 mm. As the amount of precipitated $BaSO_4$ particles increases, colloidal interactions become more significant, causing an increase in fluid viscosity, possibly reaching that of a non-Newtonian colloidal suspension (Kind, 2002). In that case, namely a high-concentration suspension system, the influence of the flow pattern on the formation of the particles is limited, where such a chaotic mixing condition leads to the formation of the irregularly shaped and smaller-sized barium sulfate. However, the average particle size of barium sulfate obtained in TCR with a gap width of 5 mm increases as the concentration increases from 0.01 to 0.1 mol/L. Compared with the TCR (Gap width = 2 mm), TCR with a gap width of 5 mm has an enormous volume and a higher tolerance for the suspension system. Therefore, the formation of particles is still under the control of the flow pattern. For a reaction system with a concentration of 0.1 mol/L, a higher initial rotation speed of TCR (Gap width = 2 mm) should be set to disparate the suspension efficiently.

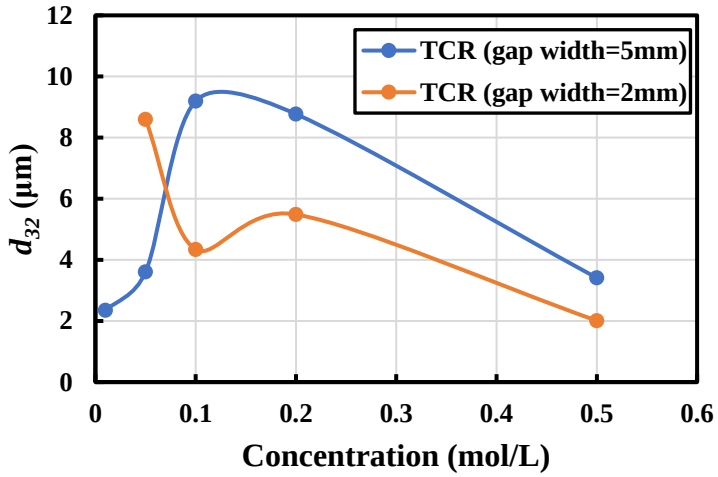

Figure 2-26 Average particle size (d_{32}) of barium sulfate obtained at different reactant concentrations in TCRs.

2.5.4 Effect of rotation speeds

In this research part, the influence of rotation speeds on the formation of barium sulfate was investigated. All experiments were conducted at room temperature (22℃). According to the results of section 2.5.3, experiments at low concentrations should be performed to examine the effect of hydrodynamics on barium sulfate's particle size and morphology. Therefore, 0.1mol/L reactant solutions were prepared. Given that the mixing at 100 rpm in TCR (gap width = 2 mm) was insufficient, therefore its initial rotation speed was set at 200 rpm to achieve better dispersion. The main operating parameters of experiments are listed in Tables 10 and 11.

Table 10

Different rotation speeds used for the preparation of barium sulfate in TCR with a gap width of 5 mm

No. of exp.	Rotational speed (rpm)	Total flow rate (mL/min)	No. of feed position (#)	Concentration of $BaCl_2$ (mol/L)	Concentration of Na_2SO_4 (mol/L)
RS1-a	100	20	2, 4	0.1	0.1
RS2-a	200	20	2, 4	0.1	0.1
RS3-a	400	20	2, 4	0.1	0.1
RS4-a	800	20	2, 4	0.1	0.1
RS5-a	1000	20	2, 4	0.1	0.1

Table 11

Different rotation speeds used for the preparation of barium sulfate in TCR with a gap width of 2 mm

No. of exp.	Rotational speed (rpm)	Total flow rate (mL/min)	No. of feed position (#)	Concentration of $BaCl_2$ (mol/L)	Concentration of Na_2SO_4 (mol/L)
RS2-b	200	20	2, 4	0.1	0.1
RS3-b	400	20	2, 4	0.1	0.1
RS4-b	800	20	2, 4	0.1	0.1
RS5-b	1000	20	2, 4	0.1	0.1

Results and discussion

Figure 2-27 shows SEM images (left) and the corresponding particle size distribution (PSD) diagrams (right) of barium sulfate obtained at different rotation speeds in TCRs. Experiments RS1~5-a were carried out in TCR with a gap width of 5 mm, and RS2~5-b were carried out in TCR with a gap width of 2 mm. In Figure 2-27 RS1-a, a desired flaky barium sulfate with an average particle size of 9.2 μm can be obtained. As the rotation speed increases to 200 rpm, such barium sulfate flakes can still be produced but with an occurrence of small aggregated spherical crystals, giving an average particle size of 8.2 μm (Figure 2-27 RS2-a). As the rotation speed increases from 400 rpm to 800 rpm and then 1000 rpm, the morphology of the particles is similar, namely aggregated clusters. The corresponding average particle size decreases from

7.4 μm (Figure 2-27 RS3-a) to 5.4 μm (Figure 2-27 RS4-a) and 4 μm (Figure 2-27 RS5-a).

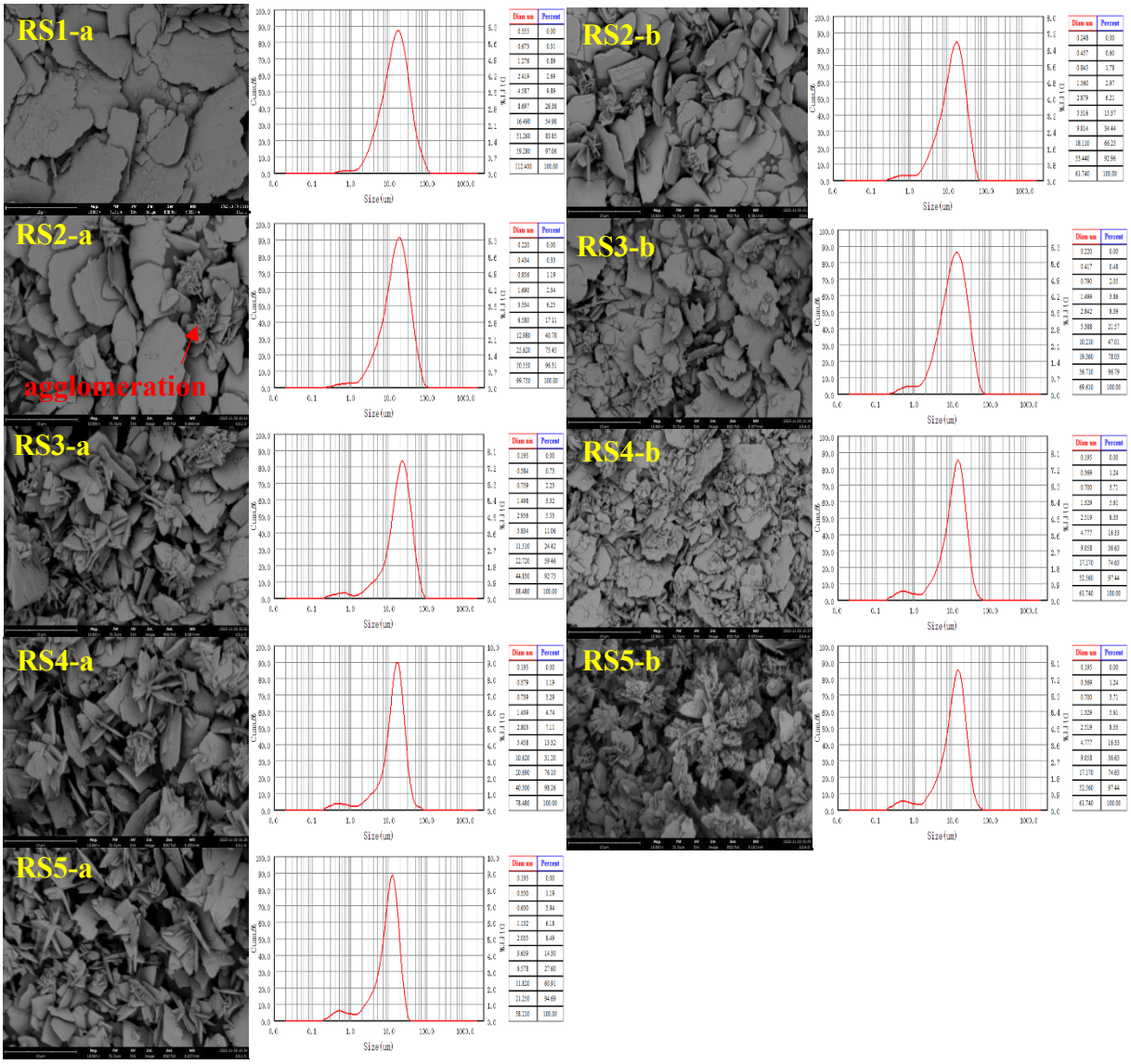

Figure 2-27 SEM and PSD of barium sulfate obtained at different rotation speeds in TCRs: RS1-a: 100 rpm, RS2-a: 200 rpm, RS3-a: 400 rpm, RS4-a: 800 rpm, RS5-a: 1000 rpm; RS2-b: 200 rpm, RS3-b: 400 rpm, RS4-b:800 rpm, RS5-b: 1000 rpm; [Concentration: 0.1 mol/L, Total feed flow rate: 20 mL/min].

In Figure 2-27 RS2-b, barium sulfate with a clean surface can be observed, giving an average particle size of 6.8 μm, but some aggregated clusters of barium sulfate can also be observed. As the rotation speed increases to 400 rpm, more aggregated clusters of barium sulfate appear, and

the surface of the particles is attached to some tiny crystals. The average particle size decreases to 5.7 μm (Figure 2-27 RS3-b). When the rotation speed reaches 800 rpm, the surface of the particles is covered with many aggregated crystals, giving an average particle size of 4.5 μm (Figure 2-27 RS4-b). At the highest rotation speed, 1000 rpm, the formed flaky barium sulfates are wholly covered with clusters, and the average particle size is 4.5 μm (Figure 2-27 RS5-b). Barium sulfate particles obtained in each TCR show a morphology change from irregular flakes to clusters as the rotation speed increases, indicating that the flow patterns greatly influence barium sulfate's morphology and particle size. As shown in Figure 2-27, the marked area of Figure 2-27 RS2-a exhibits an agglomeration of crystals, and such a phenomenon can also be observed in other SEM images, which can be deduced from the comparison of the time scale. The characteristic induction time for the formation of nuclei is extremely short, giving a value of 1×10^{-3} s, and the nucleation rate is about $\sim1\times10^{13}$ nucleus/m^{2}s (Liu et al., 2020). Generally, micromixing time (t_M) can be evaluated according to Eq. 2-8 (Racina and Kind, 2006):

$$t_M = \sqrt{\frac{\nu}{\varepsilon}} \tag{2-8}$$

Where ν is the kinematic viscosity of the fluid (1×10^{-6} m^{2}s^{-1}), ε is the amount of energy dissipated in the flow, which can be calculated from the torque of the applied reactor (T), as expressed in Eq. 2-9 (Racina and Kind, 2006). The torque (τ) can be entirely described with Eq. 2-10 according to the theory of dimensional analysis (Racina and Kind, 2006).

$$\varepsilon = \frac{P}{\rho V} = \frac{T\omega}{\rho V} \tag{2-9}$$

$$\tau = G\rho v^2 H \tag{2-10}$$

Where ω is the cylinder angular speed (rad s^{-1}), ρ is fluid density (1×10^3 kg/m^3), V is the volume

of the reactor (m^3), $V_{TCR^1} = 1.28 \times 10^{-4}\ m^3, V_{TCR^2} = 3.06 \times 10^{-4}\ m^3$, ν is the kinematic viscosity of the fluid ($1 \times 10^{-6}\ m^2 s^{-1}$) and H is cylinder length (both 0.3 m). G is the dimensionless number used to analyze the torque power consumption in Taylor-Couette reactor yields. Herein, a general form of G is applied in this calculation, described as Eq. 2-11 (Lathrop et al., 1992, Lewis and Swinney, 1999):

$$G \sim Re^{\alpha} \tag{2-11}$$

The calculation of Re is based on the previous Eq. 2-2 in section 2.1.3. Generally, the value α can be determined by experimental investigations and is found to be correlated with the ratio of the cylinder radius ($\eta = R_i/R_o$), which means that the value α is probably applicable for the particular case, such as when $\eta = 0.5$ $\alpha = 1$ (Stuart, 1958), when $\eta = 0.76$ $\alpha = 1.445$ (Racina and Kind, 2006). However, the value α is approximately 1.36 given by Donnelly and Simon (1960), was found to be almost independent of the gap width, suggesting suitable over quite a wide range of conditions. Consequently, $\alpha = 1.36$ is applied in this calculation.

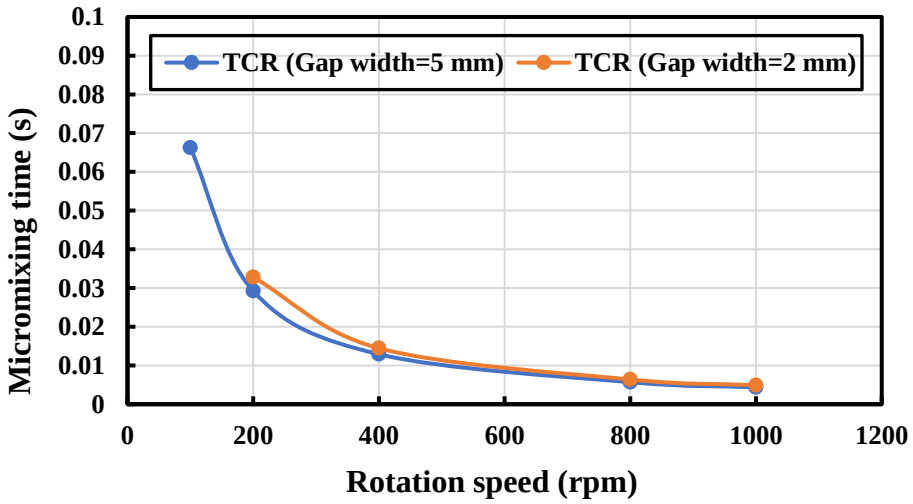

Figure 2-28 Micromixing time at different rotation speeds in TCRs.

As shown in Figure 2-28, micromixing times range between 5×10^{-3} s and 4×10^{-2} s, which is longer than the nucleation time (1×10^{-3} s), indicating that the flow dynamic in TCR has almost no influence on the nature of crystallization kinetics of barium sulfate, but can significantly affect the growth and aggregation of crystals.

Figure 2-29 shows the change in average particle size at different rotational speeds in TCRs. An increased rotation speed reduces the average particle size, which can be attributed to a stronger micromixing efficiency caused by a higher rotation speed. Marchisio et al. (2001) investigated barium sulfate precipitation in a Taylor-Couette reactor under the fully turbulent flow. The results showed that the average particle size decreased as the rotation speed increased due to the enhanced micromixing efficiency.

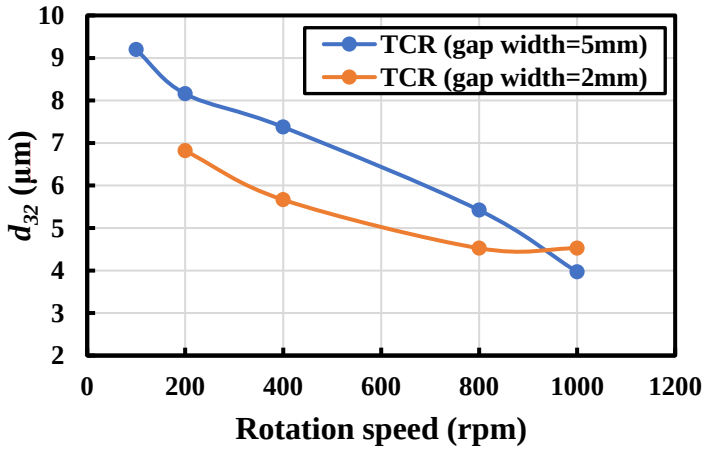

Figure 2-29 Average particle size (d_{32}) of barium sulfate obtained at different rotation speeds in TCRs.

2.5.5 Effect of feed flow rate

Residence time is a significant aspect of synthesis in reactors. In this part, residence time was determined by the feeding flow rate. Therefore, experiments with different feed flow rates were carried out at room temperature (22°C) to examine the influence of residence time. The detailed operation parameters are listed in Table 12.

Table 12

Different flow rates used for the preparation of barium sulfate in TCRs

No. of exp.	Rotational speed (rpm)	Total feed flow rate (mL/min)	No. of feed position (#)	Concentration of $BaCl_2$ (mol/L)	Concentration of Na_2SO_4 (mol/L)
FR1-a/b	100	10	2, 4	0.1	0.1
FR2-a/b	100	20	2, 4	0.1	0.1
FR3-a/b	100	60	2, 4	0.1	0.1
FR4-a/b	100	100	2, 4	0.1	0.1
FR5-a	100	200	2,4	0.1	0.1
FR6-a	100	300	2, 4	0.1	0.1

Results and discussion

Figure 2-30 shows the SEM images (left) and the corresponding particle size distribution (PSD) diagrams (right) of barium sulfate synthesized at different feed flow rates in TCR (Gap width = 5mm).

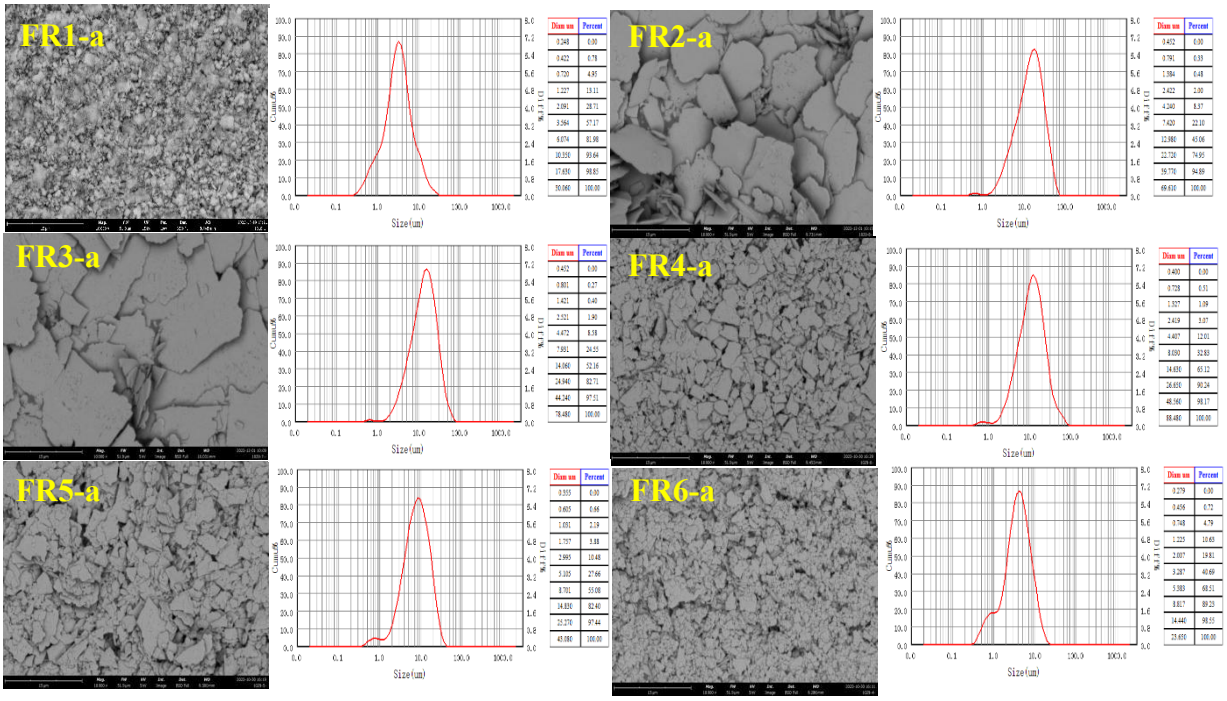

Figure 2-30 SEM and PSD of barium sulfate obtained at different feed flow rate in TCR with a gap width of 5 mm: FR1-a: total 10 mL/min, FR2-a: total 20 mL/min, FR3-a: total 60 mL/min; FR4-a: total 100 mL/min, FR5-a: total 200 mL/min, FR6-a: total 300 mL/min; [Rotation speed: 100 rpm, Concentration: 0.1 mol/L]

At the slowest feeding mode applied in TCR (Gap width = 5mm), the final barium sulfate presents a crumb shape; these highly tiny particles' particle size is within 2 μm (Figure 2-30 FR1-a). As the total feed flow rate increases to 20 and 60 mL/min (Figure 2-30 FR2-a, FR3-a), flaky barium sulfate with an average particle size of about 9 μm can be produced. After that, the flow rate increased from 100 mL/min (Figure 2-30 FR4-a) to 200 mL/min (Figure 2-30 FR5-a), then the final 300 mL/min (Figure 2-30 FR6-a), decreasing the average particle size from 7.6 μm to 5.3 μm, the final 2.6 μm, but the morphology of the products consistently exhibits a plate-like shape. In summary, the change in morphology of barium sulfate synthesized in TCR (Gap width = 5mm) with different feed flow rates is noticeable, from the

crumb at the slowest feed flow rate (total 10 mL/min) to large flakes, then small flakes and the final smaller flakes at the fastest feed flow rate (total 300 mL/min).

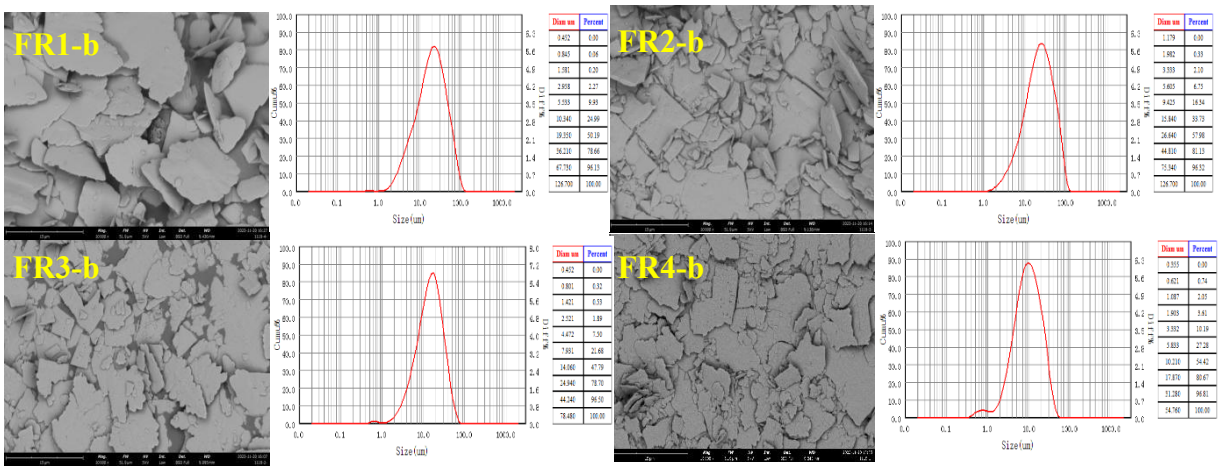

Figure 2-31 SEM and PSD of barium sulfate obtained at different feed flow rates in TCR with a gap of 2 mm: FR1-b: total 10 mL/min, FR2-b: total 20 mL/min, FR3-b: total 60 mL/min, FR4-b: total 100 mL/min; [Rotation speed: 100 rpm, Concentration: 0.1 mol/L]

Figure 2-31 shows the SEM images (left) and the corresponding particle size distribution (PSD) diagrams (right) of barium sulfate synthesized at different feed flow rates in TCR with a gap width of 2 mm. Unlike the crumb-shaped products obtained in experiment FR1-a, at the slowest feed flow rate, barium sulfate with a desired flaky shape is produced in experiment FR1-b, and the average particle size of such products reaches 12.2 μm. As the feed flow rate increases to 60 mL/min, the average particle size increases to 14.7 μm (Figure 2-30 FR2-b), but more small flaky particles are also produced. After that, an increase in the feed flow rate causes a corresponding decrease in the average particle size of the flaky barium sulfate, 10 μm in (Figure 2-30 FR3-b) and 6 μm in (Figure 2-30 FR4-b).

As shown in Figure 2-32, the particle size decreases as the flow rate increases, except for the slowest feed flow rate (10 mL/min), which agrees with the conclusion of Aljishi et al. (2013).

At the slowest feeding mode, the formed $BaSO_4$ suspension in TCR (Gap width =5mm) cannot outflow in time due to the slow feeding speed, which leads to a transient high concentration of the suspension. In that case, the chance of colliding of the formed large particles increased considerably due to a long mixing time, resulting in a smaller particle size.

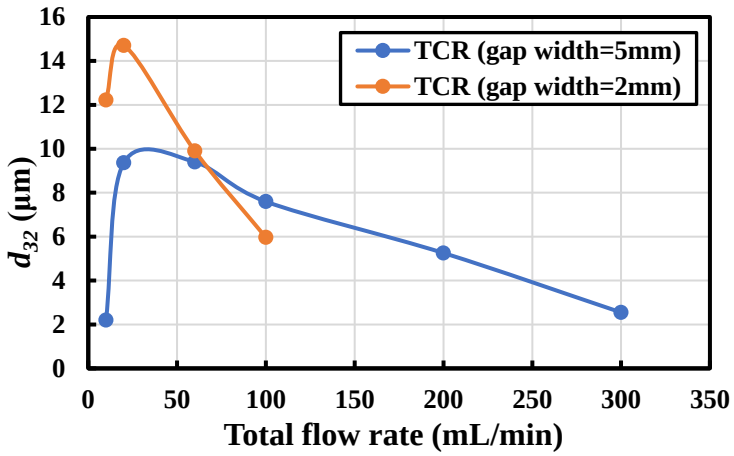

Figure 2-32 Average particle size (d_{32}) of barium sulfate obtained at different flow rates in TCRs.

Table 13 summarizes the different feed flow rates and their corresponding residence times in the TCRs used in experiments. An interesting phenomenon is that the average particle size of the products obtained at the slowest feeding mode in TCR with a gap of 5 mm is smaller than that obtained at other feeding modes. In contrast, barium sulfate with a relatively large particle size can be produced at the slowest feeding mode in TCR with a gap width of 2mm. That could be attributed to the difference in volume processing capacity in different reactors. At the same feeding flow rate, the residence time of reactants staying in TCR with a gap of 2 mm is far shorter than that staying in TCR with a gap width of 5 mm, as listed in Table 13. Thus, the transient concentration of barium sulfate suspension is relatively lower, which has almost no effect on the reaction.

Table 13

Residence time and the corresponding particle size in TCRs

Model:	TCR (gap width = 2 mm)		TCR (gap width = 5 mm)	
Total flow rate (mL/min)	Residence time (min)	Particle size (μm)	Residence time (min)	Particle size (μm)
10	12.8	12.22	30.6	2.2
20	6.4	14.71	15.3	9.36
60	2.1	9.9	5.1	9.4
100	1.28	5.96	3.06	7.6
200	NA	NA	1.53	5.26
300	NA	NA	1.02	2.55

2.5.6 Effect of reaction temperature

It is well known that reaction temperature greatly influences the rate of chemical reactions. Generally, the rate of reactions increases as the temperature increases for most of the chemical reactions. Five groups of experiments at different temperatures were conducted in TCR with a gap width of 5 mm to investigate the effect of the temperature on the preparation of barium sulfate. The concentration of the $BaCl_2$ and Na_2SO_4 solutions were both 0.1 mol/L, and other main operating parameters are listed in Table 14.

Table 14

Different reaction temperatures applied in the preparation of barium sulfate in TCR with a gap width of 5mm

No. of exp.	Rotational speed (rpm)	Total flow rate (mL/min)	No. of feed position (#)	Reactants concentration (mol/L)	Reaction temperature (℃)
RT-1	100	100	2, 4	Both 0.1	0
RT-2	100	100	2, 4	Both 0.1	20
RT-3	100	100	2, 4	Both 0.1	40
RT-4	100	100	2, 4	Both 0.1	80
RT-5	100	100	2, 4	Both 0.1	90

Results and discussion

Figure 2-33 shows SEM images (left) and the corresponding particle size distribution (PSD) diagrams (right) of $BaSO_4$ synthesized at different temperatures in TCR with a gap width of 5 mm. At the lowest reaction temperature of 0 ℃, the products present an irregular shape, giving a size of 5.9 μm, and a crack of the crystal growth can be observed, as shown in the marked red area in RT-1. A flaky barium sulfate can be produced at room temperature, 20 ℃, but there are some fine holes on the surface of the particles, as shown in the marked area in Figure 2-33 RT-2. As the temperature increases to 40℃, such fine holes become less, giving an average particle size of 3.3 μm (Figure 2-33 RT-3). When the temperature reaches 80℃, those fine holes exist

no more. The flaky barium sulfate's surface looks smooth, with an average particle size of 3 μm (Figure 2-33 RT-4). At the highest temperature, 90℃, the flaky barium sulfate changes into smaller and thicker flakes, giving an average particle size of 5.6 μm (Figure 2-33 RT-5).

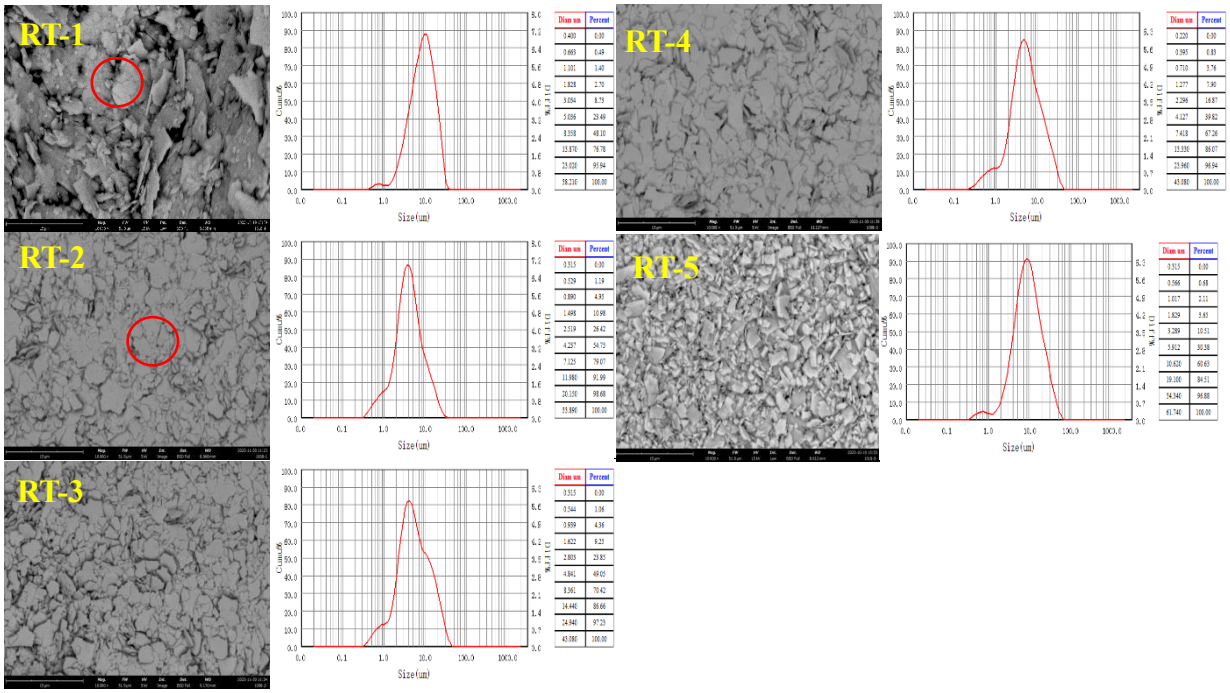

Figure 2-33 SEM and PSD of barium sulfate obtained at different reaction temperatures in TCR with a gap width of 5mm: RT-1: 0℃, RT-2: 20 ℃, RT-3: 40℃, RT-4: 80℃, RT-5: 90℃; [Concentration: 0.1 mol/L, Rotation speed: 100 rpm, Total feed flow rate: 100mL/min]

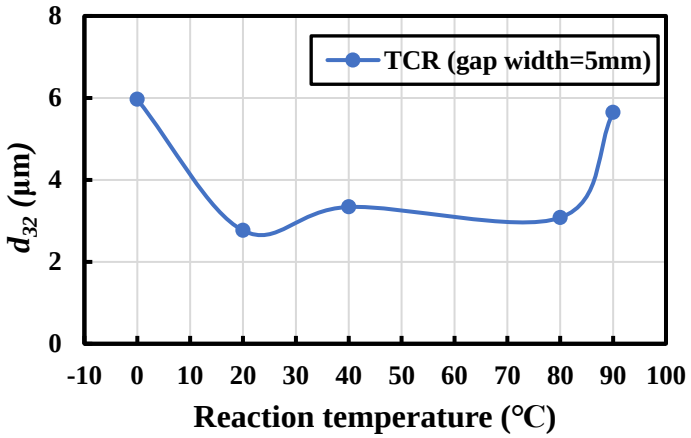

Figure 2-34 Average particle size (d_{32}) of barium sulfate obtained at different reaction temperatures in TCR with a gap width of 5mm.

Figure 2-34 exhibits the change in average particle size at different reaction temperatures in the TCR (Gap width = 5 mm). Except for the experimental conditions at the lowest temperature (0°C) and the highest temperature (90°C), the particle size keeps around 3 μm at the temperature range from 20°C to 80°C, suggesting such a temperature range might have no influence on the formation of barium sulfate. To some extent, it is acceptable to put barium sulfate precipitation at room temperature for less energy consumption. This behavior of the average particle size shows excellent consistency with the research results of Li et al. (2023). The particle size of products obtained in a relatively higher or lower reaction temperature is larger than that obtained in the ordinary reaction temperature.

2.5.7 Effect of feed position

For barium sulfate precipitated from $BaCl_2$ and Na_2SO_4 solutions in a T-mixer, the whole precipitation process time is speedy, about 1 ms; after that, aggregation dominates the changes in the particle size distribution ending within one second (Schwarzer and Peukert, 2004). Since the precipitation of $BaSO_4$ is very fast, different feeding positions, as shown in Figure 2-35, were used to adjust the contact time scale to check the influence of the feed position (FP) on the morphology and the size of barium sulfate. The experiments were conducted soon after the investigation of the effect of reaction temperature, consequently, the reaction temperature in this experiment was relatively higher (set at 60°C). Table 15 shows the experimental conditions used in this study.

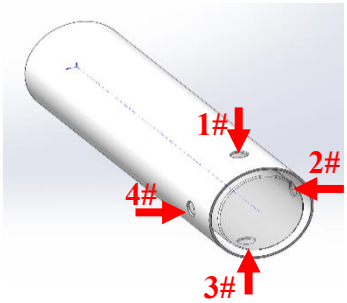

Figure 2-35 Feed position used in TCR with a gap width of 5 mm.

Table 15

Different feed positions used for the preparation of barium sulfate in TCR with a gap width of 5 mm

No. of exp.	Rotational speed (rpm)	Total flow rate (mL/min)	No. of feed position (#)	Concentration of $BaCl_2$ (mol/L)	Concentration of Na_2SO_4 (mol/L)
FP-1	100	30	1, 1	0.1	0.1
FP-2	100	30	1, 2	0.1	0.1
FP-3	100	20	1, 3	0.1	0.1
RS1-a	100	20	2, 4	0.1	0.1

[Note: "RS1-a" here is as a control group for experiment "FP-3"]

Results and discussion

Figure 2-36 shows SEM images (left) and the corresponding particle size distribution (PSD) diagrams (right) of $BaSO_4$ synthesized at different feed positions in TCR with a gap width of 5 mm. Figure 2-37 exhibits the change in the average particle size at different feeding locations.

When two feed tubes are placed together (1,1#), floc barium sulfate is produced (Figure 2-37 FP-1), and probably during the reaction, some floc aggregates into big-sized agglomerates, resulting in a bimodal distribution. The actual particle size of such products is about 3 μm, rather than those over-sized. The floc in FP-1 could be attributed to that feeding mode leads to high local supersaturations, resulting in a typical characteristic of the bimodal distributions (Wong et al., 2003). When the feed tubes are placed at 90° crossed (1,2#), serrated barium sulfate with an average particle size of 9.6 μm is observed (Figure 2-37 FP-2).

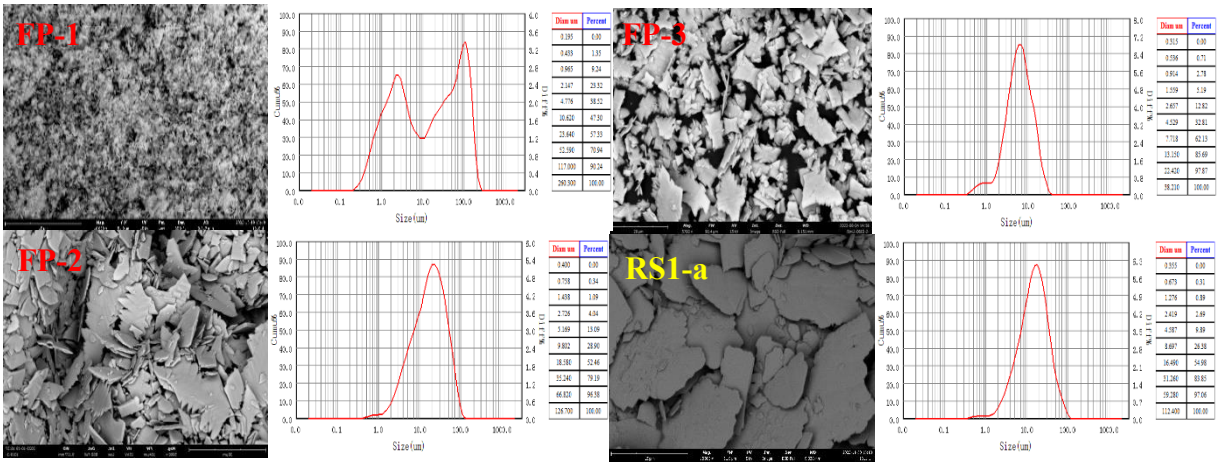

Figure 2-36 SEM and PSD in different feeding position in TCR with a gap of 5 mm:
FP-1: feed pipe set at top together, FP-2: feed pipe set at 90° crossed, (Total feed flow rate: 30 mL/min), FP-3: feed pipe set at 180° symmetrical (up-down), flow rate: 20 mL/min
[Concentration: 0.1 mol/L, Rotation speed: 100 rpm, Reaction temperature: 60°C]

The products obtained at the feed tubes set at 180° symmetrical (1,3#) present the same serrated but with a smaller particle size of 4.2 μm (Figure 2-37 FP-3). According to the results in section 2.5.6, RS1-a could be considered as a control group for FP-3. Technically, the average particle size of barium sulfate obtained in Exp. FP-3 should be close to that obtained in RS1-a (180° horizontal 2,4#), but actually, the size of RS1-a was nearly twice that of FP-3. It could be

attributed to the resistance formed by the rotating fluid in the chamber obstructing the normal reactant solution flow. During the experiment, when the reactant solution transported from the top (1#) was finished, the other reactant solution transported from the bottom (3#) still had remaining. In such a case, the reaction condition was always undersaturated, leading to a smaller particle size.

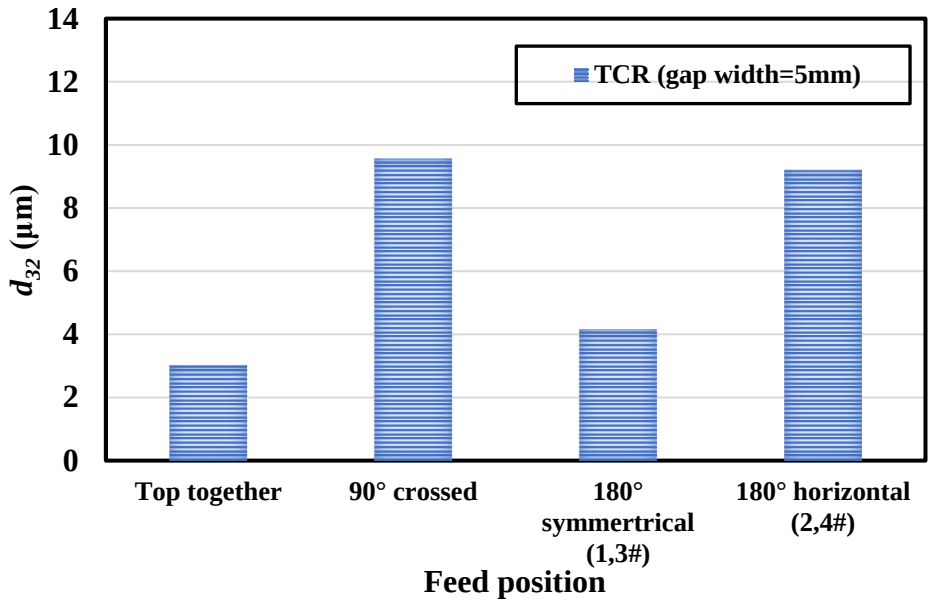

Figure 2-37 Average particle size (d_{32}) of barium sulfate obtained at different feeding positions in TCR with a gap width of 5 mm.

2.5.8 Summary

This part demonstrates a systematic experimental investigation of preparing flaky barium sulfate in TCRs. Firstly, the effect of concentrations of reactant solutions on the morphology and particle size was studied by changing the molar ratio. The results revealed that concentration is linearly related to particle size, as reported in some literature; instead, when the concentration reaches a specific balanced value (0.1 mol/L in this research), this linear relationship could be established. Secondly, the effect of hydrodynamics inside the TCRs on the morphology and particle size was studied by changing the rotation speed, which exhibited TCR's great micro mixing capacity due to the uniformity in the fluid dynamic conditions. Then, the feed flow rate was investigated to estimate the possible productivity. As an essential parameter for describing the energy consumption, the required reaction temperature was also studied, which provides a valuable design principle of experiments for the following large-scale synthesis. Last, the feed position was determined according to the results of section 2.5.7.

It is necessary to notice that the conclusion of these investigated factors could only be established for the current reaction condition because the properties of precipitated particles are shaped by the interaction of several steps involved, such as mixing, nucleation, growth, self-assembled and arbitrary aggregation. Due to their kinetics, it is difficult to study each step individually because these steps do not occur sequentially. Instead, some steps could occur simultaneously, resulting in competition between the corresponding subprocesses (Aljishi et al., 2013).

2.6 Comparison of used reactors in application to synthesizing barium sulfate

Four groups of experiments were conducted to find an ideal process for synthesizing flaky barium sulfate. The representative characteristics of barium sulfate obtained in each kind of reactor are exhibited in Table 16.

Table 16

Characteristics of barium sulfate obtained in different reactors used in this study

Reactor type	HSSM	STR	USR	TCR
Typical SEM in this investigation	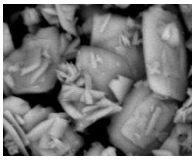	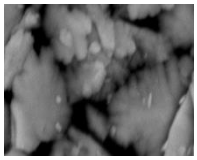	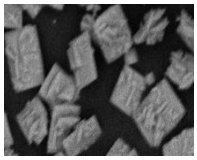	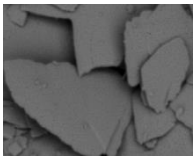
Particle size	3.4μm	9.7μm	1.9μm	9.2μm
Typical SEM in literature review	NA	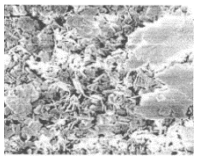	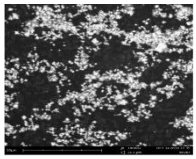	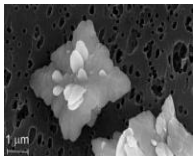
Particle size	NA	About 10μm	1.1μm	3.3μm

[Typical SEM in the literature review (from left to right): Wong et al. (2003), Pohl et al. (2012), Judat et al. (2004)]

From Table 16, the surface of barium sulfate obtained in the robust dispersion conditions generated by the high-speed shear mixer or ultrasonic reactor is often attached with tiny particles and thicker than that obtained in gentler reaction conditions generated by stirred tank reactor and Taylor-Couette reactor, which suggests that flaky barium sulfate should be synthesized in a gentle mixing condition. Given that the growth of the crystals seems to be inhibited in the stirred tank reactor, the Taylor-Couette reactor could be considered an ideal option for the next large-scale experiments.

2.7 Recapitulation and conclusion

In this chapter, four types of chemical reactors were studied to seek an optimal solution to synthesize flaky barium sulfate. Each possible operating parameter was studied in detail in these parts to determine their effect on preparing flaky barium sulfate. In most experimental investigations, flaky barium sulfate can always be produced in a Taylor-Couette reactor due to its more uniform flow field, suggesting that the Taylor-Couette reactor is the best option for preparing flaky barium sulfate. As to the high-speed shear mixer, flaky barium sulfate can be obtained at a rotation speed within a range of 6000-10000 rpm, yet the particle size is relatively smaller, which could be attributed to the more potent shear force and mixing in it. The change in the morphology and particle size of barium sulfate synthesized in the ultrasonic reactor is similar to that obtained in the high-speed shear mixer. The mixing conditions generated in the ultrasonic reactor are also pretty violent, resulting in a smaller particle size. Finally, the stirred tank reactor is not recommended to be used to prepare flaky barium sulfate due to its nonuniform flow field, which has an evident inhibition effect on the growth of particles.

At the current stage, this work aims to explore an applicable method within a limited time to produce the required flaky barium sulfate, thus most of the experiments and the measurement of their particle size in this chapter were conducted only once. To ensure the reliability of the measured average particle size (d_{32}), several samples were picked out randomly to do the second analysis. For example, the value of "*D10*, *D50*, *D90*" of C2-b in the first analysis were: 2.52μm, 6.334μm, 14.296μm and the value of "*D10*, *D50*, *D90*" of C2-b in the second analysis were: 2.551μm, 6.204μm, 13.982μm. The deviation of *D50*, *D10* and *D90* were: 2.1% (⩽6%), 1.2%

and 2.2% (⩽10%), which was admissible according to the standard of ISO 13320-2009. The value of "*D10*, *D50*, *D90*" of RS2-b in the first analysis were: 3.945μm, 13.533μm, 30.235μm and the value of "*D10*, *D50*, *D90*" of RS2-b in the second analysis were: 4.096μm, 13.757μm, 32.624μm. The deviation of *D50*, *D10* and *D90* were: 1.6% (⩽6%), 3.7% and 7.3% (⩽10%), which was also acceptable according to the above-mentioned standard, indicating that the applied method for determining the average particle size in this work was reasonable.

Note: *D10*, Cumulative distribution of particles as 10% of particle size,

D50, Cumulative distribution of particles as 50% of particle size,

D90, Cumulative distribution of particles as 90% of particle size.

Chapter 3. Large-scale continuous synthesis of flaky barium sulfate in Taylor-Couette reactor

3.1 Introduction

In the previous chapter, several chemical reactors were applied to the small-scale synthesis of flaky barium sulfate. Although uniform particle size distribution and regularly shaped barium sulfate could be obtained in the high-speed shear mixer and the ultrasonic reactor, the industrial application of this equipment could be complex due to high energy consumption and probably unstable reaction yield in large-scale production. In a high-speed shear mixer, the process technology often operates in turbulent flow conditions, where the flow is very complex (Vashisth et al., 2021). More research based on the configuration of high-speed shear mixers, the droplet breakage mechanism, and their correlation system should be studied further for the process design and scale-up. The nonuniform flow field generated in the stirred tank reactor is also not suitable for the growth of barium sulfate particles. As discussed, the three above-mentioned reactors were not recommended to be used for the large-scale production of flaky barium sulfate. However, the desired flaky barium sulfate with an acceptable particle size could be obtained in the Taylor-Couette reactor, thus such a reactor seemed to be a good option for the following large-scale experimental investigation. In this part, experiments were conducted by modifying several essential parameters, such as rotation speed, feed flow rate, and reaction temperature, to check the possibility of large-scale continuous synthesis of flaky barium sulfate with satisfactory morphology and uniform particle size distribution in the Taylor-Couette reactor with a gap width of 13 mm.

3.2 Experimental setup

The continuous synthesis system (Figure 3-1) applied to prepare barium sulfate is comprised of the TCR with a gap width of 13 mm, a cooling-circle system for mechanical seal, a temperature-assisted circulating machine, and two individual metering peristaltic pumps. The inner cylinder rotation is driven by a motor that provides a rotation rate of 10-300 RPM. Reactant materials are prepared into aqueous solutions and stored in plastic buckets with a volume of 25 L.

Figure 3-1 TCR^3 (Gap width = 13 mm)

Table 17

Dimensions of the TCR^3 (Gap width = 13 mm)

Model	inner cylinder R_i (mm)	outer cylinder R_o (mm)	Gap (mm)	Length (mm)	Volume (L)
TCR^3	111	124	13	1000	14

3.3 Experimental procedure

Barium sulfate was continuously produced in the TCR with a gap width of 13 mm by adjusting the operation process parameters. A circulating oil bath was used to maintain the desired reaction temperature. At the beginning of the experiment, the reactor was prefilled with total pure water, and the inner cylinder rotated at the set speed. Then, $BaCl_2$ and Na_2SO_4 solutions were simultaneously injected into the reactor chamber through a Polyurethane (PU) tube with a diameter of 8 mm by two individual metering peristaltic pumps. After completing solution feeding, the resulting products were filtered by a vacuum filer to collect the white precipitates. Then, the filtered products were put into a conventional oven and dried at 70℃ for 12 hours. Table 18 shows the experimental records in this study.

Table 18

Records of the large-scale experiments (LSE) conducted to prepare barium sulfate

No. of exp.	Rotational speed (rpm)	Total feed flow rate (mL/min)	Feeding time (min)	No. of feed position (#)	Reactants concentration (mol/L)	Reaction temperature (℃)
LSE-1	20	900	55	-	Both 0.1	40
LSE-2	20	900	55	-	Both 0.1	55
LSE-3	30	2000	25	-	Both 0.1	30
LSE-4	30	800	65	-	Both 0.1	25
LSE-5	30	800	125	-	Both 0.1	25

3.4 Results and Discussions

3.4.1 Characteristics of barium sulfate obtained in the large-scale experiments

Figures 3-2 and 3-3 exhibit the SEM images (up) and the change in average particle size (down) of barium sulfate prepared in the large-scale experiments 1-4 (LSE1-4).

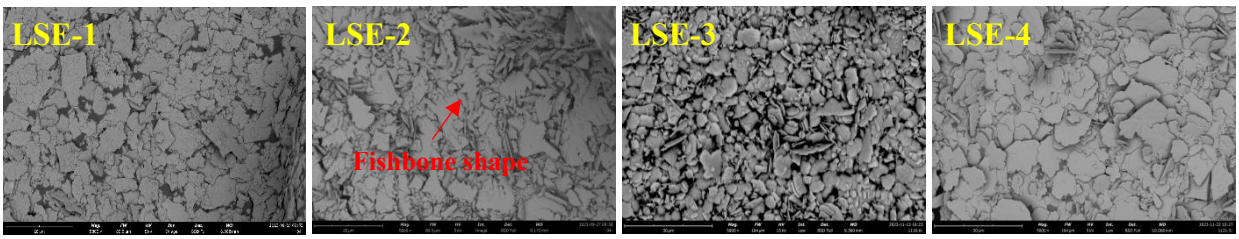

sample at 30 min | sample at 30 min | sample at 15 min | sample at 35 min

Figure 3-2 SEM of samples obtained at different times in each large-scale experiment:
LSE-1: Rotation speed = 20 rpm, Total feed flow rate: 900 mL/min (×55 min), 40℃;
LSE-2: Rotation speed = 20 rpm, Total feed flow rate: 900 mL/min (×55 min), 55℃;
LSE-3: Rotation speed = 30 rpm, Total feed flow rate: 2000 mL/min (×25 min), 30℃;
LSE-4: Rotation speed = 30 rpm, Total feed flow rate: 800 mL/min (×65 min), 25℃;
[Concentration: 0.1 mol/L, TCR (Gap width = 13 mm)]

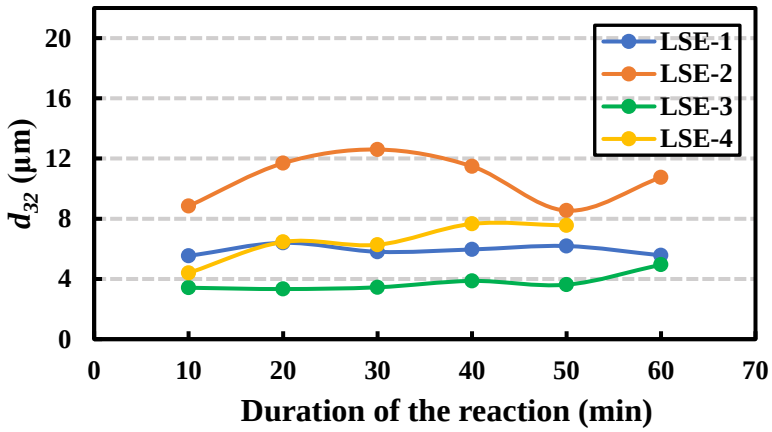

Figure 3-3 Average particle size (d_{32}) of barium sulfate obtained in each large-scale experiment.

In LSE-1, flaky barium sulfate with an average particle size of 5.9 μm was successfully prepared, proving the feasibility of TCR applied in preparing flaky barium sulfate. Then, LSE-2 was conducted at a higher reaction temperature to examine the influence of the temperature on the preparation of barium sulfate. Products with a fishbone-like shape were observed in the SEM, which indicated that flaky barium sulfate should be prepared in a milder condition. Therefore, LSE-3, with a faster feed flow rate, was conducted at a mild condition of 30 ℃ to achieve a higher yield. Although flaky products could be prepared, the particle size was unsatisfactory, giving a value of only 3.8 μm. In LSE-4, the total feed flow rate was adjusted to 800 mL/min, in which case flaky barium sulfate with an average particle size of 6.4 μm was produced.

Based on the results of the previous LSEs, an ideal experimental condition for preparing the flaky barium sulfate should involve 30 (rpm) of the rotation speed, 800-900 mL/min of the total feed flow rate, and a mild reaction temperature (at 25℃ representatively). Therefore, LSE-5 was conducted to examine the reasonability of these operation process parameters. Figures 3-4 and 3-5 give the final products' SEM results and the corresponding average particle size at different reaction moments.

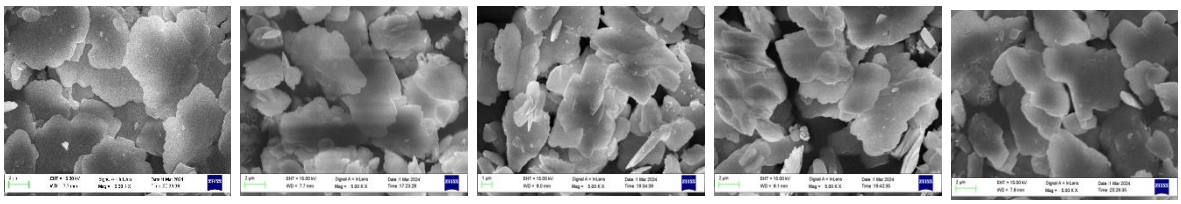

10 min　　36 min　　57 min　　90 min　　120 min

Figure 3-4 SEM of barium sulfate samples obtained in LSE-5:

LSE-5: Rotation speed = 30 rpm, Total feed flow rate: 800 mL/min (×125 min), 25 ℃.

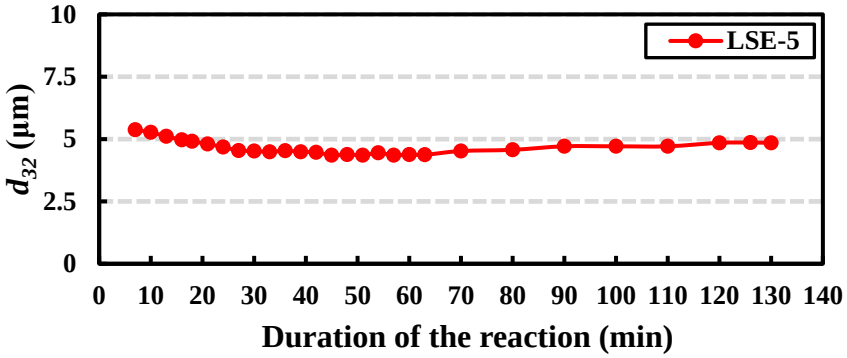

Figure 3-5 Average particle size (d_{32}) of barium sulfate obtained in LSE-5.

Technically, the particle size of the flaky barium sulfate obtained in LSE-5 should correspond with that obtained in LSE-4. Actually, the average particle size of the products obtained in LSE-5 was about 1 μm smaller than that obtained in LSE-4. From the aspect of industry, this nuance could be neglected and acceptable. The fact that such a small decrease in the particle size could be explained by the enhanced shear mixing effect of the $BaSO_4$ suspension. Dherbecourt et al. (2016) reported that a drastic mixing enhancement was observed due to the presence of solid particles. This effect is significantly enhanced by large particles and higher concentrations of particles (Rida et al., 2019). Therefore, in a typical large-scale continuous synthesis of barium sulfate, with the proceeding of the precipitation, more and more $BaSO_4$ particles were produced, which enhanced this mixing effect gradually, decreasing particle size. Then, the whole system could reach a balanced status at some point, where the barium sulfate with stable, uniform particle size distribution was produced.

3.4.2 Comparison of the products synthesized in TCR with different gap widths

Table 19

Characteristics of barium sulfate obtained in different TCRs

Reactor type	TCR^1	TCR^2	TCR^3	
Typical SEM	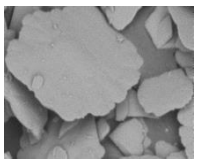	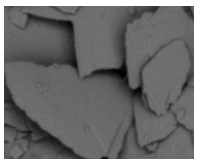	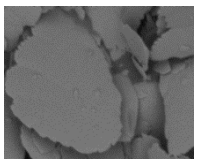	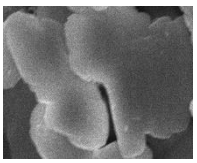
average d_{32}:	12.2μm	9.2μm	6.5μm (LSE-4)	5μm (LSE-5)
Concentration:	0.1 mol/L	0.1 mol/L	0.1 mol/L	0.1 mol/L
Rotation speed:	100 rpm	100 rpm	30 rpm	30 rpm
Linear velocity of inner cylinder:	0.36 m/s	0.34 m/s	0.37 m/s	0.37 m/s
Total feed flow rate:	10 mL/min	20 mL/min	800 mL/min	800 mL/min
Residence time:	13 min	15 min	17.5 min	17.5 min
Duration of reaction:	20 min	25 min	50 min	130 min

[From left to right: TCR^1 (Gap width = 2 mm), TCR^2 (Gap width = 5 mm), TCR^3 (Gap width = 13 mm)]

Comparing the products prepared in different TCRs is meaningful for applying such synthesis methods in the future. The typical amplifying effect of the barium sulfate synthesis in TCR is the change in particle size. As shown in Table 19, the morphologies of these products always keep a stable shape, namely thin and flaky, regardless of the change in gap width of the TCR or reaction conditions. However, the particle size decreases as the duration of the reaction increases. It can be seen from Figure 3-5 (LSE-5) that the particle size keeps decreasing until reaching a particular value, which could be attributed to the clogged area of the reactor as

discussed following. Nevertheless, the particle size is larger than that obtained in the high-speed shear mixer and the ultrasonic reactor, which shows the excellent adaptability of the Taylor-Couette reactors.

Figure 3-6 shows the SEM images of barium sulfate samples taken at different moments in LSE-4 and -5. The results of LSE-5 showed good consistency with that of LSE-4, both products exhibited the desired morphology with acceptable particle size, which showed good reproducibility of such a work.

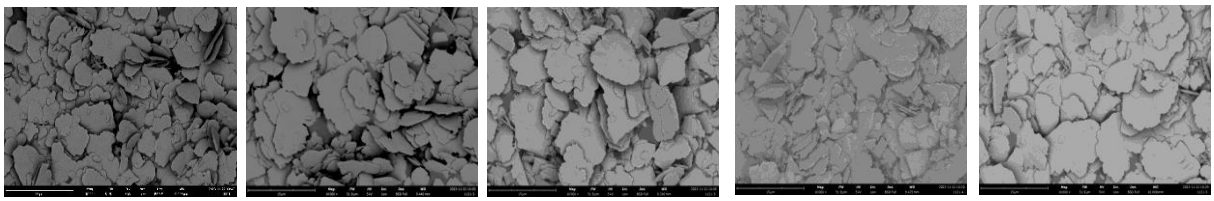

Sample at 15min Sample at 25min Sample at 35min Sample at 45min Sample at 50min

SEM of samples obtained in LSE-4

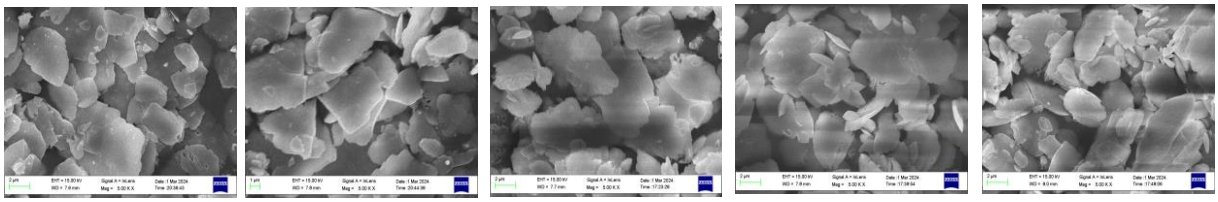

Sample at 16min Sample at 27min Sample at 36min Sample at 45min Sample at 51min

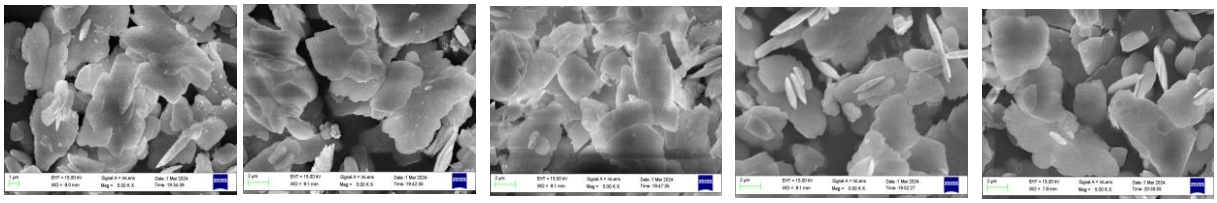

Sample at 70min Sample at 90min Sample at 110min Sample at 126min Sample at 130min

SEM of samples obtained in LSE-5

Figure 3-6 SEM of barium sulfate samples taken at different moments in LSE-4 and -5: LSE-4: Rotation speed = 30 rpm, Total feed flow rate: 800 mL/min (×65 min), 25℃; LSE-5: Rotation speed = 30 rpm, Total feed flow rate: 800 mL/min (×125 min), 25 ℃, [Concentration: 0.1 mol/L, TCR (Gap width = 13 mm)].

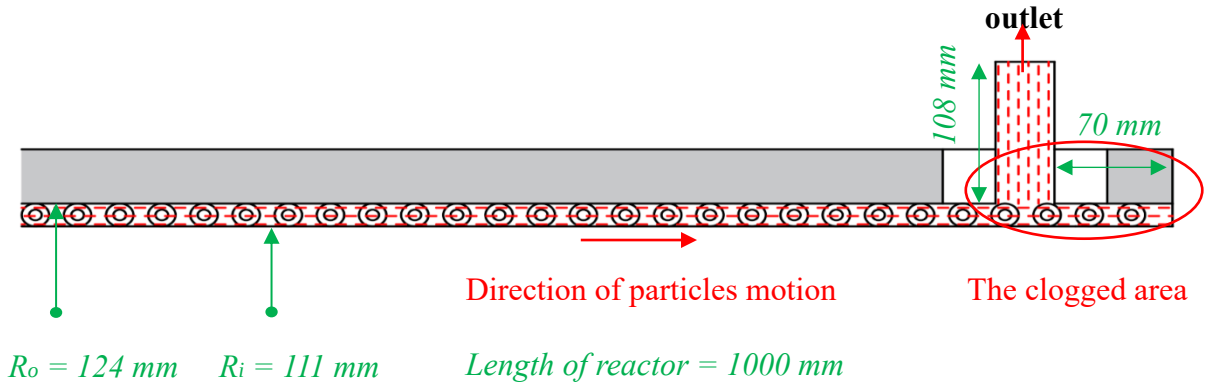

Figure 3-7 Illustration of the clogged area in TCR[3] (Gap width = 13 mm).

During LSE-5, a disadvantage of the reactor was found that a clogged area possibly formed inside the reactor. Table 20 shows the weight of each batch obtained in LSE-5. ΔW is the increment of the weight between the two batches. "Rest" is the total weight of the suspension in the reactor chamber at the end of the reaction. Generally, ΔW should be a constant, yet it kept decreasing until the reaction was almost complete. This could be attributed to the clogged area in the TCR[3] (Gap width =13 mm). As shown in Figure 3-7, a backflow motion of the fluid occurs due to a distance of 70 mm between the outlet and the reactor wall (the clogged area), which forms a counterforce, limiting the natural outflow of barium sulfate suspensions.

Table 20

Weight of products obtained during the process of LSE-5

Batch	1	2	3	4	5	6	7	Rest
W (g)	39	69	92	106	111	136	85	427
ΔW (g)	-	+30	+23	+14	+5	+25	-	-

Besides, during the experiments, we also observed that the outflow of barium sulfate suspensions was not equal to the inflow of the reactant solutions, probably because it was

strenuous for the driving force generated by the pumps to propel such a large volume of suspensions (14L) beyond a height of 108 mm. In that case, the precipitated particles could not be transported out in time, resulting in more and more suspended particles in the reactor, and the formed large particles were broken into small particles. Thus, an apparent decreasing trend in particle size can be observed at the beginning of LSE-5, and then the whole system could reach a balanced status at some point as discussed in section 3.4.1.

Chapter 4. Modeling of the barium sulfate synthesis process in Taylor-Couette reactor

4.1 Introduction

In Chapter 3, flaky barium sulfate with different morphologies and sizes was successfully prepared in TCRs using different combinations of experimental conditions. The results show that rotational speed is essential in affecting the properties of barium sulfate. Therefore, the chapter will focus on studying the impact mechanisms of hydrodynamics in TCRs. Judat et al. (2004) studied the influence of macro- and micromixing on barium sulfate precipitation in a TCR through Particle image velocimetry (PIV) measurements. The results showed that micromixing is a more significant factor in determining the final particle size. Aljishi et al. (2013) examined the influence of different flow structures formed in a TCR on the precipitation of barium sulfate. Hydrodynamics is the core issue for chemical reactor design and the fundamental factor affecting the chemical and physical processes involved in the reactors. With the development of computer technology and the advancement of numerical methods, the computational simulation method has become a powerful tool for studying the flow dynamics that occur in various chemical reactors. Bałdyga et al. (2008) introduced a new breakage model to interpret the erosive dispersion of agglomerates by using the $k-\varepsilon$ model of CFD Fluent. Santos-Moreau et al. (2012) simulated the liquid flow field in a stirred tank reactor with Reynolds-averaged Navier-Stokes equations, and the simulation shows a good agreement with the existing reports. Anabaraonye et al. (2021) utilized CFD to simulate the liquid-phase diffusive and convective transport phenomena inside the Taylor-Couette reactor, which provides a deep and comprehensive understanding of fluid kinetics at turbulent conditions.

4.2 Mathematical modeling

4.2.1 Governing equations

The general continuity equation is given by 4-1. In this work, because of the low volume fraction of particles (< 0.5%), the simulation is conducted in a one-way couple regime, and the fluid flow is assumed to be incompressible and continuous; thus, Eq. 4-1 can be simplified into $\boldsymbol{\nabla} \cdot \boldsymbol{V} = 0$, the equivalent equation is expressed as Eq. 4-2.

$$\frac{\partial \rho}{\partial t} + \boldsymbol{\nabla} \cdot (\rho \boldsymbol{V}) = 0 \tag{4-1}$$

$$\frac{\partial u}{\partial x} + \frac{\partial v}{\partial y} + \frac{\partial w}{\partial z} = 0 \tag{4-2}$$

The hydrodynamics is controlled by Navier-Stokes equations (4-3~4-5) are expressed as below:

$$\frac{\partial (\rho u)}{\partial t} + \boldsymbol{\nabla} \cdot (\rho u \boldsymbol{V}) = -\frac{\partial p}{\partial x} + \rho f_x + F'_{visx} \tag{4-3}$$

$$\frac{\partial (\rho v)}{\partial t} + \boldsymbol{\nabla} \cdot (\rho v \boldsymbol{V}) = -\frac{\partial p}{\partial y} + \rho f_y + F'_{visy} \tag{4-4}$$

$$\frac{\partial (\rho w)}{\partial t} + \boldsymbol{\nabla} \cdot (\rho w \boldsymbol{V}) = -\frac{\partial p}{\partial z} + \rho f_z + F'_{visz} \tag{4-5}$$

Where $\boldsymbol{V}$ is the fluid velocity vector, ρ is the fluid density, p is the pressure, f is the body forces acting on the fluid, and $\boldsymbol{F_{vis}}$ is the viscous forces.

4.2.2 Turbulence model

In this study, $k - \varepsilon$ model is adopted to solve for turbulent kinetic energy k (the energy contained in the velocity fluctuations) and can be calculated from Eq. 4-6, and the turbulent dissipation ε (the rate of the energy dissipation per unit mass of fluid). The eddy viscosity can be described by Eq. 4-7 and 4-8. Shimada and Ishihara (2002) used $k - \varepsilon$ turbulence model to simulate the behavior of water velocity in the channel bends, the results showed that the

standard $k-\varepsilon$ model has a better performance than the realizable $k-\varepsilon$ model in curved channels. Suresha et al. (2024) studied the transient buoyancy-motivated free convection turbulent flow of an incompressible viscous fluid traveling through a vertical cylinder by using $k-\varepsilon$ model, which shows an excellent agreement with the existing experimental results.

$$k=\frac{1}{2}\left(\overline{u'^2}+\overline{v'^2}+\overline{w'^2}\right) \tag{4-6}$$

$$\rho\frac{\partial k}{\partial t}+\rho\overline{u_j}\frac{\partial k}{\partial x_j}=\tau_{ij}\frac{\partial \overline{u_i}}{\partial x_j}-\rho\varepsilon+\frac{\partial}{\partial x_j}\left[(\mu+\mu_t/\sigma_k)\frac{\partial k}{\partial x_j}\right] \tag{4-7}$$

$$\rho\frac{\partial \varepsilon}{\partial t}+\rho\overline{u_j}\frac{\partial \varepsilon}{\partial x_j}=C_{\varepsilon 1}\frac{\varepsilon}{k}\tau_{ij}\frac{\partial \overline{u_i}}{\partial x_j}-C_{\varepsilon 2}\rho\frac{\varepsilon^2}{k}+\frac{\partial}{\partial x_j}\left[(\mu+\mu_t/\sigma_\varepsilon)\frac{\partial \varepsilon}{\partial x_j}\right] \tag{4-8}$$

Wherein: $C_{\varepsilon 1}=1.44,\ C_{\varepsilon 2}=1.92,\ C_\mu=0.09,\ \sigma_k=1.00,\ \sigma_\varepsilon=1.3.$

4.2.3 Numerical modeling

Description of the problem

The Taylor-Couette reactor with a gap width of 5 mm is selected to be the simulated object (Figure 4-1) because systematic investigations of barium sulfate synthesis were conducted in such a reactor.

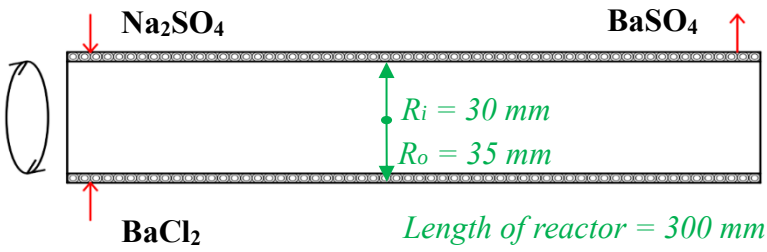

Figure 4-1 Schematic illustration of barium sulfate synthesis in the TCR (Gap width = 5mm)

Geometry model

SOLIDWORKS 2022 and ICEM 19.2 were applied for the 3-D modeling before the whole simulation work, as shown in Figure 4-2.

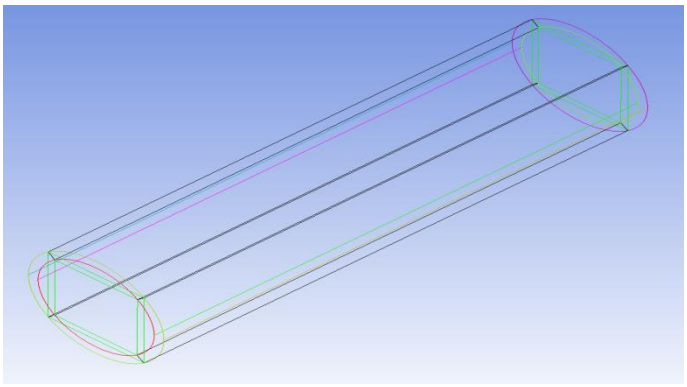

Figure 4-2 Example: geometry model of the fluid domain in TCR (Gap width = 5mm)

Mesh generation

Structured grids are used in the whole geometry model to control the quality of mesh generation and boundary layer mesh. The O-type block method is often used to improve the quality of grids for circular structures, and Figures 4-2 show the typical details of the O-grids. Table 12 gives detailed information about the cell numbers of each TCR mesh.

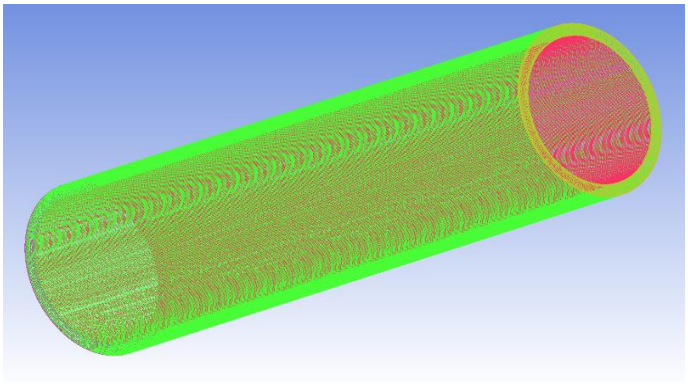

Figure 4-3 Example: meshes of structured at the whole region in TCR (Gap width = 5 mm)

Table 21

The total number of cells throughout the domain in TCR

Direction	TCR^1 (Gap width = 2 mm)	TCR^2 (Gap width = 5 mm)
Length	1500	1580
Circumference	25	25
Gap	15	25
Total cells	2250000	3950000

Method of solution

ANSYS 19.2 was employed to solve the numerical simulation. As mentioned, pure water is the only filler used in experiments due to the low volume of barium sulfate particles. Thus, water was assumed to be the flow material. The density of water is 998.2 kg/$m^{3,}$ and the viscosity is about 0.001003 kg/ms. Steady time and gravity in the y-direction are set in the numerical simulation. The convergence criterion is set at 10^{-4} for all parameters to reach convergence better. Simulation is conducted for 5×10^3 times steps to obtain the steady state of the flows. The case is based on SIMPLE schemes for pressure equations, second-order upwind spatial discretization of other convection-diffusion equations, and the pressure velocity, which is resolved using the SIMPLE algorithm.

Boundary conditions

In this case, boundary conditions are motions of the moving wall, namely the rotation speed of the inner cylinder. Table 22 shows the simulated cases in this work.

Table 22

Cases	Rotation speed (rpm)
TCR with a gap width of 2 mm	200/400/800
TCR with a gap width of 5 mm	100/200/400/800/1000

4.3 Results and Discussion

As discussed in section 2.5.4, particle size decreases with an increased rotation speed in TCRs. It is also worth noticing that the sizes of particles synthesized by TCR with a gap width of 5mm at 200 rpm, 400 rpm, and 800 rpm are larger than those synthesized by TCR with a gap width of 2mm. The radial velocity field in the vertical Y-Z plane is introduced to figure out such a phenomenon.

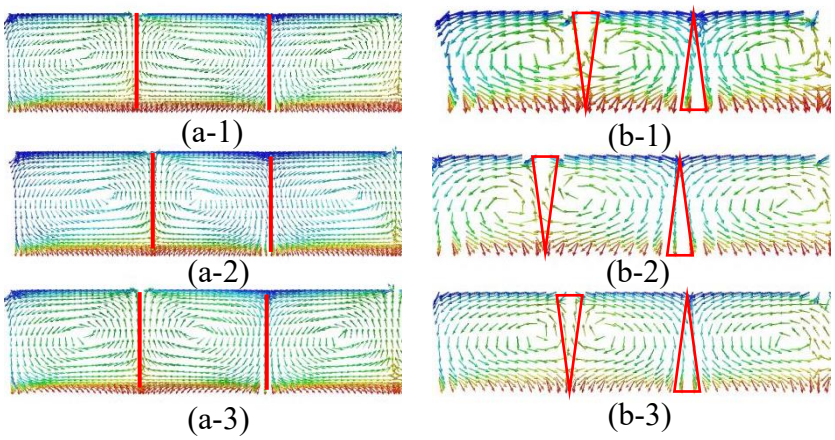

Figure 4-4 Velocity distribution in the Y-Z plane of TCRs:

a-1: 200 rpm, a-2: 400 rpm, a-3: 800 rpm (TCR with a gap width of 5 mm)

b-1: 200 rpm, b-2: 400 rpm, b-3: 800 rpm (TCR with a gap width of 2 mm)

As shown in Figure 4-4, the impinging jet region (the red marked area) between each pair of vortices in TCR with a gap width of 2mm changes from a larger one to a smaller one in the

circumferential direction, while the size of the gap in TCR with a gap of 5 mm has no apparent changes along this direction. Such changes could have a significant influence on the shear distribution in vortices. The fluid flow in the gap between the cylinders can be thought of as either radially outward or inward-impinging jet flows in the region between two counterpart toroidal vortices (Liu et al., 2020). For the given rotational speeds (200 rpm, 400 rpm, 800 rpm), the outward velocities of the jet regions in TCR (Gap width = 2 mm) are higher than those in TCR (Gap width = 5 mm) at the gap region. This shear turbulence intensifies the mixing, leading to a higher gradient and a smaller particle size.

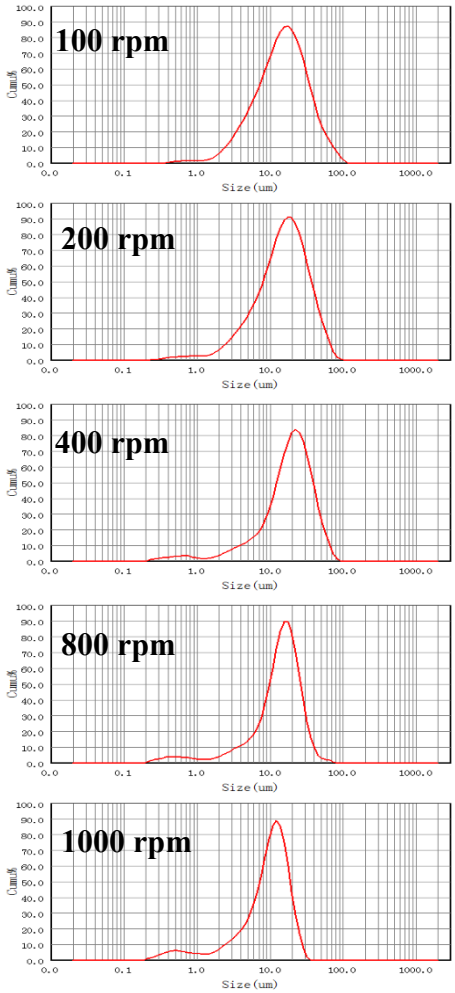

Figure 4-5 Particle size distribution of barium sulfate obtained at different rotation speeds in TCR with a gap width of 5mm [Concentration: 0.1 mol/L, Total feed flow rate: 20 mL/min].

As shown in Figure 4-5, it is clear to see that the particle size distribution becomes narrower as the rotation speed increases. The local shear stress results from the motion of the fluid flow, which plays an important role in determining particle size. Figure 4-6 shows the time average shear strain rate distribution at different rotation speeds in TCR with a gap width of 5 mm. The highest shear strain is formed in the jet regions (close to the walls of the cylinders), while the lowest is formed in the core of the vortices (in the middle of the annulus). To quantitatively identify the effect of rotation speeds on the shear strain rate generated in the reactor, the corresponding shear strain rate is introduced in Figure 4-7. The average turbulent shear is enhanced with the increased rotation speed, and the distribution of the average shear tends to be centralized, leading to a narrower particle size distribution (namely a relatively better uniformity), as introduced in Figure 4-5.

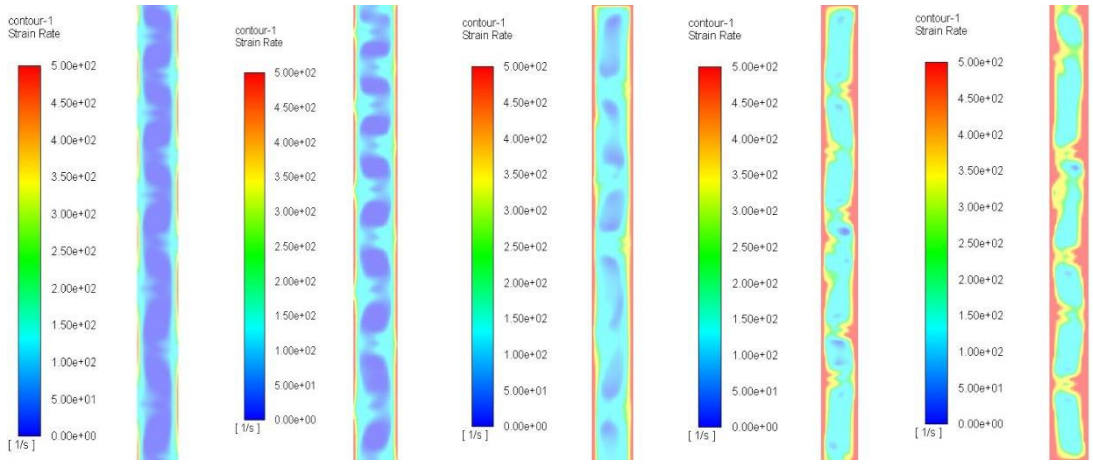

Figure 4-6 The time average shear strain rate at different rotation speeds in TCR with a gap width of 5 mm.

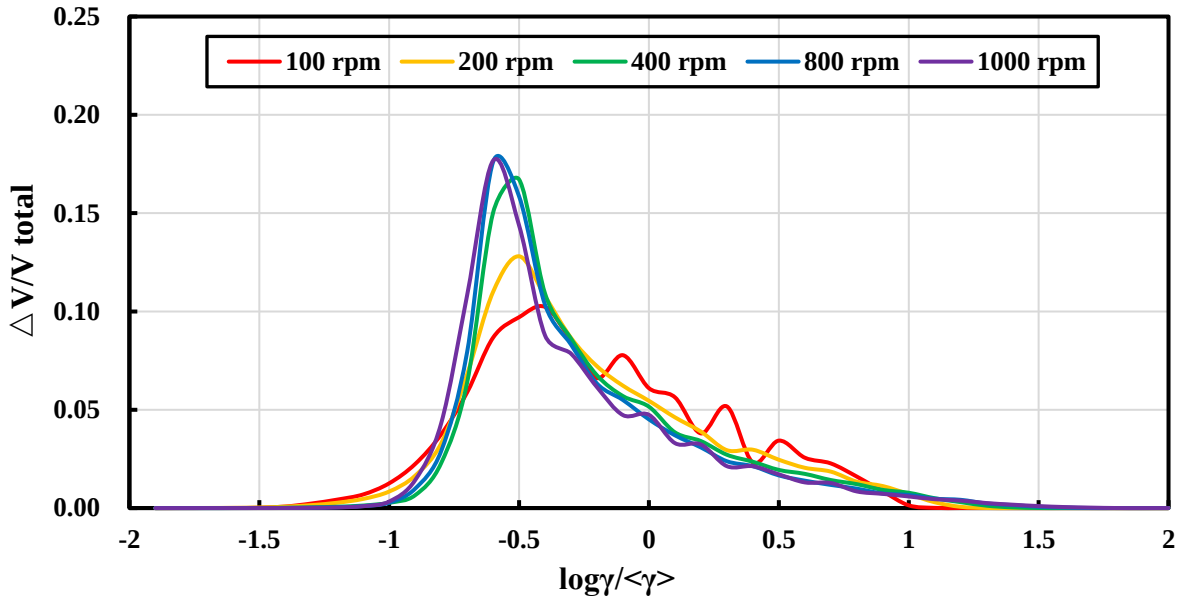

Figure 4-7 Distribution of the shear strain rate at different rotation speeds in TCR with a gap width of 5mm.

Generally, the stable aggregated particle diameter: d_{32} (m) can be determined by an empirical expression according to the review of Jarvis et al. (2005).

$$d_{32} = CG^{-\gamma} \tag{4-9}$$

Where C is the aggregated particle strength coefficient, G is the average velocity gradient (s^{-1}), and γ is the stable aggregate size exponent.

Shear is usually characterized by the average velocity gradient (G) for homogeneous and isotropic turbulence (Camp, 1943), as shown in Eq. 4-10.

$$G = \sqrt{\frac{\varepsilon}{\nu}} \tag{4-10}$$

Where ε is the turbulent energy dissipation rate (m^2s^{-3}), ν is the kinematic viscosity of the fluid (ms^{-1}), and G can be directly deduced from that equation.

Linearization of the Eq. 4-11 allows γ and log C to be found in Figure 4-8.

$$\log d_{32} = \log C - \gamma \log G \tag{4-11}$$

The steepness of the slope can be considered an indicator of suspension strength. From Figure 4-8, the steeper the slope γ shows that the particles are more accessible to break by surface erosion. Thus, a more significant reduction in average particle size can be seen with increasing *G*. As shown in Figure 4-9, the average particle size keeps decreasing with an increasing rotation speed.

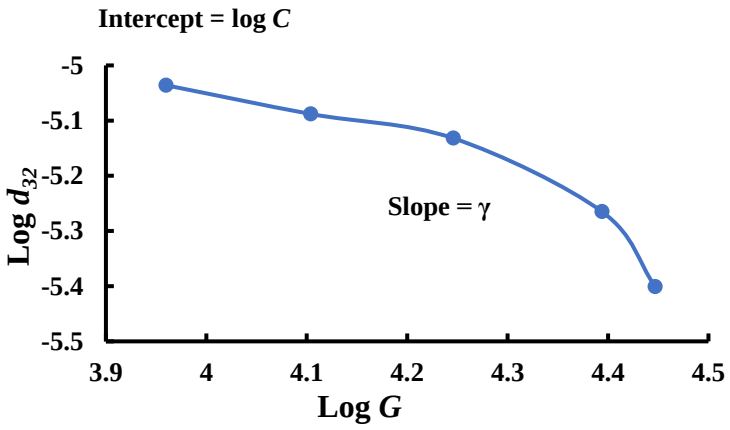

Figure 4-8 The relationship between the change in average particle size of barium sulfate obtained in TCR (Gap width = 5 mm) and the velocity gradient in the reactor.

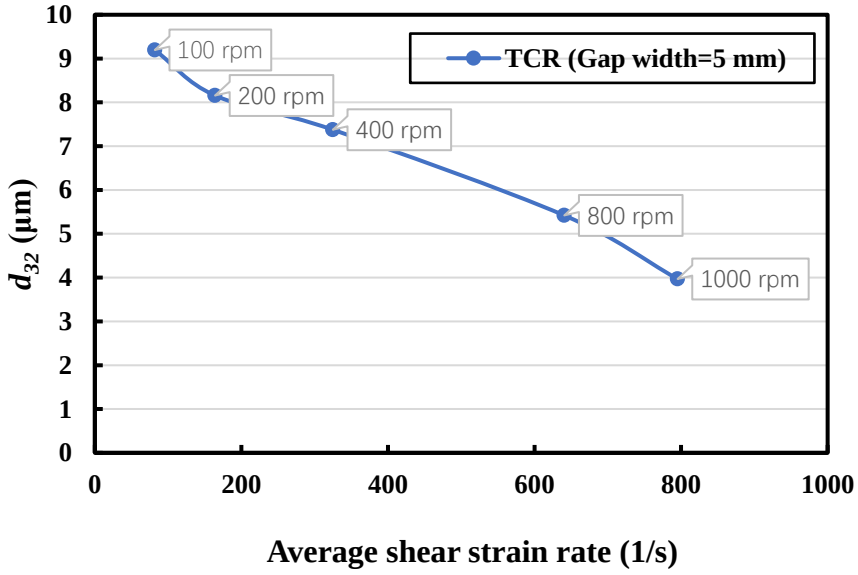

Figure 4-9 Average particle size (d_{32}) of barium sulfate obtained at different rotation speeds (characterized by average shear strain rate) in TCR with a gap width of 5mm.

4.4 Recapitulation and conclusion

In this chapter, we focused on the relationship between the particle size and the rotation speeds of the Taylor-Couette reactor (gap width = 5 mm). With the help of Fluent, the effect of rotation speeds on the particle size was quantified and gave the following conclusions:

1. A higher rotation speed produces a more centralized distribution of the shear force inside the Taylor-Couette reactor, leading to a narrower particle size distribution (or called a better uniformity), but also leads to a smaller average particle size due to the increasing shear.
2. With a narrower gap width, the particle size could be smaller under the same experimental conditions due to the relatively higher velocity gradient.
3. Compared with the visual velocity distribution inside the stirred tank reactor the velocity distribution inside the Taylor-Couette reactor is more uniform, which is beneficial for the formation of the desired barium sulfate.

The analysis of the relationship between the average shear strain (rate) and the particle size shows that a low rotation speed applied in large-scale experiments is reasonable. The uniformity is an important evaluation standard, the average particle size is still yet the most significant standard. Based on the acceptable results of LSE-5, simulation work on determining the optimal rotation speed should continue.

Chapter 5. Conclusions and outlook for the future work

5.1 Conclusion for the present work

In this work, many efforts have been devoted to the experimental investigation of engineering controllable synthesis of barium sulfate with flaky morphology using different chemical reactors. In Chapter 2, four typical chemical reactors were applied in the research of the synthesis of flaky barium sulfate. Then, according to the results of those investigations conducted on a lab scale, experimental continuous synthesizes of flaky barium sulfate were conducted in a pilot-scale Taylor-Couette reactor to examine the feasibility of producing flaky-type barium sulfate. The results showed that the characteristics of the final products were quite acceptable. In summary, barium sulfate with a plate-like shape can be synthesized in any studied reactor by adjusting the operating parameters.

1. Rectangular flaky barium sulfate with about 3 um can be synthesized in a high-speed shear mixer due to such reactors' great shear mixing capacity (Typical experimental conditions: 0.1 mol/L concentration of barium chloride and sodium sulfate, 6500-9500 rpm). At the same time, the complex and unstable flow field in such reactors contributes to some tiny crystals attached to the surface of the products.
2. Round-shaped flaky barium sulfate with about 8.5 um can be synthesized in a simple stirred tank reactor (Typical experimental conditions: 0.1 mol/L concentration of barium chloride and sodium sulfate, 300-500 rpm, propeller; or 0.1 mol/L concentration of the reactants, 300-800 rpm, anchored paddle). However, the apparent crack on the surface of the particles can be observed due to the non-uniform distribution of the flow field in such reactors.

3. Cavitation generated by an ultrasonic reactor favours the formation of rectangular flaky barium sulfate with about 2 um and excellent size distribution (Typical experimental conditions: 0.1 mol/L concentration of barium chloride and sodium sulfate, feed inlet located in the formed annual flow field, 150 W, 30KHz).
4. Round-shaped flaky barium sulfate with a particle size range of about 5-12 um can be synthesized in different Taylor-Couette reactors due to the efficiency but gentle mixing in such reactors, indicating that a uniform turbulent flow regime could be considered an optimal growth area for the formation of flaky barium sulfate. The concentration of the reactants (mol/L), the rotation speed of the reactors (rpm), and the feed flow rate (mL/min) are the three most important operating parameters in the synthesis of flaky barium sulfate. The favorable experimental conditions for the formation of such products are listed below.

   Typical experimental conditions in TCR^1 (Gap width = 2 mm):

   [0.1 mol/L concentration of barium chloride and sodium sulfate, 200 rpm, Total feed flow rate: 10-60 mL/min];

   Typical experimental conditions in TCR^2 (Gap width = 5 mm):

   [0.1 mol/L concentration of barium chloride and sodium sulfate, 100-200 rpm, Total feed flow rate: 20 mL/min-60 mL/min];

   Typical experimental conditions in TCR^3 (Gap width = 13 mm):

   [0.1 mol/L concentration of barium chloride and sodium sulfate, 30 rpm, Total feed flow rate: 800 mL/min].

   Generally, an increase in any of the parameters mentioned above leads to a decrease in

particle size. Higher concentration causes the morphology to change from flaky to aggregated rice-shaped or thick block-shaped. An increase in the rotation speed leads to a change in the morphology from flaky to agglomerated clusters. An increase in the feed flow rate does not influence the morphology of barium sulfate but can significantly affect the particle size, namely a decrease in that.

5.2 Recommendations for the study

Turbulence shear controllable synthesis is a rigorous pathway to produce particles with expected size and particular morphology. However, Taylor-Couette reactors could be considered an ideal option for achieving that goal due to their excellent flexibility in forming those unique flow regimes. However, in this research, the mixing performance of the Taylor-Couette reactor (Gap width = 13 mm) could be limited due to the clogged area, as mentioned in Chapter 3 section 3.4.2. The barium sulfate suspensions cannot smoothly flow out due to the inappropriate design of outlet structure in time, resulting in high-concentration suspensions, which may alter the flow pattern and residence time of particles in Taylor reactors. Therefore, future research should adopt an optimized outlet structure to ensure the smooth outflow of the mixture suspension. According to the existing synthesis method (experimental conditions applied in LSE-4/5), the maximum production of the flaky barium sulfate reaches only 8.2 t/year. It is necessary to continue to optimize this method to achieve the set yield aim. Given the performance of the morphology and the particle size of the flaky barium sulfate synthesized in experiments “C1-b” and “C2-a” are acceptable, it seems that a wider gap can process a higher concentration when a suitable rotation speed is applied. Thus, it is perhaps too conservative that

only 0.1mol/L was applied in these large-scale experiments. A higher concentration and the matched experimental conditions deserve to be studied further to obtain a higher yield.

Note: Experimental conditions applied in this work.

C1-b: TCR[1] (Gap width = 2mm), 0.05ml/L, 100rpm, 20ml/min;

RS2-a: TCR[2] (Gap width = 5mm), 0.1ml/L, 200rpm, 20ml/min;

LSE-4/5: TCR[3] (Gap width = 13mm), 0.1ml/L, 30rpm, 400ml/min.

In Chapter 2 except for section 2.2, the comparison work between the calculated particle size and the measured particle size cannot be completed due to time constraints. Such work should continue in future to strengthen the understanding of the characteristics of different reactors. Besides, the mixing conditions in the ultrasonic reactor seemed more violent than those in the Taylor-Couette reactor. However, flaky barium sulfate with a more regular shape could be produced in such mixing conditions. Further study of the behaviours of the hydrodynamics in the actual ultrasonic condition is promising and meaningful.

As mentioned in Chapter 1, some additives positively influence the formation of barium sulfate particles, such as the reduction in the attachment of tiny crystals on the surfaces, more uniform particle size distribution, and efficient control of the morphology. Thus, it is also necessary and useful to conduct experiments under such a reaction system, if a higher quality of barium sulfate products is required.

REFERENCES

AKONUR, A. & LUEPTOW, R. M. 2003. Three-dimensional velocity field for wavy Taylor–Couette flow. *Physics of Fluids,* 15**,** 947-960.

AKYOL, E. & CEDIMAGAR, M. A. 2016. Size and morphology controlled synthesis of barium sulfate. *Crystal Research and Technology,* 51**,** 393-399.

ALAMER, M., LIM, A. R. & JOO, Y. L. 2018. Continuous synthesis of structurally uniform graphene oxide materials in a model Taylor–Couette flow reactor. *Industrial & Engineering Chemistry Research,* 58**,** 1167-1176.

ALJISHI, M. F., RUO, A.-C., PARK, J. H., NASSER, B., KIM, W.-S. & JOO, Y. L. 2013. Effect of flow structure at the onset of instability on barium sulfate precipitation in Taylor–Couette crystallizers. *Journal of crystal growth,* 373**,** 20-31.

AMIRAFTABI, M., KHIADANI, M. & MOHAMMED, H. A. 2020. Performance of a dual helical ribbon impeller in a two-phase (gas-liquid) stirred tank reactor. *Chemical Engineering and Processing-Process Intensification,* 148**,** 107811.

ANABARAONYE, B. U., BENTZON, J. R., KHALIQDAD, I., FEILBERG, K. L., ANDERSEN, S. I. & WALTHER, J. H. 2021. The influence of turbulent transport in reactive processes: A combined numerical and experimental investigation in a Taylor-Couette reactor. *Chemical Engineering Journal,* 421**,** 129591.

ANDERECK, C. D., LIU, S. & SWINNEY, H. L. 1986. Flow regimes in a circular Couette system with independently rotating cylinders. *Journal of fluid mechanics,* 164**,** 155-183.

ASGHARZADEHAHMADI, S., RAMAN, A. A. A., PARTHASARATHY, R. & SAJJADI, B. 2016. Sonochemical reactors: Review on features, advantages and limitations. *Renewable and Sustainable Energy Reviews,* 63**,** 302-314.

BAŁDYGA, J., ORCIUCH, W., MAKOWSKI, Ł., MALIK, K., ÖZCAN-TAŞKIN, G., EAGLES, W. & PADRON, G. 2008. Dispersion of nanoparticle clusters in a rotor–stator mixer. *Industrial & engineering chemistry research,* 47**,** 3652-3663.

BROMLEY, L. A. 1973. Thermodynamic properties of strong electrolytes in aqueous solutions. *AIChE journal,* 19**,** 313-320.

CAFIERO, L., BAFFI, G., CHIANESE, A. & JACHUCK, R. 2002. Process intensification: precipitation of barium sulfate using a spinning disk reactor. *Industrial & engineering chemistry research,* 41**,** 5240-5246.

CAMP, T. R. 1943. Velocity gradients and internal work in fluid motion. *J. Boston Soc. Civ. Eng.,* 30**,** 219-230.

CHEN, G., LUO, G., XU, J. & WANG, J. 2005. Preparation of barium sulfate particles using filtration dispersion precipitation method in O/W system. *Powder technology,* 153**,** 90-94.

CHERKASOV, N., ADAMS, S. J., BAINBRIDGE, E. G. & THORNTON, J. A. 2023. Continuous stirred tank reactors in fine chemical synthesis for efficient mixing, solids-handling, and rapid scale-up. *Reaction Chemistry & Engineering,* 8**,** 266-277.

COUGHLIN, K. & MARCUS, P. 1992. Modulated waves in Taylor-Couette flow Part 2. numerical simulation. *Journal of Fluid Mechanics,* 234**,** 19-46.

COVENEY, P. V., DAVEY, R., GRIFFIN, J. L., HE, Y., HAMLIN, J. D., STACKHOUSE, S. & WHITING, A. 2000. A new design strategy for molecular recognition in heterogeneous systems: a universal crystal-face growth inhibitor for barium sulfate. *Journal of the American Chemical Society,* 122**,** 11557-11558.

DEHKORDI, A. M. & VAFAEIMANESH, A. 2009. Synthesis of barium sulfate nanoparticles using a spinning disk reactor: Effects of supersaturation, disk rotation speed, free ion ratio, and disk diameter. *Industrial & engineering chemistry research,* 48**,** 7574-7580.

DELACOUR, C., STEPHENS, D. S., LUTZ, C., METTIN, R. & KUHN, S. 2020. Design and characterization of a scaled-up ultrasonic flow reactor. *Organic Process Research & Development,* 24**,** 2085-2093.

DESHAWAR, D. & KUMAR, V. 2017. Hydrodynamics and mixing characterization in a novel high shear mixer. *Chemical Engineering and Processing-Process Intensification,* 120**,** 57-67.

DHERBECOURT, D., CHARTON, S., LAMADIE, F., CAZIN, S. & CLIMENT, E. 2016. Experimental study of enhanced mixing induced by particles in Taylor–Couette flows.

Chemical Engineering Research and Design, 108**,** 109-117.

DONG, Z., DELACOUR, C., MC CAROGHER, K., UDEPURKAR, A. P. & KUHN, S. 2020. Continuous ultrasonic reactors: design, mechanism and application. *Materials,* 13**,** 344.

DONNELLY, R. & SIMON, N. 1960. An empirical torque relation for supercritical flow between rotating cylinders. *Journal of Fluid Mechanics,* 7**,** 401-418.

DUTCHER, C. S. & MULLER, S. J. 2009. Spatio-temporal mode dynamics and higher order transitions in high aspect ratio Newtonian Taylor–Couette flows. *Journal of fluid mechanics,* 641**,** 85-113.

FARAHANI, H. B., SHAHROKHI, M. & DEHKORDI, A. M. 2017. Experimental investigation and process intensification of barium sulfate nanoparticles synthesis via a new double coaxial spinning disks reactor. *Chemical Engineering and Processing: Process Intensification,* 115**,** 11-22.

FERRARI, M., BOCCARDO, G., BUFFO, A., VANNI, M. & MARCHISIO, D. L. 2023. CFD simulation of a high-shear mixer for food emulsion production. *Journal of Food Engineering,* 358**,** 111655.

GIORDANO, R. L., GIORDANO, R. C. & COONEY, C. L. 2000. Performance of a continuous Taylor–Couette–Poiseuille vortex flow enzymic reactor with suspended particles. *Process biochemistry,* 35**,** 1093-1101.

GU, D., LIU, Z., QIU, F., LI, J., TAO, C. & WANG, Y. 2017. Design of impeller blades for efficient homogeneity of solid-liquid suspension in a stirred tank reactor. *Advanced Powder Technology,* 28**,** 2514-2523.

GUHA, D., RAMACHANDRAN, P. & DUDUKOVIC, M. 2007. Flow field of suspended solids in a stirred tank reactor by Lagrangian tracking. *Chemical Engineering Science,* 62**,** 6143-6154.

GUPTA, A., SINGH, P. & SHIVAKUMARA, C. 2010. Synthesis of BaSO4 nanoparticles by precipitation method using sodium hexa metaphosphate as a stabilizer. *Solid State Communications,* 150**,** 386-388.

HAN, S., YANG, Z., ZHANG, L., ZHANG, Z. & ZHANG, J. 2024. Development of reflective

cooling plasticized polyvinyl chloride/precipitated barium sulfate composites for building roof applications throughout entire solar wavebands. *Journal of Vinyl and Additive Technology,* 30**,** 172-185.

HARTMANN, H., DERKSEN, J. & VAN DEN AKKER, H. 2006. Numerical simulation of a dissolution process in a stirred tank reactor. *Chemical Engineering Science,* 61**,** 3025-3032.

HARVEY, D. 2000. *Modern analytical chemistry*, McGraw Hill.

HASHEMI, S. A., HAJIALIGOL, N., MAZAHERI, K. & FATTAHI, A. 2014. Investigation of the effect of the flame holder geometry on the flame structure in non-premixed hydrogen-hydrocarbon composite fuel combustion. *Combustion, Explosion, and Shock Waves,* 50**,** 32-41.

HOSEINI, S., NAJAFI, G., GHOBADIAN, B. & AKBARZADEH, A. 2021. Impeller shape-optimization of stirred-tank reactor: CFD and fluid structure interaction analyses. *Chemical Engineering Journal,* 413**,** 127497.

HU, L., WANG, G., CAO, R., YANG, C. & CHEN, X. 2014. Fabrication and surface properties of hydrophobic barium sulfate aggregates based on sodium cocoate modification. *Applied surface science,* 315**,** 184-189.

JAHANSHAHI-ANBOOHI, J. & MOLAEI DEHKORDI, A. 2019. Continuous synthesis of barium sulfate nanoparticles in a new high-speed spinning disk reactor. *Industrial & Engineering Chemistry Research,* 58**,** 16597-16609.

JARVIS, P., JEFFERSON, B., GREGORY, J. & PARSONS, S. A. 2005. A review of floc strength and breakage. *Water research,* 39**,** 3121-3137.

JOHNSON JR, W., BERGFELD, W. F., BELSITO, D. V., HILL, R. A., KLAASSEN, C. D., LIEBLER, D. C., MARKS JR, J. G., SHANK, R. C., SLAGA, T. J. & SNYDER, P. W. 2018. Safety assessment of barium sulfate as used in cosmetics. *International journal of toxicology,* 37**,** 5S-11S.

JONES, F., OGDEN, M. I. & RADOMIROVIC, T. 2018. The impact of oxalate ions on barium sulfate crystallization. *Journal of Crystal Growth,* 498**,** 148-153.

JONES, F., STANLEY, A., OLIVEIRA, A., ROHL, A., REYHANI, M., PARKINSON, G. & OGDEN, M. 2003. The role of phosphonate speciation on the inhibition of barium sulfate precipitation. *Journal of Crystal Growth,* 249**,** 584-593.

JUDAT, B. & KIND, M. 2004. Morphology and internal structure of barium sulfate—derivation of a new growth mechanism. *Journal of Colloid and Interface Science,* 269**,** 341-353.

JUDAT, B., RACINA, A. & KIND, M. 2004. Macro‐and micromixing in a Taylor‐Couette reactor with axial flow and their influence on the precipitation of barium sulfate. *Chemical Engineering & Technology: Industrial Chemistry‐Plant Equipment‐Process Engineering‐Biotechnology,* 27**,** 287-292.

KARBSTEIN, H. & SCHUBERT, H. 1995. Developments in the continuous mechanical production of oil-in-water macro-emulsions. *Chemical Engineering and Processing: Process Intensification,* 34**,** 205-211.

KETEGENOV, T., KAMUNUR, K., BATKAL, A., GANI, D. & NADIROV, R. 2022. Recent advances in the preparation of barium sulfate nanoparticles: a mini-review. *ChemEngineering,* 6**,** 30.

KIATWATTANACHAROEN, S., SRIMAROENG, P., KOTHAN, S., JUMPEE, C., KIM, H. & KAEWJAENG, S. A study of x-ray radiation shielding properties of bricks contained barium sulfate. AIP Conference Proceedings, 2020. AIP Publishing.

KILIAN, H. I., ZHANG, H., SHIRAZ BHURWANI, M. M., NILAM, A. M., SEONG, D., JEON, M., IONITA, C. N., XIA, J. & LOVELL, J. F. 2023. Barium sulfate and pigment admixture for photoacoustic and x-ray contrast imaging of the gut. *Journal of Biomedical Optics,* 28**,** 082803-082803.

KIM, J. S., KIM, D. H., GU, B. & YANG, D. R. 2013. Simulation of Taylor–Couette reactor for particle classification using CFD. *Journal of crystal growth,* 373**,** 106-110.

KIND, M. 2002. Colloidal aspects of precipitation processes. *Chemical engineering science,* 57**,** 4287-4293.

KUCHER, M., BABIC, D. & KIND, M. 2006. Precipitation of barium sulfate: Experimental investigation about the influence of supersaturation and free lattice ion ratio on particle

formation. *Chemical Engineering and Processing: Process Intensification,* 45**,** 900-907.

LAMBERTO, D., ALVAREZ, M. & MUZZIO, F. 2001. Computational analysis of regular and chaotic mixing in a stirred tank reactor. *Chemical Engineering Science,* 56**,** 4887-4899.

LATHROP, D. P., FINEBERG, J. & SWINNEY, H. L. 1992. Transition to shear-driven turbulence in Couette-Taylor flow. *Physical Review A,* 46**,** 6390.

LEWIS, G. S. & SWINNEY, H. L. 1999. Velocity structure functions, scaling, and transitions in high-Reynolds-number Couette-Taylor flow. *Physical Review E,* 59**,** 5457.

LI, J., LIU, D., JIANG, H., WANG, J., JING, X., CHEN, R., ZHU, W., HAN, S., LI, W. & WEI, H. 2016. Effects of polyacrylic acid additive on barium sulfate particle morphology. *Materials Chemistry and Physics,* 175**,** 180-187.

LI, J., ZHOU, Y., WANG, J., WANG, N., BI, J., LI, X., CHEN, K. & HAO, H. 2023. Manipulation of Morphology, Particle Size of Barium Sulfate and the Interacting Mechanism of Methyl Glycine Diacetic Acid. *Molecules,* 28**,** 726.

LIU, L., YANG, X., LI, G., HUANG, X. & XUE, C. 2020. Shear controllable synthesis of barium sulfate particles using lobed inner cylinder Taylor-Couette flow reactor. *Advanced Powder Technology,* 31**,** 1088-1099.

LYCZKO, N., ESPITALIER, F., LOUISNARD, O. & SCHWARTZENTRUBER, J. 2002. Effect of ultrasound on the induction time and the metastable zone widths of potassium sulphate. *Chemical Engineering Journal,* 86**,** 233-241.

MAJJI, M. V. & MORRIS, J. F. 2018. Inertial migration of particles in Taylor-Couette flows. *Physics of Fluids,* 30.

MARCHISIO, D. L., BARRESI, A. A. & FOX, R. O. 2001. Simulation of turbulent precipitation in a semi-batch Taylor-Couette reactor using CFD. *AIChE Journal,* 47**,** 664-676.

MARCHISIO, D. L., BARRESI, A. A. & GARBERO, M. 2002. Nucleation, growth, and agglomeration in barium sulfate turbulent precipitation. *AIChE Journal,* 48**,** 2039-2050.

MISTEWICZ, K., JESIONEK, M., KIM, H. J., HAJRA, S., KOZIOŁ, M., CHROBOK, Ł. & WANG, X. 2021. Nanogenerator for determination of acoustic power in ultrasonic

reactors. *Ultrasonics Sonochemistry,* 78**,** 105718.

MONNIN, C. 1999. A thermodynamic model for the solubility of barite and celestite in electrolyte solutions and seawater to 200 C and to 1 kbar. *Chemical Geology,* 153**,** 187-209.

NAGARAJA, B. M., ABIMANYU, H., JUNG, K. D. & YOO, K. S. 2007. Preparation of mesostructured barium sulfate with high surface area by dispersion method and its characterization. *Journal of colloid and interface science,* 316**,** 645-651.

NEMRI, M., CHARTON, S. & CLIMENT, E. 2016. Mixing and axial dispersion in Taylor–Couette flows: the effect of the flow regime. *Chemical Engineering Science,* 139**,** 109-124.

NEMRI, M., CLIMENT, E., CHARTON, S., LANOE, J.-Y. & ODE, D. 2013. Experimental and numerical investigation on mixing and axial dispersion in Taylor–Couette flow patterns. *Chemical Engineering Research and Design,* 91**,** 2346-2354.

PADRON, A. G. 2005. Effect of surfactants on drop size distributions in a batch, rotor-stator mixer.

POHL, B., JAMSHIDI, R., BRENNER, G. & PEUKER, U. 2012. Experimental study of continuous ultrasonic reactors for mixing and precipitation of nanoparticles. *Chemical engineering science,* 69**,** 365-372.

POHL, B., OZYILMAZ, N., BRENNER, G. & PEUKER, U. A. 2009. Characterisation of conical geometry for an ultrasonic flow reactor. *Chemie Ingenieur Technik,* 81**,** 1613-1622.

QI, L., MA, J., CHENG, H. & ZHAO, Z. 1996. Preparation of BaSO4 nanoparticles in non-ionic w/o microemulsions. *Colloids and Surfaces A: Physicochemical and Engineering Aspects,* 108**,** 117-126.

RACINA, A. & KIND, M. 2006. Specific power input and local micromixing times in turbulent Taylor–Couette flow. *Experiments in fluids,* 41**,** 513-522.

RAHIMI, M., MOVAHEDIRAD, S. & SHAHHOSSEINI, S. 2017. CFD study of the flow pattern in an ultrasonic horn reactor: Introducing a realistic vibrating boundary

condition. *Ultrasonics sonochemistry,* 35**,** 359-374.

RIDA, Z., CAZIN, S., LAMADIE, F., DHERBECOURT, D., CHARTON, S. & CLIMENT, E. 2019. Experimental investigation of mixing efficiency in particle-laden Taylor–Couette flows. *Experiments in Fluids,* 60**,** 1-13.

SAJJADI, B., ASGHARZADEHAHMADI, S., ASAITHAMBI, P., RAMAN, A. A. A. & PARTHASARATHY, R. 2017. Investigation of mass transfer intensification under power ultrasound irradiation using 3D computational simulation: A comparative analysis. *Ultrasonics sonochemistry,* 34**,** 504-518.

SANTOS-MOREAU, V., BRUNET-ERRARD, L. & ROLLAND, M. 2012. Numerical CFD simulation of a batch stirred tank reactor with stationary catalytic basket. *Chemical engineering journal,* 207**,** 596-606.

SCHRIMPF, M., ESTEBAN, J., WARMELING, H., FäRBER, T., BEHR, A. & VORHOLT, A. J. 2021. Taylor‐Couette reactor: Principles, design, and applications. *AIChE Journal,* 67**,** e17228.

SCHWARZER, H. C. & PEUKERT, W. 2004. Combined experimental/numerical study on the precipitation of nanoparticles. *AIChE Journal,* 50**,** 3234-3247.

SEENIVASAN, M., YANG, C.-C., WU, S.-H., CHIEN, W.-C., WU, Y.-S., JOSE, R. & LUE, S. J. 2021. Using a Couette–Taylor vortex flow reactor to prepare a uniform and highly stable Li [Ni0· 80Co0· 15Al0. 05] O2 cathode material. *Journal of Alloys and Compounds,* 857**,** 157594.

SEUNG-YONG, K. & HAK-HEE, K. 2004. A Study on the Surface-Modification of Barium Sulfate/TiO $ _2 $/Dimethicone Composite Powder and its Application in Color Cosmetics. *Journal of the Society of Cosmetic Scientists of Korea,* 30**,** 197-200.

SHIMADA, K. & ISHIHARA, T. 2002. Application of a modified k–ε model to the prediction of aerodynamic characteristics of rectangular cross-section cylinders. *Journal of fluids and structures,* 16**,** 465-485.

SINNOTT, M. D. & CLEARY, P. W. 2016. The effect of particle shape on mixing in a high shear mixer. *Computational Particle Mechanics,* 3**,** 477-504.

SIRECI, S. 2021. Clinical utility of barium sulfate products: Formulation determines appropriate use. *Applied Radiology,* 50**,** 1-7.

SONG, Y., WANG, M., LI, J., CUI, H., SU, H. & LIU, Y. 2021. Controllable synthesis of LiNi1/3Co1/3Mn1/3O2 electrode material via a high shear mixer-assisted precipitation process. *Chemical Engineering Journal,* 419**,** 129281.

STUART, J. T. 1958. On the non-linear mechanics of hydrodynamic stability. *Journal of Fluid Mechanics,* 4**,** 1-21.

SURESHA, S., REDDY, G. J. & BASHA, H. 2024. Turbulent low-Reynolds-number k–ε model effect on buoyancy-driven free convection flow past a vertical cylinder. *Indian Journal of Physics,* 98**,** 659-677.

TANG, Z., KIM, W.-S. & YU, T. 2019. Studies on morphology changes of copper sulfide nanoparticles in a continuous Couette-Taylor reactor. *Chemical Engineering Journal,* 359**,** 1436-1441.

UCHIDA, M., SUE, A., YOSHIOKA, T. & OKUWAKI, A. 2001. Morphology of barium sulfate synthesized with barium (II)–aminocarboxylate chelating precursors. *CrystEngComm,* 3**,** 21-26.

VASHISTH, V., NIGAM, K. & KUMAR, V. 2021. Design and development of high shear mixers: Fundamentals, applications and recent progress. *Chemical Engineering Science,* 232**,** 116296.

VICUM, L., MAZZOTTI, M. & BALDYGA, J. 2003. Applying a thermodynamic model to the non - stoichiometric precipitation of barium sulfate. *Chemical Engineering & Technology: Industrial Chemistry - Plant Equipment - Process Engineering - Biotechnology,* 26**,** 325-333.

VIRONE, C., KRAMER, H., VAN ROSMALEN, G., STOOP, A. & BAKKER, T. 2006. Primary nucleation induced by ultrasonic cavitation. *Journal of crystal Growth,* 294**,** 9-15.

VISHWAKARMA, R. S. & GOGATE, P. R. 2017. Intensified oxalic acid crystallization using ultrasonic reactors: understanding effect of operating parameters and type of ultrasonic

reactor. *Ultrasonics Sonochemistry,* 39**,** 111-119.

WANG, B. & TAO, S. 2022. Synthesis of Micro-/Nanohydroxyapatite Assisted by the Taylor–Couette Flow Reactor. *ACS omega,* 7**,** 44057-44064.

WANG, C., ZHOU, L., ZHANG, S., WANG, L., WEI, C., SONG, W., XU, L. & ZHOU, W. 2021. Morphology of Barite Synthesized by In-Situ Mixing of Na2SO4 and BaCl2 Solutions at 200° C. *Crystals,* 11**,** 962.

WANG, F., XU, G., ZHANG, Z. & XIN, X. 2005. Morphology control of barium sulfate by PEO-PPO-PEO as crystal growth modifier. *Colloids and Surfaces A: Physicochemical and Engineering Aspects,* 259**,** 151-154.

WERELEY, S. T. & LUEPTOW, R. M. 1998. Spatio-temporal character of non-wavy and wavy Taylor–Couette flow. *Journal of Fluid Mechanics,* 364**,** 59-80.

WOHLGEMUTH, K., RUETHER, F. & SCHEMBECKER, G. 2010. Sonocrystallization and crystallization with gassing of adipic acid. *Chemical Engineering Science,* 65**,** 1016-1027.

WOJTAS, K., MAKOWSKI, Ł. & ORCIUCH, W. 2020. Barium sulfate precipitation in jet reactors: Large eddy simulations, kinetics study and design considerations. *Chemical Engineering Research and Design,* 158**,** 64-76.

WONG, D. C. Y., JAWORSKI, Z. & NIENOW, A. W. 2003. Barium Sulphate Precipitation in a Double-Feed Semi-Batch Stirred Reactor. *Chemical Engineering Research and Design,* 81**,** 874-880.

WOOD, R. J., LEE, J. & BUSSEMAKER, M. J. 2017. A parametric review of sonochemistry: Control and augmentation of sonochemical activity in aqueous solutions. *Ultrasonics sonochemistry,* 38**,** 351-370.

WU, H., WANG, C., ZENG, C. & ZHANG, L. 2013. Preparation of barium sulfate nanoparticles in an interdigital channel configuration micromixer SIMM-V2. *Industrial & Engineering Chemistry Research,* 52**,** 5313-5320.

WU, Z., SEOK, S., KIM, D. H. & KIM, W.-S. 2015. Control of crystal size distribution using non-isothermal Taylor vortex flow. *Crystal Growth & Design,* 15**,** 5675-5684.

YOKOTA, M., OIKAWA, E., YAMANAKA, J., SATO, A. & KUBOTA, N. 2000. Formation and structure of round-shaped crystals of barium sulfate. *Chemical Engineering Science,* 55**,** 4379-4382.

ZHANG, J., XU, S. & LI, W. 2012. High shear mixers: A review of typical applications and studies on power draw, flow pattern, energy dissipation and transfer properties. *Chemical Engineering and Processing: Process Intensification,* 57**,** 25-41.

ZHANG, M., ZHANG, B., LI, X., YIN, Z. & GUO, X. 2011. Synthesis and surface properties of submicron barium sulfate particles. *Applied Surface Science,* 258**,** 24-29.

ZHANG, R., LIU, J., HAN, B., HE, J., LIU, Z. & ZHANG, J. 2003. Recovery of nanoparticles from (EO) 8 (PO) 50 (EO) 8/p-xylene/H2O microemulsions by tuning the temperature. *Langmuir,* 19**,** 8611-8614.